

Technical Report Documentation Page

1. Report No. RC-1389A	2. Government Accession No.	3. Recipient's Catalog No.	
4. Title and Subtitle Development of the Procedure for Efficient Evaluation of Bridge Decks		5. Report Date November 2000	
7. Author(s) Andrzej S. Nowak, Maria M. Szerszen and Leslaw J. Kwasniewski		6. Performing Organization Code	
9. Performing Organization Name and Address University of Michigan 2340 GG Brown Bldg. Ann Arbor, MI 48109-2125		8. Performing Org Report No. UMCEE 99-14	
12. Sponsoring Agency Name and Address Michigan Department of Transportation Construction and Technology Division P.O. Box 30049 Lansing, MI 48909		10. Work Unit No. (TRAIS)	
		11. Contract/Grant No. 98-1303 DIR	
15. Supplementary Notes		13. Type of Report & Period Covered Final Report	
		14. Sponsoring Agency Code	
16. Abstract Report provides the background information for the Michigan Deck Evaluation Guide. It consists of chapters dealing with material models for deck analysis, field inspection and field test results, finite element analysis of bridge superstructure, and additional analysis on punching shear failure mode.			
17. Key Words bridge slab decks, deterioration, field inspection, field tests, material models, failure scenarios, finite element analysis, punching shear		18. Distribution Statement No restrictions. This document is available to the public through the Michigan Department of Transportation	
19. Security Classification (report) Unclassified	20. Security Classification (page) Unclassified	21. No of Pages	22. Price

UMCEE 99-14
RC-1389A

November 2000

**DEVELOPMENT OF THE
PROCEDURE FOR EFFICIENT
EVALUATION OF BRIDGE DECKS**

**CONTRACT NO. 98-1303 DIR
Report submitted to
The Michigan Department of Transportation**

Andrzej S. Nowak, Maria M. Szerszen
and Leslaw J. Kwasniewski



Department of Civil and Environmental Engineering
University of Michigan
Ann Arbor, Michigan 48109-2125

DISCLAIMER

The contents of this report reflect the views of the authors, who are responsible for the facts and the accuracy of the information presented herein. This document is disseminated under the sponsorship of the Michigan Department of Transportation and Great Lakes Center for Truck Transportation Research at the University of Michigan Transportation Research Institute, in the interest of information exchange. The Michigan Department of Transportation assumes no liability for the contents or use thereof.

TABLE OF CONTENTS

Acknowledgments	iv
1. Introduction	1
2. Material Models	2
3. Field Inspections	5
4. Deck Deterioration	10
5. Field Tests	29
6. Finite Element Models of Deck Slab Bridges	33
6.1 Need for analytical model for bridge decks	33
6.2 Types of finite element models for bridges	33
6.3 Development of FE model	35
6.4 Calibration of the FE model	63
6.5 Summary of analytical results	70
7. Punching Shear Failure Mode	101
8. Summary	107
References	108

Acknowledgments

The presented research has been sponsored by the Michigan Department of Transportation, and the Great Lakes Center for Truck and Transit Research (GLCTTR) at the University of Michigan which is gratefully acknowledged. The authors thank the present and former technical staff of the Michigan DOT, David Juntunen, Rick Smith, Sonny Jadun, Roger Till, and Sudhakar Kulkarni, for their useful comments, discussions and support, and Thomas Gillespie, of the University of Michigan Transportation Research Institute (UMTRI) for his support.

The project team received help from other researchers, current and former students and staff of the University of Michigan. In particular, thanks are due to Junsik Eom, Chris Eamon, Dr. Ahmet Sanli, and Arnoud Chenal. They were involved in field instrumentation, measurements, and processing of the results.

The realization of the research program would not be possible without in kind support of the Michigan DOT and the University of Michigan. Measurements were taken using equipment purchased by the University of Michigan.

1. INTRODUCTION

Report provides the background information for the Michigan Deck Evaluation Guide. It consists of chapters dealing with material models for deck analysis, field inspection and field test results, finite element analysis of bridge superstructure, and additional analysis on punching shear failure mode.

2. MATERIAL MODELS

The bridge decks considered in this study are made of reinforced concrete. Some of decks had latex overlay which served as the wearing surface to improve permeability. The major parameters which determine the behavior of such deck slabs include: strength of concrete (f'_c), modulus of elasticity of concrete, strength of reinforcement (f_y), quality of concrete (aggregates, cement, water/cement ratio), pouring sequence and environmental conditions (French, Eppers and Hajjar, 1999). Concrete degradation is caused by various factors including shrinkage, temperature variations, fatigue and corrosion (Thoft-Christensen and Sorensen, 1997, Stewart and Rosowsky, 1998, Boothby and Laman, 1999). The deck degradation analysis requires material models for concrete, which account for these parameters.

The primary material-related parameters, which affect the shrinkage properties of concrete, are: cement content, aggregate type and quantity, air content, and mix-additives. High shrinkage can be expected for cement content up to 500 kg/m^3 , but for lower cement content, closer to 280 kg/m^3 , shrinkage will be reduced. The low cement content results in a reduced paste volume and reduced heat of hydration, and therefore reduced thermal stresses and less initial cracking. The increased quantity (by unit volume) of aggregate results in reduced cracking, because paste volume is reduced.

The concrete deck slab is subjected to live load cycles, which are due to truck traffic. The possibility of fatigue failure of concrete in compression depends primarily on the extreme values of the cyclic stress (Schlafli and Bruhwiler, 1998, Szerszen, Destrebecq and Dyduch, 1994, 1995, Holmen, 1982, Cornelissen, Hordijk and Reinhardt, 1986). Under a high stress level of cyclic loading, the most significant parameters are the frequency of load and the shape of the load function over time. Under a low stress level, concrete fatigue behavior is primarily dependent on time, as smaller increments of damage accumulate over many load cycles. It was observed that the stress in concrete decks under traffic loads is low. If the stress level varies within the elastic range, then it can be assumed that the fatigue damage accumulates as a linear function of the number of applied cycles.

Cyclic loading causes mechanical fatigue after kinematically irreversible microscopic deformations occur in the material. Macroscopic fatigue damage can arise not only from cyclic slip (as in the case of metals) but from microcracking in the matrix (such as in composite cementitious materials) or creep. Therefore, mechanical fatigue must be considered in semi-brittle solids such as concrete. Processes, which cause kinematically irreversible microscopic deformations, can be characterized as follows:

1. Frictional sliding between mating faces of microcracks in the matrix or of the interfaces between the matrix and aggregate,
2. Microscopic and macroscopic flaws which cause wedging of the mating surfaces,
3. Microcracking caused by shrinkage may create a permanent transformation strain in the material during cyclic loading as a result of intrinsic material changes,
4. Inelastic strain caused by shear, transformations or expansion.

The degradation of concrete occurs even when the damage is invisible to the naked eye. It can be understood as two types of damage: cyclic damage resulting from linearly accumulated microcracks, and time dependant damage with the assumption of viscous material behavior. Which type of damage is more active depends on the loading level.

The degradation of concrete in compression due to fatigue can be described in the form of a damage function. The stress level, frequency of loading and number of applied cycles are parameters, which influence the damage function. It is assumed, that for a virgin, never loaded material, the damage function takes some initial value larger than zero (which also accounts for shrinkage), and at failure, the damage function is equal to 1. The damage function is represented by the following formula (Szerszen, Destrebecq and Dyduch, 1994):

$$D(t) = 1 - \left[(1 - D_0)^{r+1} - \alpha \Gamma^{(k)} t \right]^{\frac{1}{r+1}} \quad (3-1)$$

$$\Gamma^{(k)} = \frac{1}{T} \int_0^T \left[\frac{\sigma(t)}{f_c} \right]^k dt$$

Where D_0 = initial damage caused by shrinkage and hydration temperatures, T = cycle period, $\alpha = 3.06$, calibration coefficient based on test results, $\sigma(t)$ = stress range, f_c = strength of concrete in compression, t = time under loading condition, k and r = material parameters.

The damage function is a fraction of unity, and under cyclic loading during a long service life it can be between 0.3 and 0.4. The compressive strength and the modulus of elasticity of concrete are to be multiplied by this diminishing coefficient.

It is important to remember that fatigue is only one of the parameters, which influence the degradation of concrete. Some others are shrinkage, temperature gradient, freeze/thaw cycles and chemical corrosion. Some of these parameters were included in the finite element model developed for this project. These parameters affect the strength of concrete and most importantly, the modulus of elasticity. The structural performance of the slab is strongly affected by its stiffness. All kinds of degradation, which decrease the modulus of elasticity and thus the stiffness, will affect the performance of the slab.

It is very difficult to include all parameters that influence the degradation of concrete in one analytical model. One simplified method assumes that the value of elastic modulus can be decreased by 50% due to these cumulative influences. The British Code BS 5400, Part 4.3.2.1, proposes this method to determine the effects of permanent and short term loading, and imposed deformations and crack widths, based on concrete in compression.

3. FIELD INSPECTIONS

The objective of the bridge slab inspection program was to evaluate the actual condition of the inspected decks. In particular, the decks were checked for occurrence of cracks and leaking cracks (through the thickness of the slab), quality of the slab surface, occurrence of crushed concrete, and any kind of holes. The pattern of cracks was investigated to find out if they were caused by shrinkage, temperature gradient, or live load (heavy trucks). The quality of concrete surface was checked to determine if the surface is smooth or rough with some porosity, if a map of tiny cracks exists, and/or if concrete is crushed. The occurrence of holes was investigated to find their probable cause and location within the traffic lane.

The field inspections lead to the following observations. Longitudinal cracks (parallel to girders) were observed in prestressed

bridges, along the longitudinal joints between boxes. Transverse cracks often continued across the full width of the deck. In majority of decks, pot –holes were located along the wheel line of truck traffic, and mostly in the lane used by trucks rather than in a passing lane. Latex overlays were subject to delamination.

The possible types of deck damage, like categories of cracks and holes, crushed concrete and delamination are described in Michigan Deck Evaluation Guide, are presented below in photos from field inspections, Figure 3-1 to Figure 3-9.



Figure 3-1. Transverse Shrinkage Cracks.



Figure 3-2. Longitudinal Cracks.



Figure 3-3. Cracks in Latex Overlay; Core Samples.



Figure 3-4. Potholes in Latex Overlay.



Figure 3-5. Pothole with Map Cracks.



Figure 3-6. Pothole on the Way of Major Crack.



Figure 3-7. Pothole in Latex Overlay.



Figure 3-8. Potholes on the Way of Wheels.

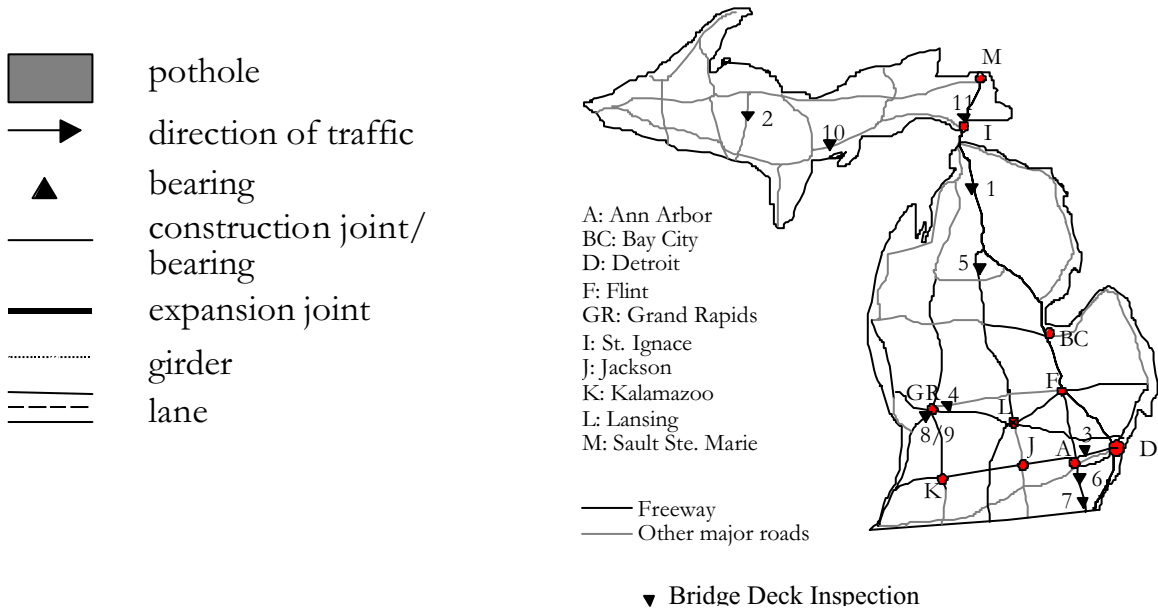


Figure 3-9. Holes on the Way of Wheels; Cracks Close to Joint.

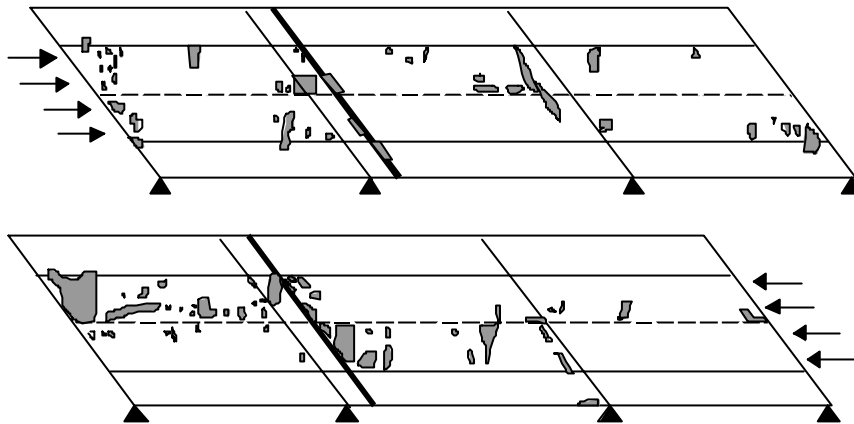
4. DECK DETERIORATION

Patterns of deck slabs deterioration were analyzed based on MDOT Bridge Inspection File (bridges #1 – 24 and #44 - 49), and found during the field inspections in summer 1999 (bridges #25 – 49 and #50 – 52). Possible types of damage described in Chapter 3 and Michigan Deck Evaluation Guide were documented during reviews.

Bridge decks without latex overlay



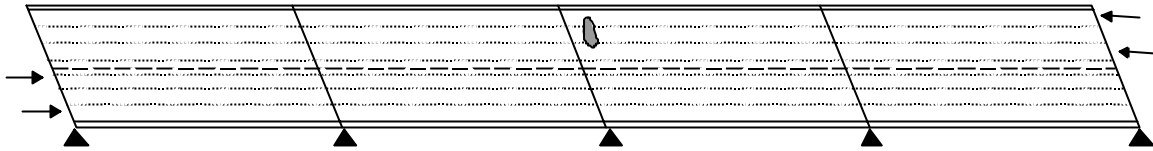
#1



B01-16091
 I-75 NB&SB over Indian River
 1.4 miles north of M-68

year build: 1962; year serv: 32
 ADT: 2750; ADTT 715;
 f'c: 35 MPa; crushed limestone agg.

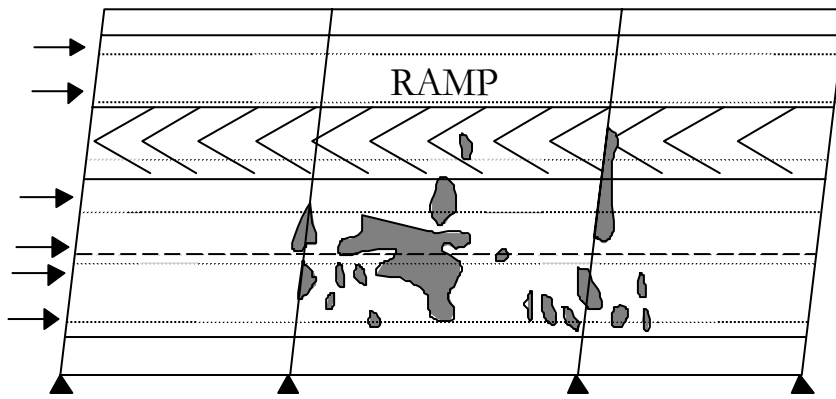
#2



B03-52011
M-95 over the Michigamme River
6.9 miles south of US-41

year build: 1958; year serv: 36
ADT: 2800; ADTT: 196
f'c: 41 MPa; natural agg

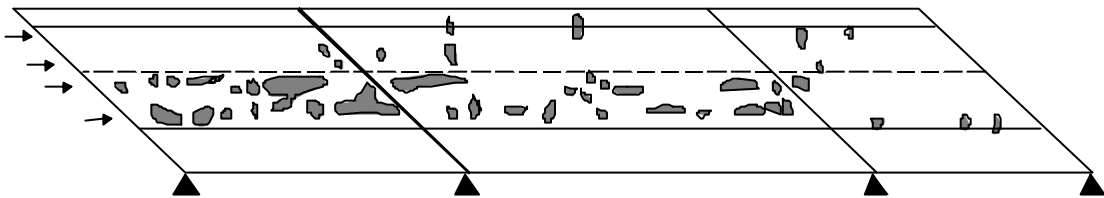
#3



S06-81103;
M-14 EB over Earhart Road
0.5 mile east of US-23

year build: 1964; year serv: 30
ADT: 27500 ADTT: 2475
f'c: 36 MPa; natural agg

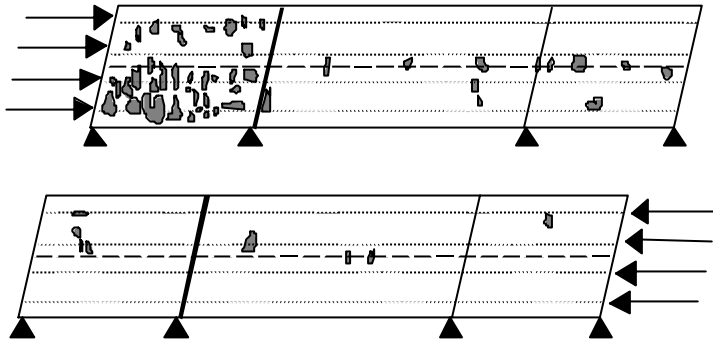
#4



S09-41025
I-196 WB over I-96 EB
Grand Rapids

year build: 1963; year serv: 31;
ADT: 16000; ADTT: 1120
f'c: 40 MPa; crushed natural agg

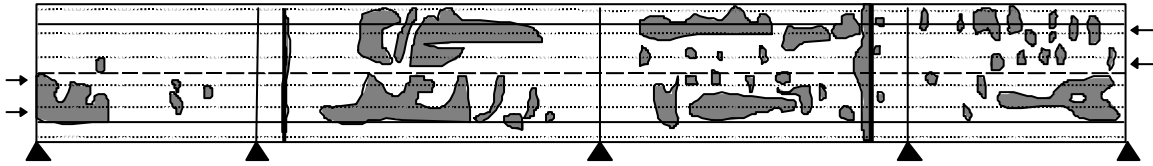
#5



S04-72013;
 Snow Bowl road over US-27 NB
 4.5 miles south of M-55

year build: 1967; year serv: 27
 ADT: 130; ADTT: 4
 f'c: 30 MPa crushed limestone agg

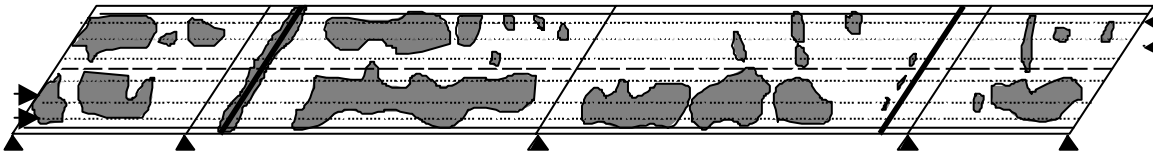
#6



S04-81076
 US-23 under Willis Road
 3.5 miles south of US-12

year build: 1962; year serv: 32;
 ADT: 5627; ADTT: 169
 f'c: 41 MPa; crushed natural agg

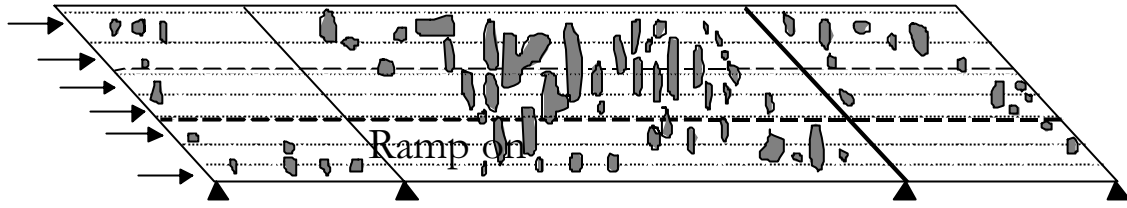
#7



S03-81076
 US-23 under Stoney Creek Road
 3.4 mile north of the Monroe County line

year build: 1962; year serv: 32
 ADT: 3115; ADTT: 93
 f'c: 42 MPa; crushed agg

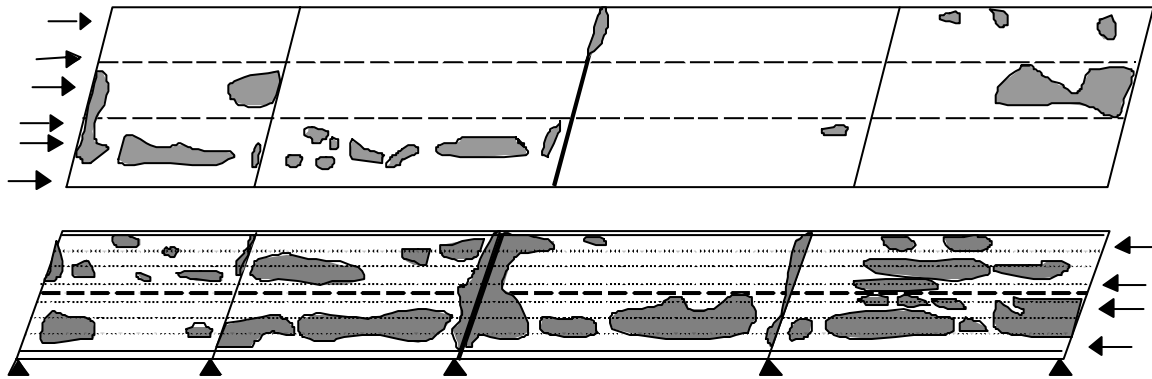
#8



S01-41029;
I-196 EB over Chicago Drive
Grandville

year build: 1960; year serv: 29
ADT: 25500; ADTT 2275
crushed natural agg

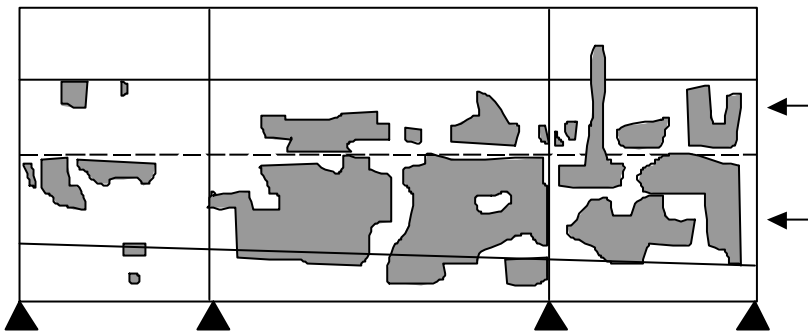
#9



S15-41029
I-196 over Garfield/valley
Grand Rapids

year build: 1964; year serv: 30
ADT: 25500; ADTT: 2295
f_c: 38 MPa; crushed natural agg

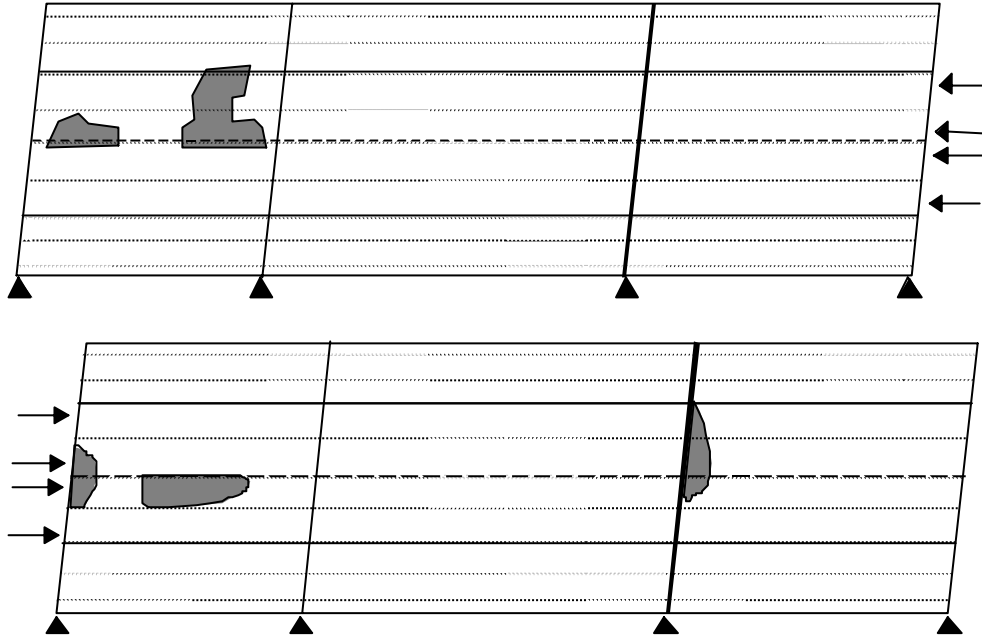
#10



B05-21024
US-2 over the Sturgeon River
0.3 mile east of Nahma Junction

year build: 1972; year serv: 23
ADT: 4000; ADTT: 120
f_c: 33 MPa; crushed limestone agg

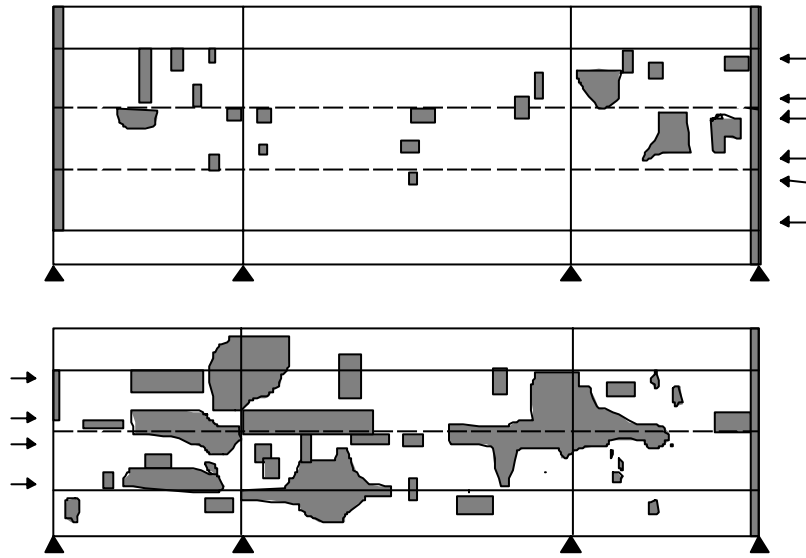
#11



S02-49025;
I-75 over Portage Street
St. Ignace

year build: 1960; year serv: 34
ADT: 3400; ADTT: 408
f_c: 42 MPa; crushed lime stone with latex

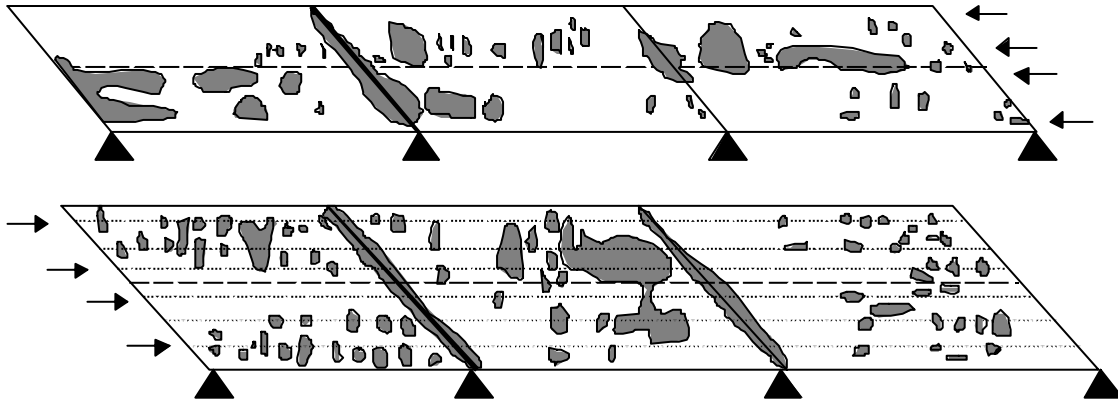
#12



S06-25042;
I-69 EB & WB
over Elm Road

year build: 1960; year serv: 34
ADT: 15000; ADTT: 2850
f_c: 35 MPa; natural agg

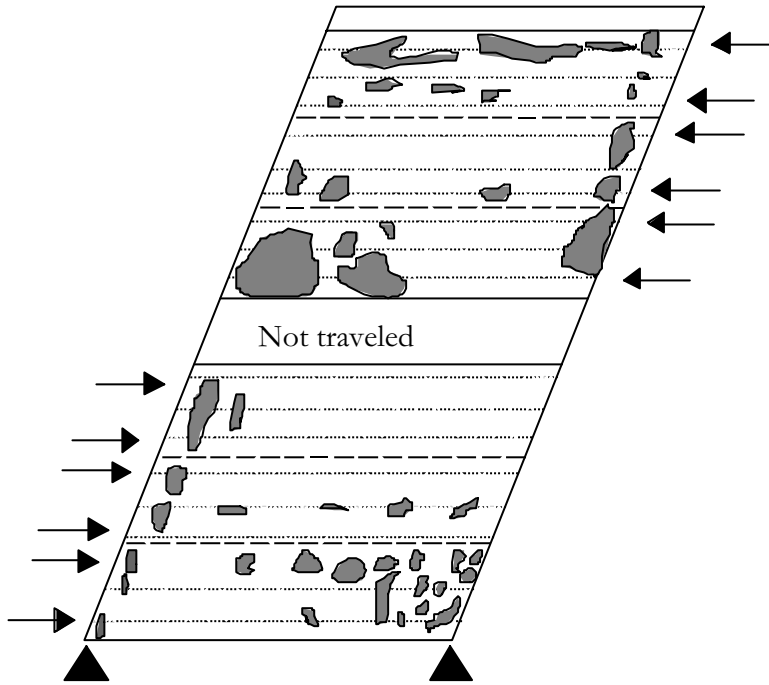
#13



S34-82112
M-102 (8 mile road)
over M-10 (lodge freeway)

year build: 1965; year serv: 29
ADT: 9800; ADTT: 294
f_c: 35 MPa; slag agg

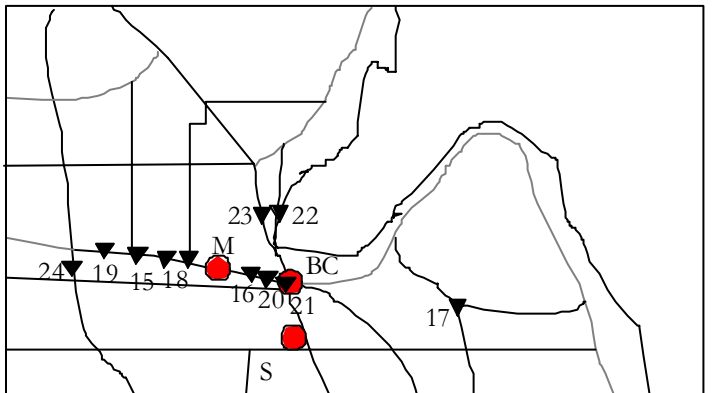
#14



B09-70023
Chicago Drive (old M-21)
over Rush Creek

year build: 1933; year serv: 61
ADT: 15000; ADTT: 1500
f_c: 37 MPa; natural agg.

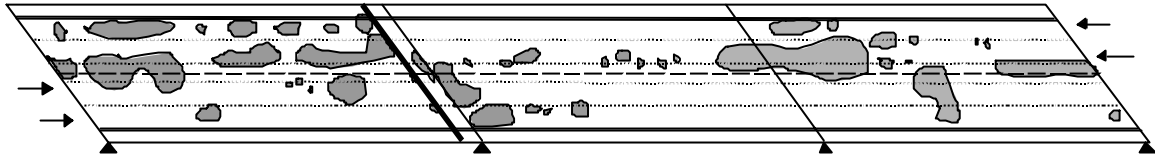
-  pothole
-  direction of traffic
-  bearing
-  construction joint/
bearing
-  expansion joint
-  girder
-  lane



BC: Bay City — Freeway
M: Midland — Other major roads
S: Saginaw — Other roads

▼ Bridge Deck Inspection

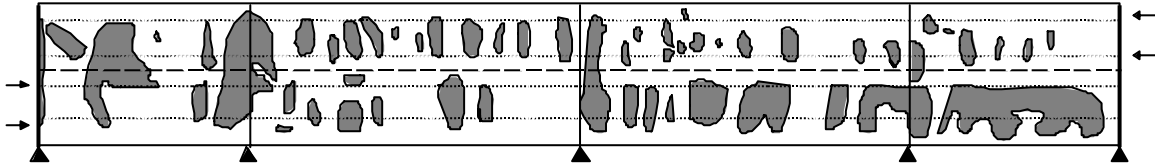
#15



B01-56044
 US-10 EB over Buff creek
 0.8 mile south east of M-18

year build: 1962; year serv: 34
 ADT: 6000; ADTT 480
 f'c: 27 MPa;

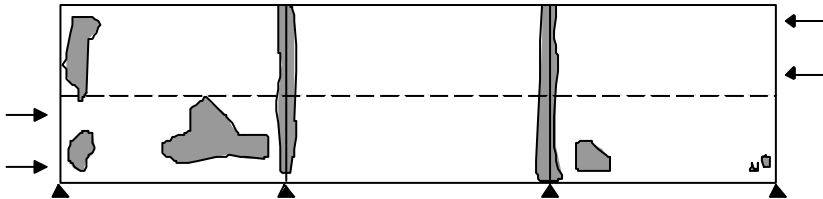
#16



S08-09101
 Nine Mile Road over M-10
 Southern limits of Auburn

year build: 1958; year serv: 37
 ADT: 2120
 f'c: 31 MPa; crushed natural agg

#17



B03-44061
 M-90 over the Flint River
 1.0 mile west of North Branch

year build: 1997; year serv: -2
 ADT: 3500; ADTT: 140
 f'c: 37 MPa; natural agg.

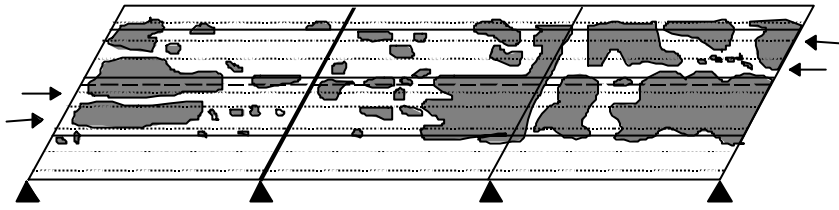
#18



S02-56044;
 West River road over US-10
 1.3 miles northwest of M-30

year build: 1962; year serv: 33;
 ADT: 6862; ADTT: 343
 f'c: 40 MPa; crushed limestone agg

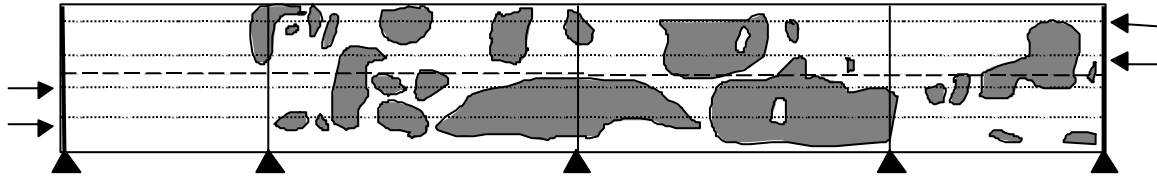
#19



R02-09101;
US-10 NB over GTW RR
0.3 mile east of the Midland County line

year build: 1961; year serv: 34;
ADT: 14500; ADTT: 870
f'c: 34 MPa ; crushed limestone agg

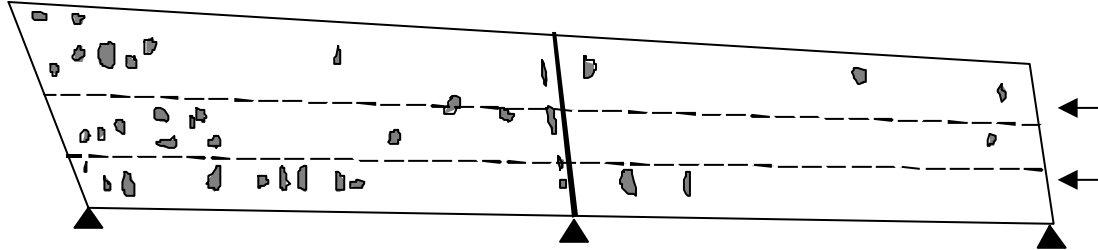
#20



S10-09101;
Mackinaw Road over M-10
4.0 miles west of Bay City

year build: 1958; year serv: 37;
ADT: 7052; ADTT: 212
f'c: 34 MPa; crushed natural agg

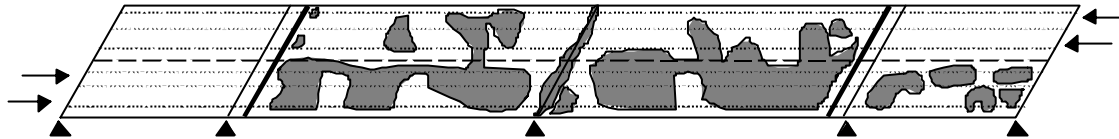
#21



S11-82195
I-75 NB Fisher Freeway
over Lodge Freeway (M-10)

year build: 1953; year serv: 41
ADT: 45000; ADTT 6300
expanded agg

#22



S01-09111;
Wilder Road over M-13
1.9 miles south of Kawkawlin

year build: 1961; year serv: 34
ADT: 17720; ADTT 886
f'c: 34 MPa

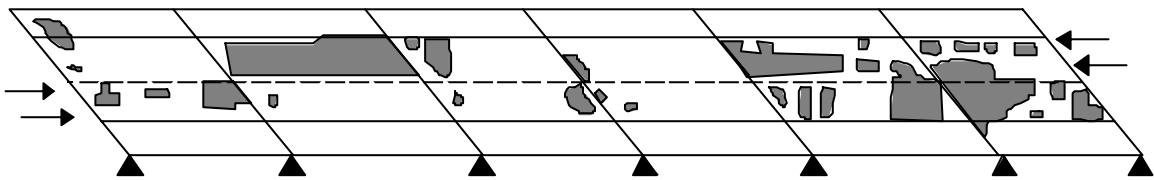
#23



S04-09035;
Wilder Road over I-75
2.0 miles south of Kawkawlin

year build: 1968; year serv: 27
ADT: 6375; ADTT: 191
f'c: 28 MPa

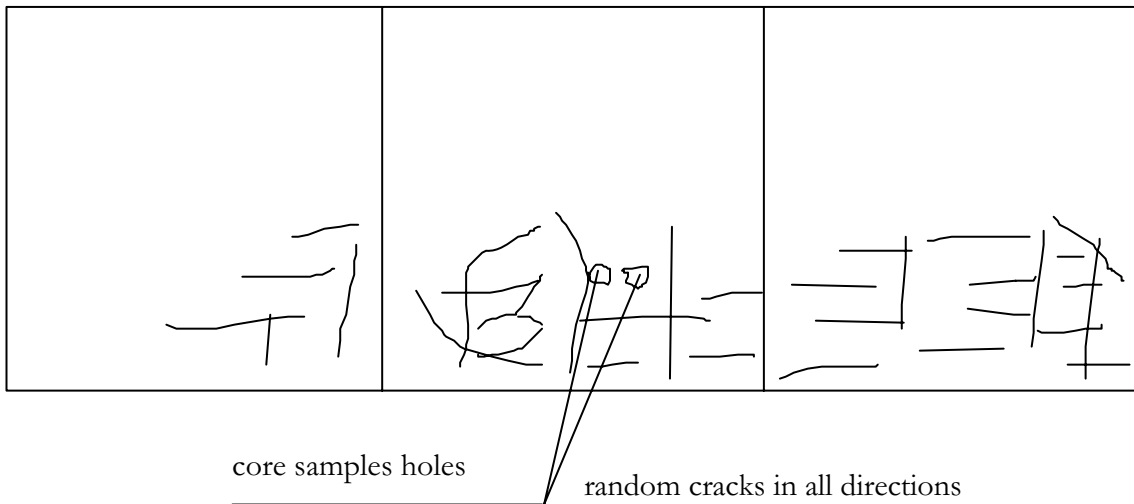
#24



S02-18033;
US-27 NB&SB over US-27 BR
1.0 mile north of Clare

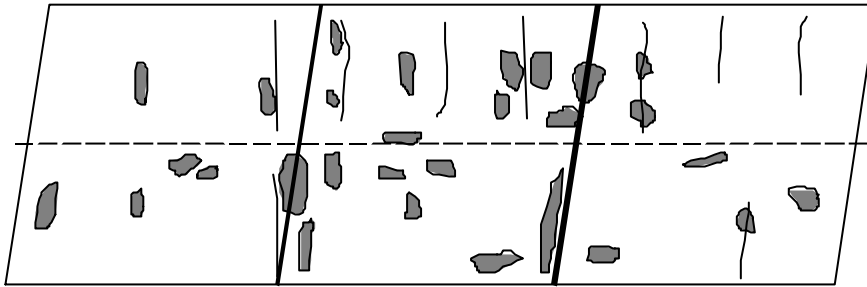
year build: 1961; year serv: 33;
ADT: 10500; ADTT:840
crushed limestone agg

#25



Bridge # S06-38103 on Clear Lake Rd over I94,
Reviewed 9/23/99

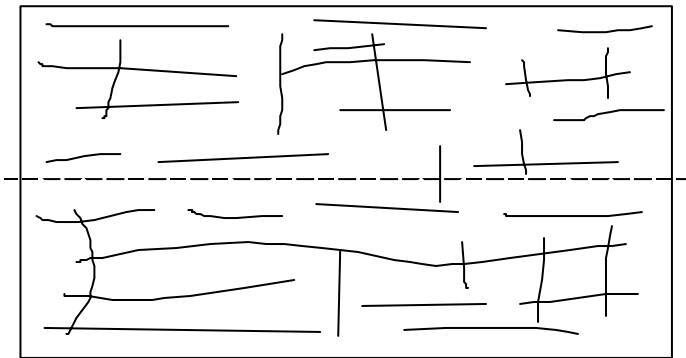
#26



barriers are cracked

Bridge # S06-81076 on Road 12 over US 23 (close to Ann Arbor),
Reviewed 9/3/99

#27



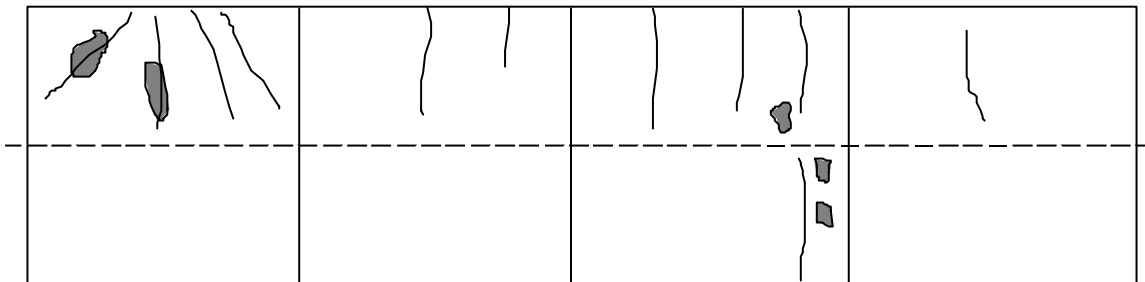
Cracks could occur because of temperature changes. They are about in the same distance that concrete box girders.

map of small cracks on both lanes.

Bridge #B1 77 2 0002903 1301 on Abbotsford Rd. over Mill Creek in St. Clair County, built in 1989

Reviewed 9/3/99

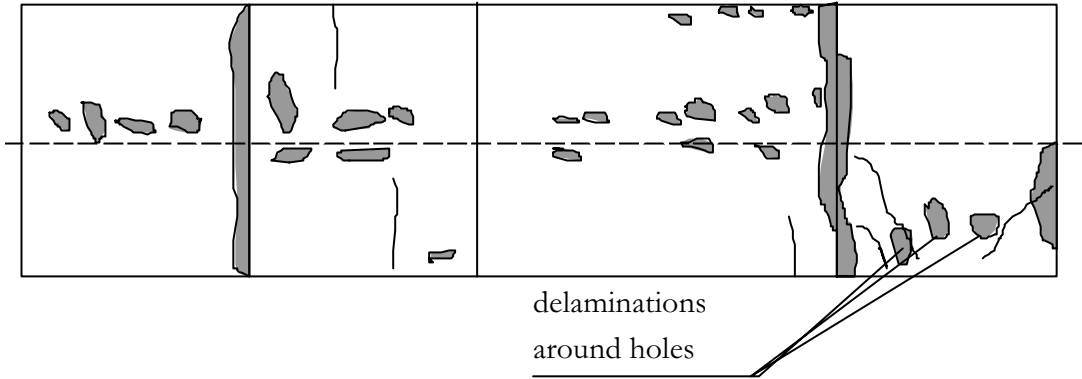
#28



barriers are cracked

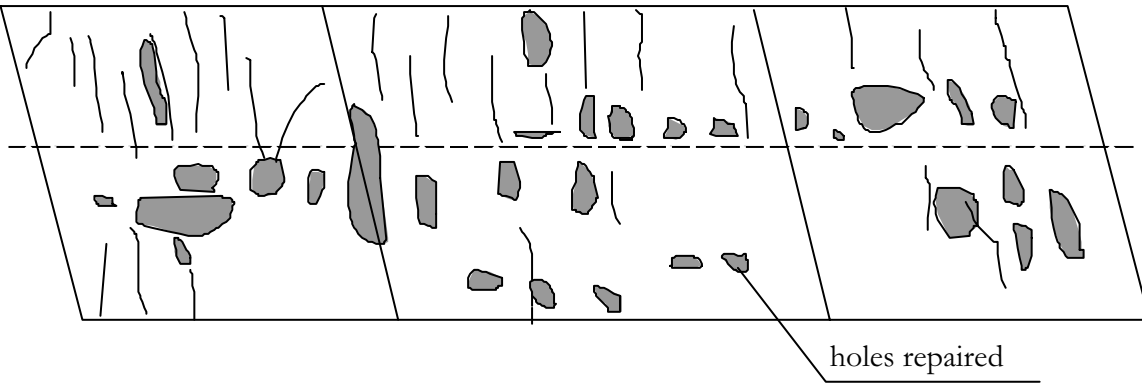
Bridge # S06 - 81076, BBF 218 (19), on Bennis Rd over US 23;
Reviewed 9/6/99

#29



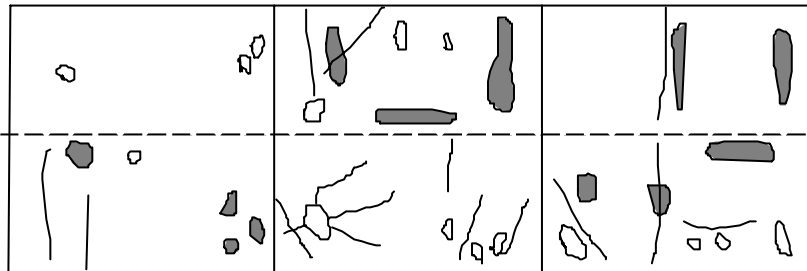
Bridge #S05-47014 on Clyde Rd over I23
built in 1961;
reviewed 10/12/99

#30



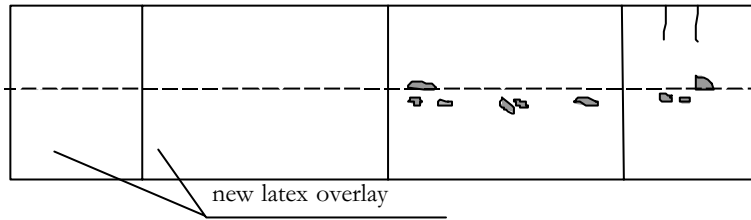
Bridge # B1 47 3 09 0001800 1301 on Crouse Rd over North Ore Creek;
built in 1960;
reviewed 10/12/99

#31



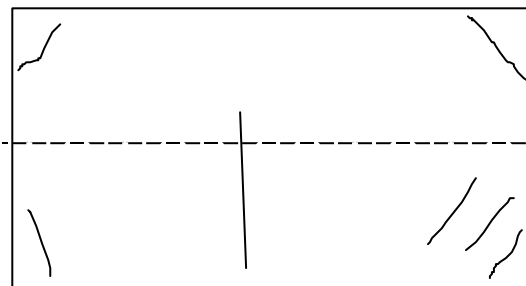
Bridge # S05-81104 on Freer Rd over
I94
Reviewed 9/23/99

#32



Bridge # S06 - 81075, F219 (24) on Joy Rd over I23;
built in 1962; in 1962; reviewed 10/12/99

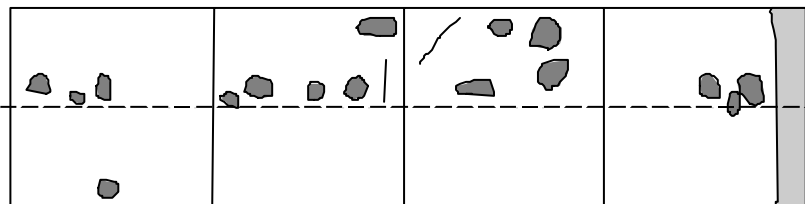
#33



Deck in rather good
condition, only a few
cracks.
One major crack.

Bridge #B04-77012 on M-19 over Mill Creek in Brockway;
Reviewed 6/24/99

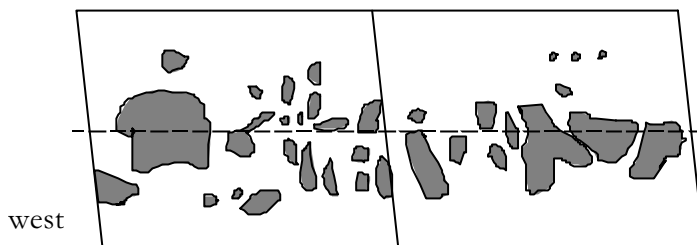
#34



bridge has concrete girders

Bridge #S08-81104 on Parker Rd over I94
Reviewed 9/23/99

#35

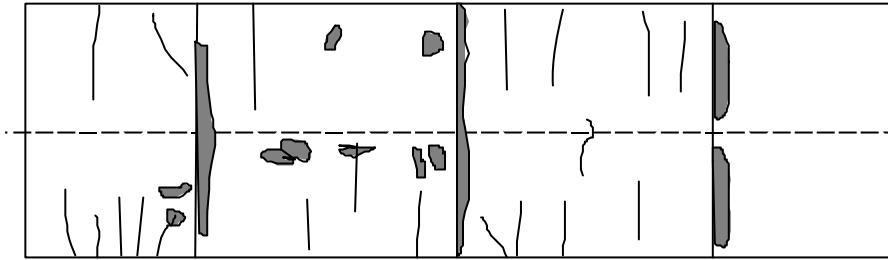


east

Deck is in very bad
condition, deep holes,
upper reinforcement
is visible.

Bridge #S03-81062 on Scio Church over I94 in Ann
built in 1955; reviewed 7/3/99

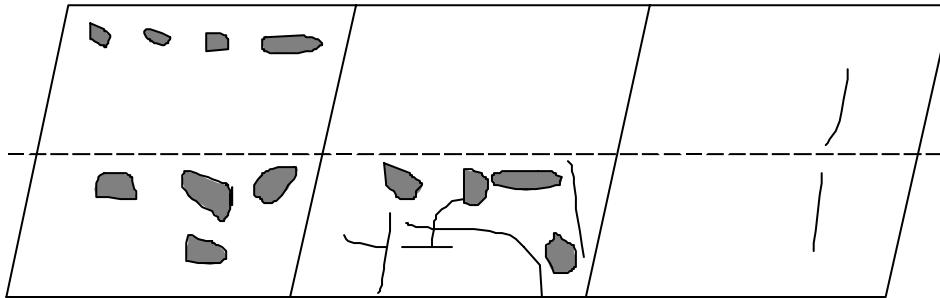
#36



Deck is crushed close to joint

Bridge #S02-81076 on Willow Rd over 23;
Reviewed 9/6/99

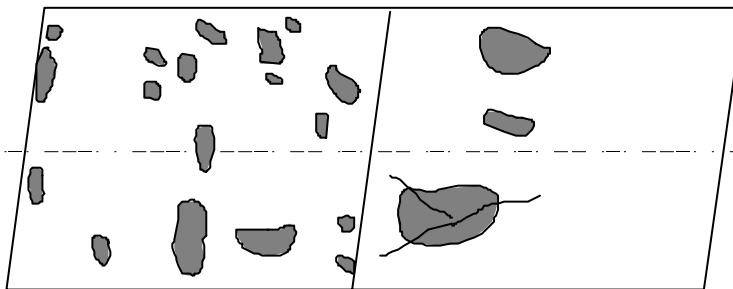
#37



Bridge has big vibrations

Bridge #S10-81104 on Zeeb Rd over I94;
Reviewed 9/23/99

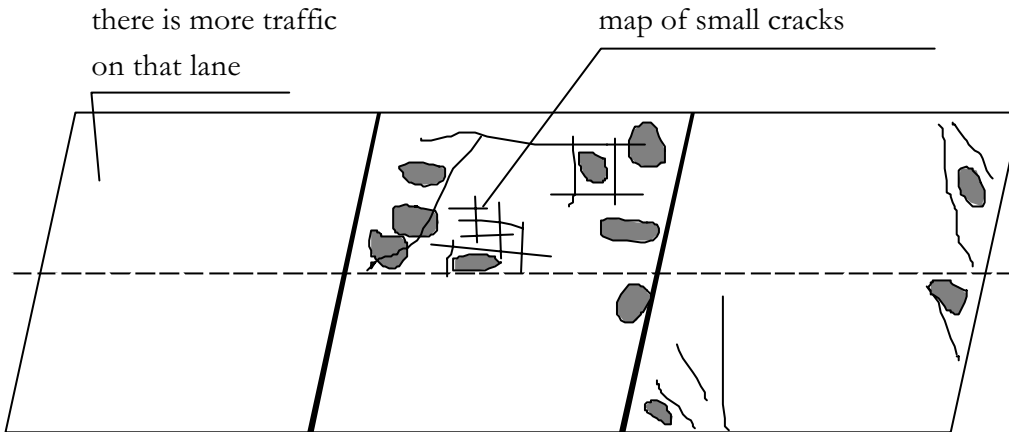
#38



Deck is deteriorated,
deep holes, some of them
are 3 inch deep. About
25% of the surface is
destroyed.

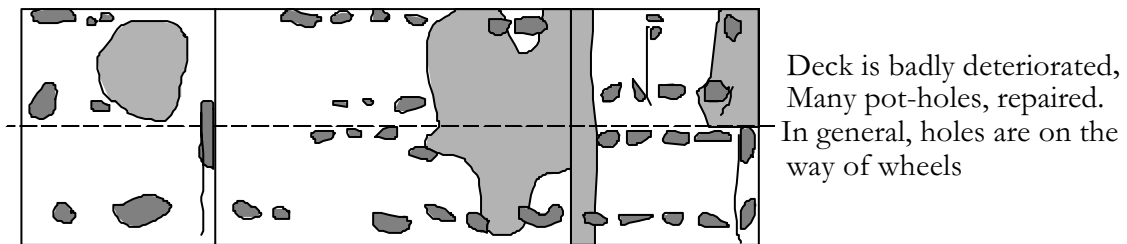
Bridge # S02-41132, on US131 NB over North Park Street,
0.3 mile north of I96 in Grand Rapids; built in 1968; reviewed 7/24/99

#39



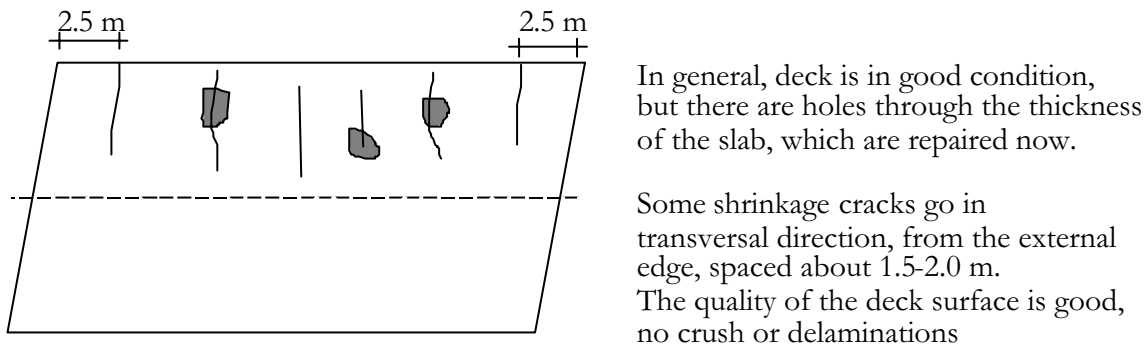
Bridge #B01-59041 on M136 over Black River in St. Claire County
 Reviewed 9/3/99

#40



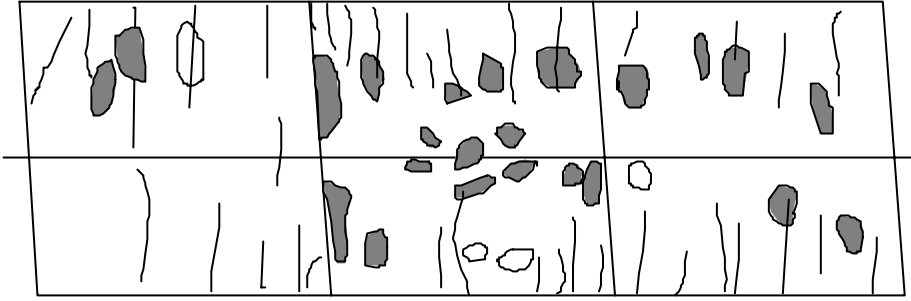
Bridge #B01-59041 on US82 close to US 131 (North to Grand Rapids);
 built in 1961; reviewed 9/21/99

#41



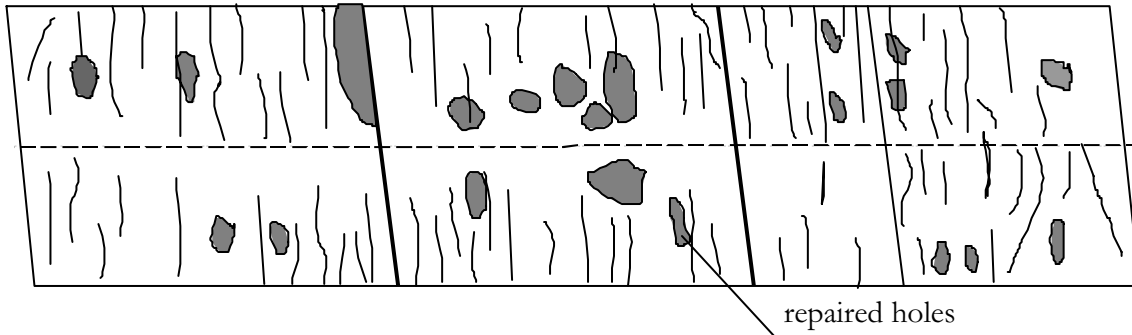
Bridge #B01-33171 on US127 NB over Red Cedar River
 Reviewed 6/14/99

#42



Bridge # S04-58033 on Plank Rd over US23
Built in 1961; reviewed 9/6/99

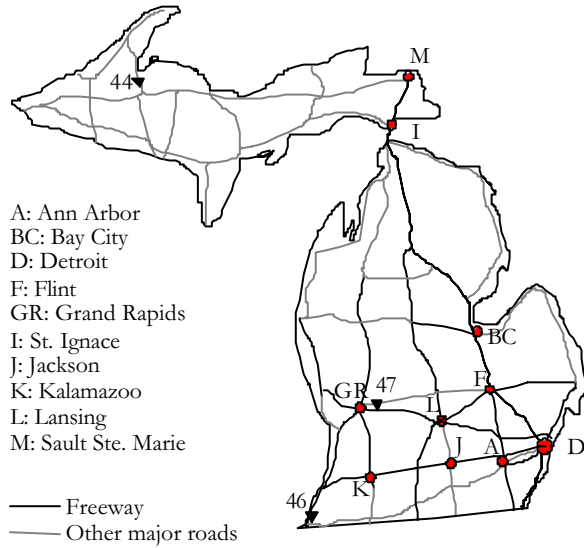
#43



Bridge # S04-47014, B2 of 47-9-6, EBF 219 (20) on Crouse Rd over I23
built in 1961; reviewed 10/12/99; steel girders very corroded

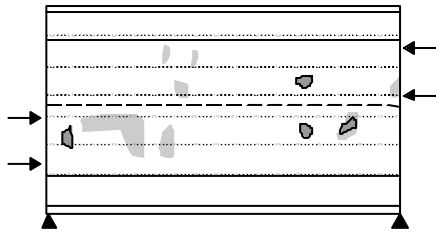
Bridge decks with latex overlay

-  pothole
-  delamination
-  direction of traffic
-  bearing
-  construction joint/
bearing
-  expansion joint
-  girder
-  lane



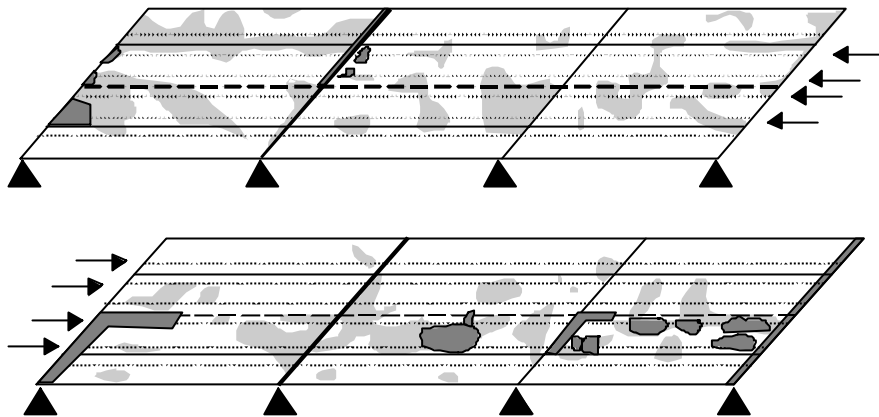
▼ Bridge Deck Inspection

#44



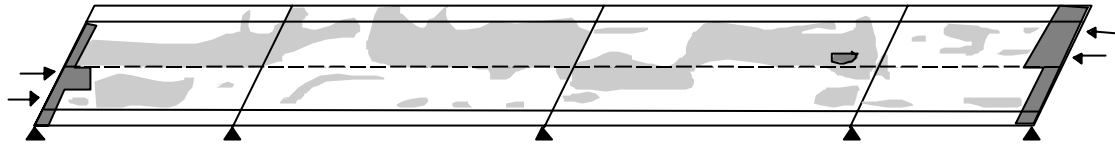
B04-07012 year build: 1960; year serv: 35; year overlay: 21
 US-41 over the Falls River ADT: 5900; ADTT: 413
 L'Anse crushed limestone and natural agg

#45



R01-80024 year build: 1959; year serv: 35; year overlay: 18
 EB&WB I-94 over Amtrak ADT: 4830; ADTT: 81000
 natural agg.

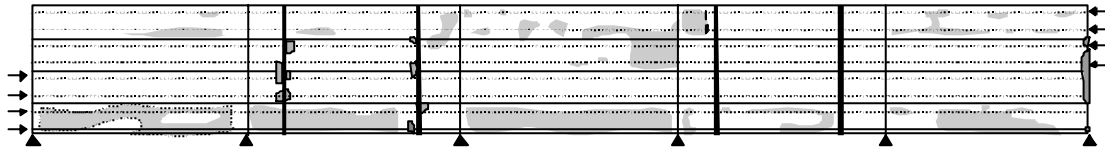
#46



S04-11016;
I-94 under Napier Road
1.4 miles southeast of Benton Harbor

year build: 1960; year serv: 35; year overlay: 21
ADT: 9025; ADTT: 272
f_c:40 MPa; crushed limestone agg

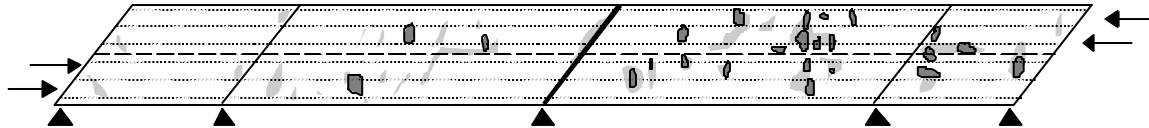
#47



B01-34032
M-66 over the Grand River
Ionia

year build: 1948; year serv: 48; year overlay: ?
ADT: 15000; ADTT: 450
f_c: 39 MPa;

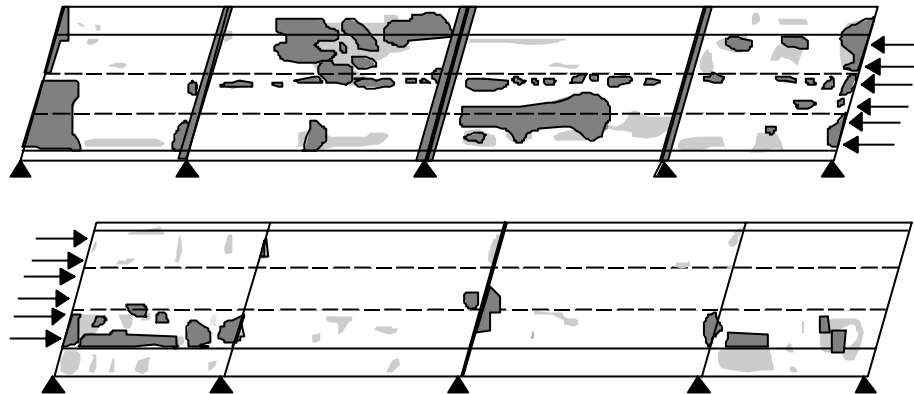
#48



S04-41024;
Whitneyville road over I-96

year build: 1961; year serv: 33; year overlay: 21
ADT: 41000; ADTT: 1640
f_c: 30 MPa; natural agg

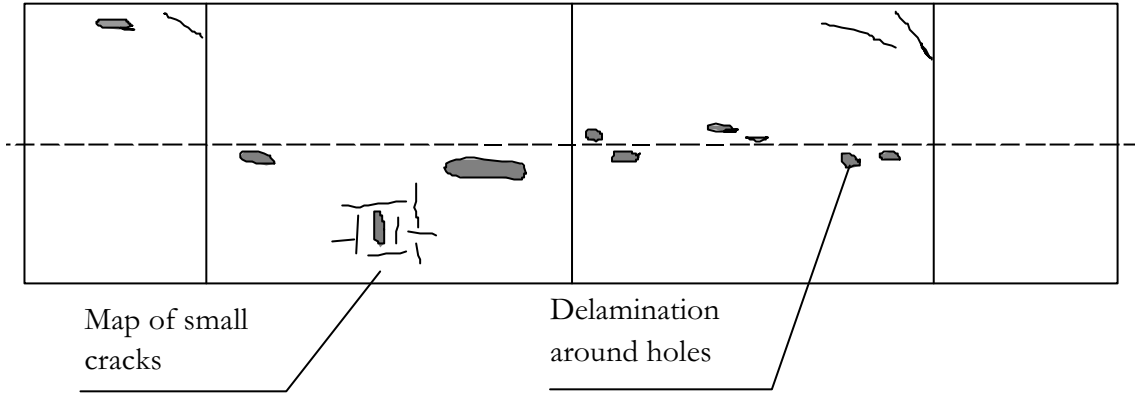
#49



R01-82022;
I-94 EB&WB over Shook road
Romulus

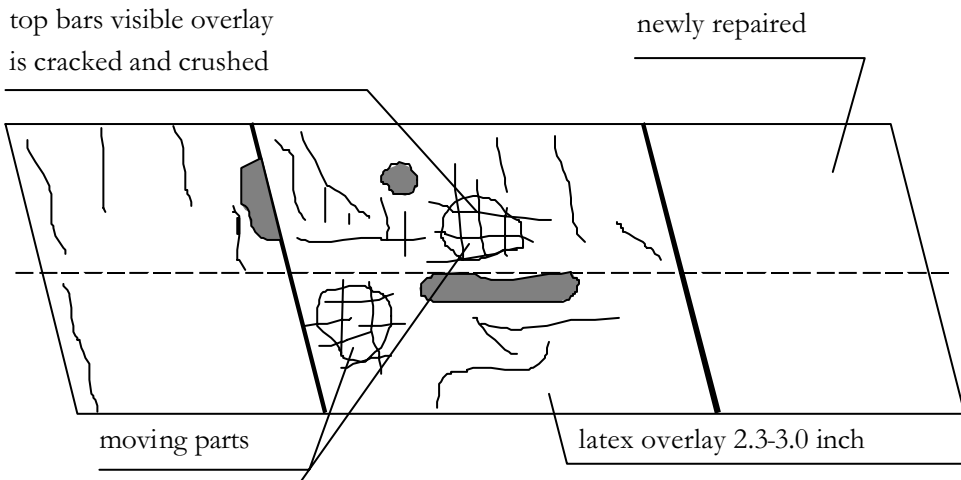
year build: 1962; year serv: 34; year overlay: 18;
ADT: 25000; ADTT: 1500
f_c: 39 MPa; slag agg

#50



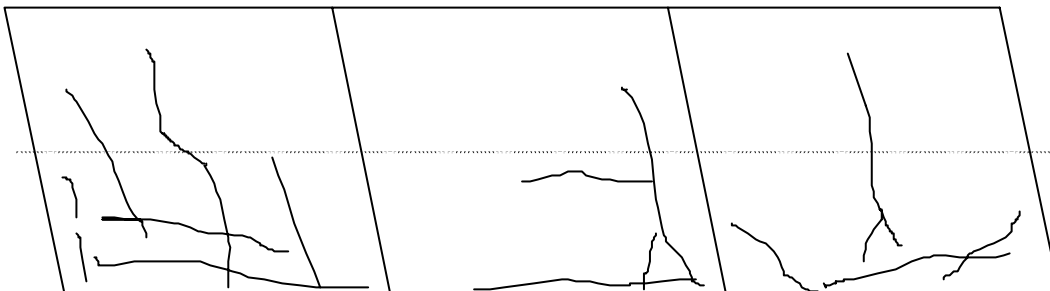
Bridge # S05 - 81075, F219 (24) on Warren Rd over I23; build in 1962; small traffic; Latex overlay; reviewed 10/12/99

#51



Bridge # S08-81075, F219 (24) on Six mile Rd over I23 built in 1962; reviewed 10/12/99

#52



Bridge #S07-81075, MB2 of 81-10-15 on North Territorial Rd over I23 built in 1967; reviewed 10/12/99;

5. FIELD TESTS

The bridge slab testing was oriented to evaluate the quality of concrete. The actual values of concrete strength in compression, f'_c , and modulus of elasticity, E_c , estimated after many years of service were used in finite elements analysis of bridge superstructure (presented in Chapter 6). The quality of concrete was checked using three different methods: H-Meter (Schmidt hammer) and Windsor HP Probe (gun with cartridges) to find the compressive strength, and ultrasonic detector to evaluate the modulus of elasticity.

In the H-Meter method, the rod is pressed against the surface that is to be tested and the rod reaction re-transmits the rebound to the mass inside the hammer. The harder and the more compact the concrete, the greater the rebound. During the rebound stroke, the mass moves a pointer that indicates the maximum point of return, and at the same time, indicates a reference value on the scale. This number, when translated to the H-Meter chart, gives the compression resistance in respect to the impact angle. This method is the most common to check the quality of concrete in the field, but results depend on the preparation of the surface. If the surface is not smooth, it should be ground. It is also necessary to avoid striking the larger pieces of aggregate. Old and dried out concrete has a disproportionately hard surface. Because of this, the readings are higher than the actual value.

The Windsor HP Probe gives a more precise value for the compressive strength of concrete. The cartridge is shot out into the tested element. The length of the pin driven into the material gives the strength. This method accounts for the hardness and size of the aggregate. The reading gives the compressive strength of concrete, the same as tested on standard cylinders. The accuracy guaranteed by producer is about 3%.

The third method used to evaluate the quality of concrete was based on an ultrasonic impulse which goes through the material. Knowing the distance between the sender and receiver of the wave, and the time, it is possible to calculate the modulus of elasticity. All defects inside the material, like delamination, micro-cracks or air voids, cause a drop in velocity and a lower modulus of elasticity. The field measurement results are shown in Table 5-1. Number of applied cycles, presented in the table was determined based on ADTT

for particular road and years of service. Concrete strength in compression is presented in two columns as measured using H Meter and Windsor Probe. Two values of modulus of elasticity (MOE) are presented for each tested deck. The first value is calculated based on concrete strength in compression (the minimum measured value), the second value was measured using ultrasonic impulse method. The latter is smaller because it takes into account the imperfections inside concrete. Also shown in this column is the ratio of these two moduli (measured and calculated). When the MOE was not measured in the field, then lab results were used instead.

Comparing results obtained from these three methods, it was found that the H-Meter gives a higher value for compressive strength than the Windsor HP Probe, because the H-Meter gives results depending on the hardness of the surface. The modulus of elasticity based on measured compressive strength significantly varied from the value measured using the ultrasonic impulse. It can be caused by some degradation inside the material, which is not visible on the surface. Live load may cause such fatigue changes in material. The stress range is not very high, but the frequency of loading can reach 0.2 Hz (equivalent to about 5,000 vehicles per day), which produces a large number of loading cycles during the service life of the deck. In the case of concrete, the stress level is not very high (less than 50% of ultimate compressive strength), such that the cyclic load can cause micro-cracks develop in the matrix and between the matrix and aggregate. The fatigue degradation develops from some initial damage, which exists in a cementitious material prior to any loading. This damage is due to shrinkage, and can be different in the concrete element on the surface, as well as deeper in the section. Because of two types of shrinkage, chemical and due to drying, the deck layers close to the surface can be exposed to higher shrinkage than the rest of the slab. Once there is more initial damage in the top part of the deck, it will degrade faster under cyclic loading, and impact load from wheels. Also, the influence of chemical corrosion of rebars is more visible on the surface, because salt has easier access from the porous layer on top of the slab. All this evidence may be a reason that more damage was observed on the top surface of the deck. Also, the modulus of elasticity, measured using an ultrasonic impulse which can detect all discontinuities in material, is lower.

The test results show the great heterogeneity in the quality of concrete. The strength of concrete, checked in different places on the same deck, varies up to 30%. These weaker parts of the slab are more damageable.

Table 5-1. Deck Testing Data

Bridge No & Name	Year of Constr.	No of Applied Cycles	f'c [MPa] H-Meter	f'c [MPa] Windsor Probe	Ec [GPa] V-Meter	Deterioration (cracks, holes, delamination, corrosion)	Date
Bridge on US 223 over Raisin River in Palmyra #BO2-46062	1933 reconstruct. 1967 (32)	18,949,600	44		31.7 19.8 ratio=0.625*	Deck is in good condition, a few shrinkage cracks	5/6/99
Bridge on 475 over 175, East Branch (North to Flint) #S15 of 82195	1970 (29)	31,291,400	39 46	37 41	28.6 26.1 ratio=0.914	Transversal cracks, from 1 m to 1.75 m, irregular in spacing, deck is removed	5/14/99
Bridge on US 23, North to Ann Arbor	1962 rebuilt in 1999 (37)	42,135,600	40	39	29.7 15.6 ratio=0.527	Reinforcement is corroded, deck is removed	5/24/99
Bridge on M-66 over NYC Abandoned #RO1-78054	1965 (34)	3,387,900	38		29.4 18.4 ratio=0.625	Deck is in good condition, only a few transversal cracks going from the edge	5/27/99
Bridge on US 127 BN over Red Cedar River #BO1 of 33171	1964 (35)	3,255,000	38	45	29.4 18.0 ratio=0.615	Deck in good condition, but there were holes through the thickness which are repaired. Shrinkage cracks go in transversal direction from the external edge of the slab, spaced 1.5-2 m. The first crack is about 2.5 m from the construction joint. The quality of the deck surface is good, no cracks or delaminations.	6/14/99
Bridge on M-19 over Mill Creek in Brockway	1928 changed in 1971 (28)	4,650,000	46	38	30.1 19.7 ratio=0.636	Deck is in good condition, a few cracks, transversal from the edge.	6/24/99
Bridge on Scio Church over 194 in Ann Arbor	Deck rebuilt in Aug.99		47		30.2 18.9 ratio=0.625	Deck in very bad condition. Crushed concrete, holes, upper reinforcement without cover, delaminations, visible corrosion	7/3/99
Bridge on US 131 NB over North Park St. in Grand Rapids #SO2 of 41132	1969 (30) deck under reconstr.	26,762,000	31	30	26.2 11.3 ratio=0.43	Cracks and holes (7.5 cm in depth) on the whole deck. About 25% of the surface is destroyed.	7/24/99
Bridge on US 82 over Tamarak Creek North to Grand Rapids	1961 (38)	6,816,000	28	38	25.2 19.4 ratio=0.77	Deck is deteriorated, many potholes, which are repaired. Holes on the way of truck wheels.	9/21/99

*ratio = 0.625 was found in lab measurements

6. FINITE ELEMENT MODELS OF DECK SLAB BRIDGES

6.1 Need for analytical model

This report presents a finite element analysis of short - and medium - span deck slab bridges. There are two main goals of the research work done here. The first is to build a general numerical model, which would be easily applicable for wide range of highway bridges. Such a model can be useful in determining load rating and in estimating the behavior of bridge superstructure. Using the numerical model, it is possible to find the stress level and stress distribution in the deck slab. Also the strain values are available. This knowledge helps to investigate which parameters (live load, geometry of superstructure, materials) are essential for cracking moment in the deck. The evaluation of bridge parameters in this case is done without conducting expensive field tests. Bridge parameters are based on the collected information about the bridge and engineering experience.

The next goal is to develop an accurate model for the bridges. Material and structural parameters that can influence the numerical results, were calibrated using test data. Modeling actual bridges with known behavior is helpful to create a general model to better understand superstructure behavior. Special attention was directed to slab behavior, as slabs are cracked extensively in some bridge decks. Actual bridges were selected for a comprehensive parametric study and comparison with field test data.

The analysis was performed using ABAQUS finite element system available at the University of Michigan.

6.2 Types of finite element models for bridges

In finite element analysis the geometry of the bridge superstructure can be idealized in many different ways. The following types of models are used:

- plane grillage model,
- 3-dimensional grillage model,
- 2-dimensional model with shell elements for slab and beam elements for girders,
- 3-dimensional model with shell elements for slab and beam elements for girders,

- 3-dimensional model with shell elements for slab and girders,
- 3-dimensional model with solid elements for slab and shell elements for girders.

Most commonly used, especially in design practice, are plane grillage models Cussens (1975), Bhatt (1986). In this analysis technique the bridge deck slab is discretized into a number of longitudinal and transverse beams lying in the same plane. Each longitudinal beam represents one girder and part of the slab. The properties of such beams are determined by the position of the neutral axis, which is dependent on composite or noncomposite behavior of the bridge. A transverse grillage beam represents a strip of slab and makes the connection between longitudinal elements. Detailed recommendations on the implementation of a grillage analysis for slab bridges can be found in West (1973), Hambly (1991), Zhang and Aktan (1997). Such simple FE models allow only for a global evaluation of bridge behavior. This accuracy depends on an assumed location of the neutral axis in bending elements O'Brien and Keogh (1998). The determination of this location is difficult, especially in bridges where wide cantilevers, barriers or sidewalks cause the neutral axis to change position across the bridge width. In such cases a more complex, 3-dimensional grillage model can be used, O'Brien and Keogh (1998), Zhang and Aktan (1997). In these models, grid beams placed in two levels are connected using rigid vertical links. Although both grillage analyses represent simple geometry which is easy to model, they involve an elaborate determination of beam properties, often based on doubtful assumptions.

The evolution of FE models for bridges shows the tendency toward more complex model geometries with larger number of elements. At the same time, the determination of element properties is clearer and stands closer to reality.

The next group of models is represented by examples where the slab is discretized using shell elements and girders using beam element Mabsout et al. (1999), Hays et al. (1997). Diaphragms (if they are taken into account) are also represented by beam elements. In such plane models Mabsout et al. (1999), centroids of beams coincide with the centroid of the slab. To determine beam cross-section properties, the actual distance between its neutral axis and the middle plane of the slab must be taken into account. In 3-D models space frame elements are connected with shell elements using rigid links, which accounts for the eccentricity of the girders. It is still difficult to include precisely composite action when determining beam stiffness.

To overcome this problem, shell elements can be used to model the girders Alaylioglu and Alaylioglu (1997), Tarhini and Frederic (1992). This seems to be better solution, especially for elements such as steel girders consisting of thin parts. Sometimes there is strong influence by structural components as sidewalks, curbs and barriers on bridge behavior. In such cases it can be insufficient to model them only by changing the thickness of shell elements.

It is most realistic to use solid elements for a slab, and its sidewalks and barriers Tarhini and Frederic (1992). The application of solid elements also allows for a more detailed investigation of local stress and strain distribution. Modeling the slab with solid elements and girders and diaphragms with shell elements seems to describe most adequately the bridge geometry and physical properties.

6.3. Development of a FE model

6.3.1 Major parameters

As it is shown by included examples and is reported by other authors Schultz et al. (1995), the following parameters can have significant influence on the results.

- MESH – idealization of geometry and physical properties of the bridge depending on the type and number of elements.
- MATERIAL – data for steel and concrete. As it is shown later different material properties are needed for different kind of analyses.
- BOUNDARY CONDITIONS – evaluation of the actual constraints in the supports.
- INTERACTION – simulation of interaction between different elements especially girders and slab causing composite or noncomposite action.
- LOADS – different types of loading are concerned: dead and live loads, dynamic loading, temperature and shrinkage. This is important to determine in a proper way the value and position of the loads distributed to the nodes.

All of the following parameters are discussed and their influence on the results is included using examples. Calibration, meaning assessment, of the model parameters based on the comparison of numerical results with test data is also presented.

6.3.2. General description of a model

Geometry

A typical FE model for a deck slab bridge used here is presented in Figure 6.1. Longitudinal (traffic) direction is noted as X or 1 and transverse direction is named Y or 2. Z or 3 refers to the vertical direction of the superstructure. Two or four layers of solid elements represent deck slab (Figure 6.2). All of these elements have the same length.

$$\Delta L_e = L/n_e, \tag{6-1}$$

where L is the total length of the bridge and n_e is the number of rows of the elements (for slab and girders) in longitudinal direction X. For all calculations presented here, $n_e = 24$.

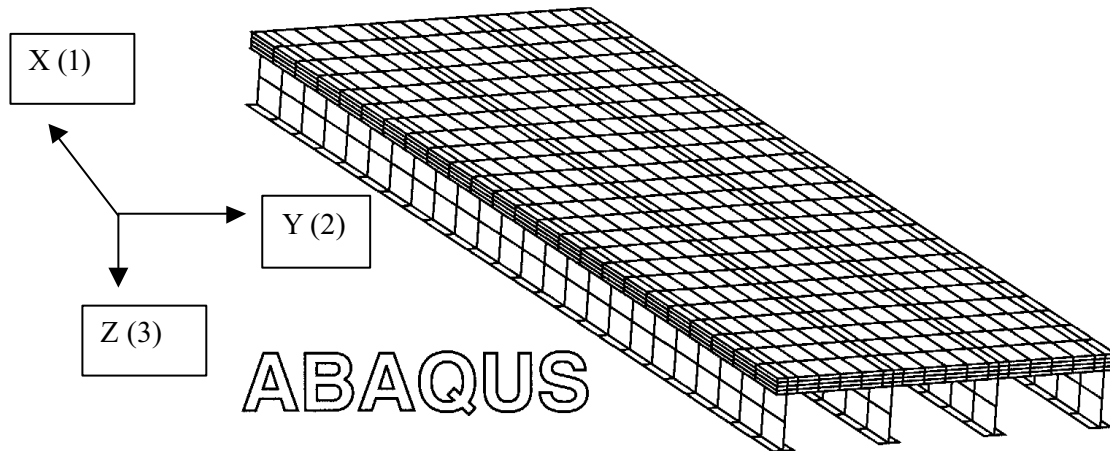


Figure 6.1 Isometric view of FE model for deck slab bridge.

The nodal representation of live loads is strictly connected with n_e . The width of the elements (dimension in transverse direction noted as Y or 2) varies depending on the distance between girders, the flange width and on the transverse dimensions of edge parts of the slab such as curbs and barriers (if they are taken into account). Usually, the slab strip touching the upper flange is divided into two elements and the part of the slab between two flanges is divided into four rows of elements (Figure 6.2). These numbers can be easily changed. The transverse division of the sidewalk depends on its width and the position of the first girder.

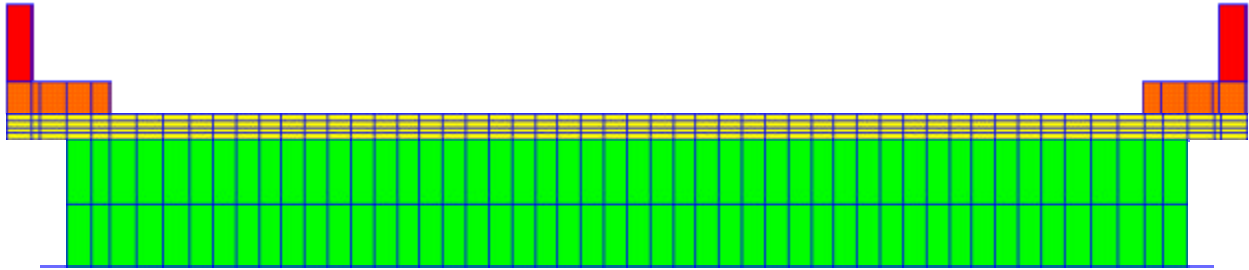


Figure 6.2 Cross-section of the FE model.

The barrier is represented by 24 elements forming one longitudinal row. The transverse dimension (width) b of these elements is calculated using the idealization of an actual barrier presented in Figure 4.3. b [mm] is determined in such a way that the moment of inertia calculated according to the middle axis of the slab is the same for the idealized and actual barrier. The depth is assumed to be the same.

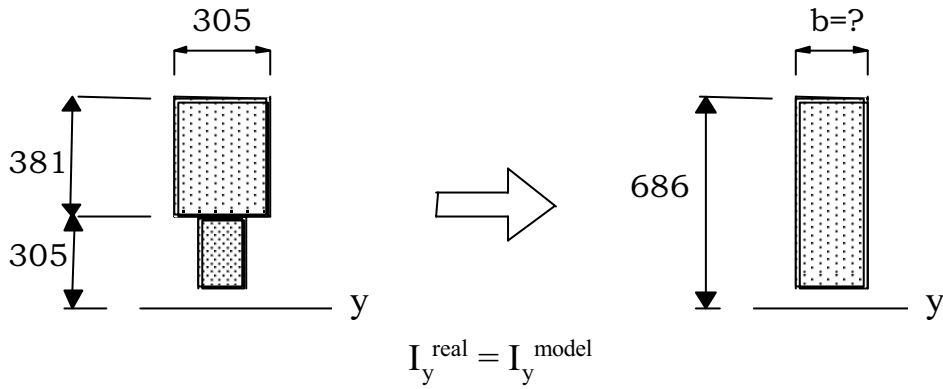


Figure 6.3 Idealization of a barrier in the model.

Girders are modeled using shell elements. As shown in Figure 6.4, the cross-section of a girder is divided into 6 elements. This is the coarsest division used and it can be easily refined. This means that one girder in the model has at least $6 \times 24 = 144$ elements.

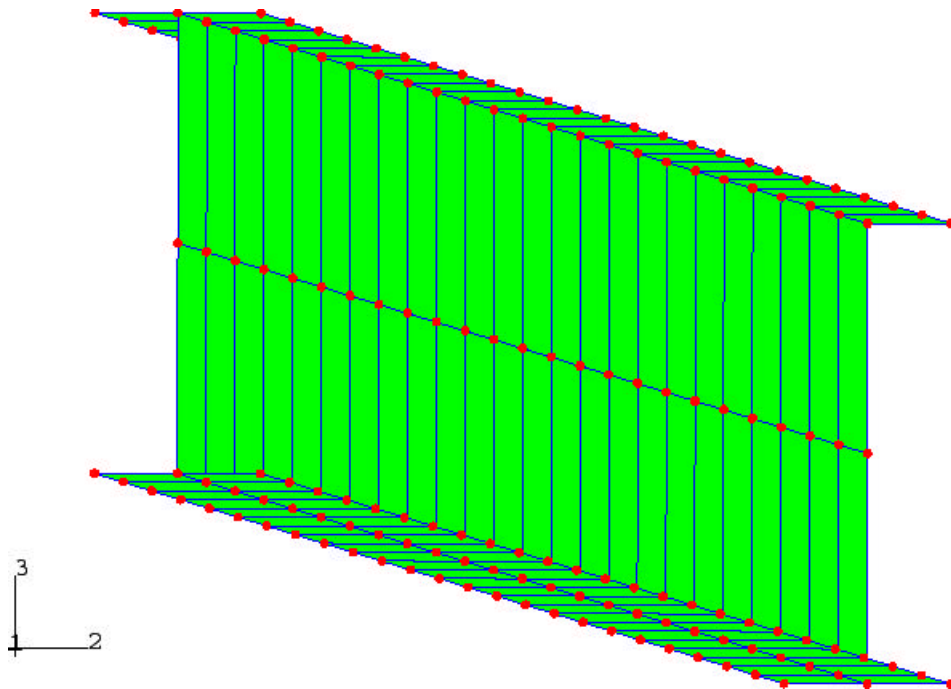


Figure 6.4 Girder modeled with shell elements

In highway bridges there are different kinds of transverse bracing used between girders. Steel and concrete diaphragms are modeled using shell elements with the same transverse division as in the slab and two layers in Z direction (Figure 6.5). Transverse bracing is represented by beam elements. Sometimes better results are received without diaphragms, especially for old bridges with concrete diaphragms. The influence of concrete diaphragms on girder deflections is sometimes very small and can be neglected. After many years of service and cyclic deformations caused by temperature changes, the bonding between the concrete diaphragms and steel girders can be drastically reduced, especially if there are no additional steel connectors. These diaphragms still provide protection against transverse buckling of the girders however. In the model, shell elements representing diaphragms are connected with girder elements at the same nodes. Such a connection may give too stiff of a response of the superstructure.

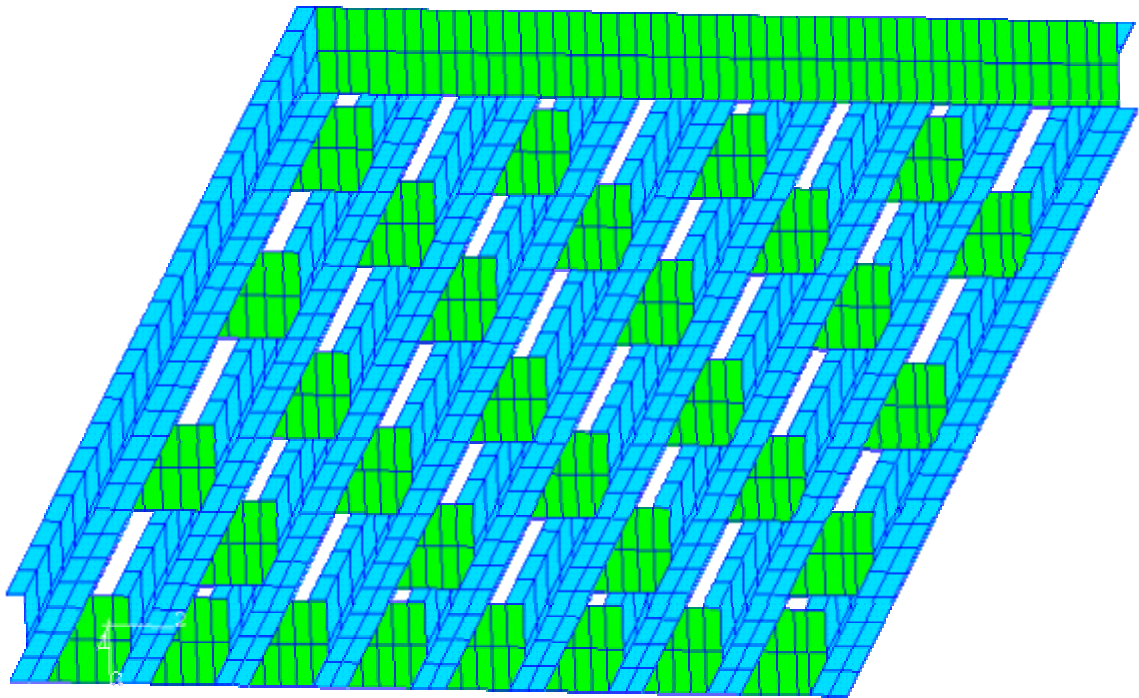


Figure 6.5 Girders and diaphragms modeled with shell elements

Material properties

The basic materials include structural steel, reinforcing steel and concrete. The user selects the following input data:

$E_s = 2 \cdot 10^5$ MPa – modulus of elasticity of steel,

$\nu_s = 0.3$ - Poisson's ratio of steel,

f_Y - yield stress of steel.

The stress – strain relationship for steel is shown in Figure 6.6. The same material model is used for structural steel and reinforcing bars although different values for f_Y can be specified. This model is included in the ABAQUS program.

Material model for concrete used in ABAQUS is more complex. This is described by the following data:

E_c - modulus of elasticity of concrete,

ν_c - Poisson's ratio of concrete,

f_{c1}' - compressive stress defined as the elastic limit (for zero plastic strain) (Figure 6.7),

f_{c2}' - ultimate concrete stress (peak stress) (Figure 6.7),

ϵ_{c2} – strain corresponding to f_{c2}' .

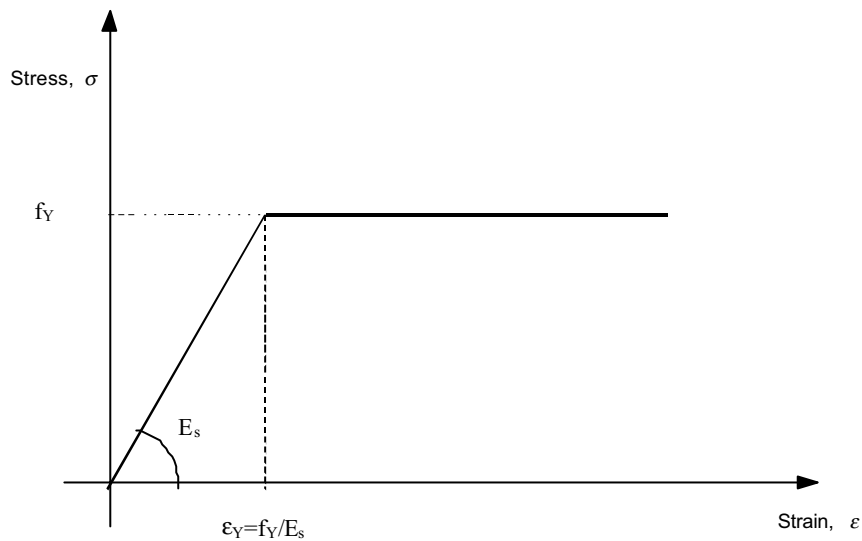


Figure 6.6 Stress-strain curve for steel

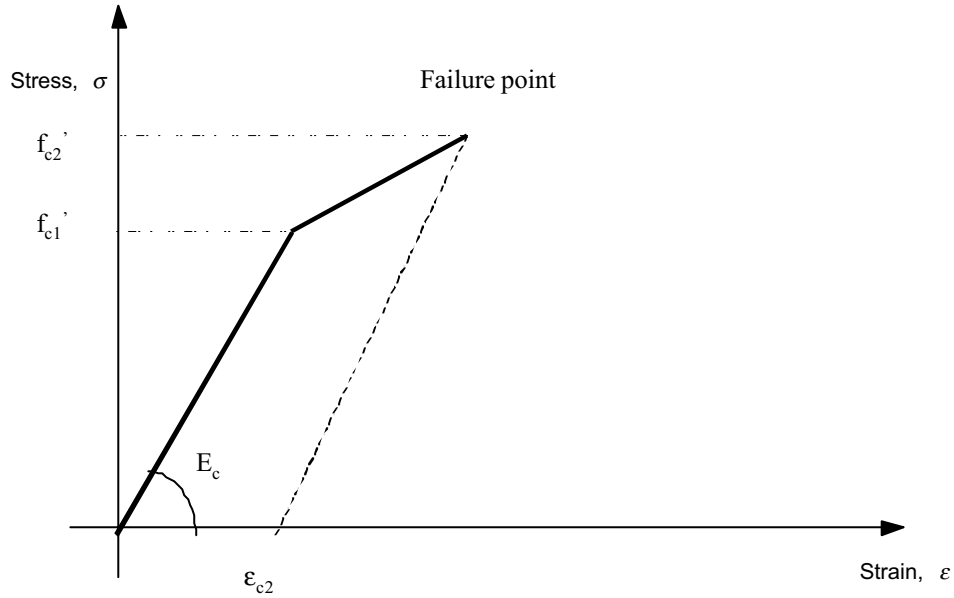


Figure 6.7 Stress-strain curve for uniaxial compression used in ABAQUS/Standard User's Manual (1996)

The concrete behavior is modeled in ABAQUS as a smeared crack model, which does not involve individual “macro” cracks. The strain-softening behavior for cracked concrete is determined by the user who has to define at least two parameters; fraction of remaining stress to stress at cracking, and the absolute value of direct strain minus the direct strain at cracking. This way the user specifies the postfailure stress as a function of strain across the crack (Figure 6.8). In the presented work a linear reduction of stress after failure is assumed. For standard concrete, strain at failure is usually 10^{-4} and the total strain, which reduces stress to zero, is 10^{-3} ABAQUS/Standard User's Manual (1996).

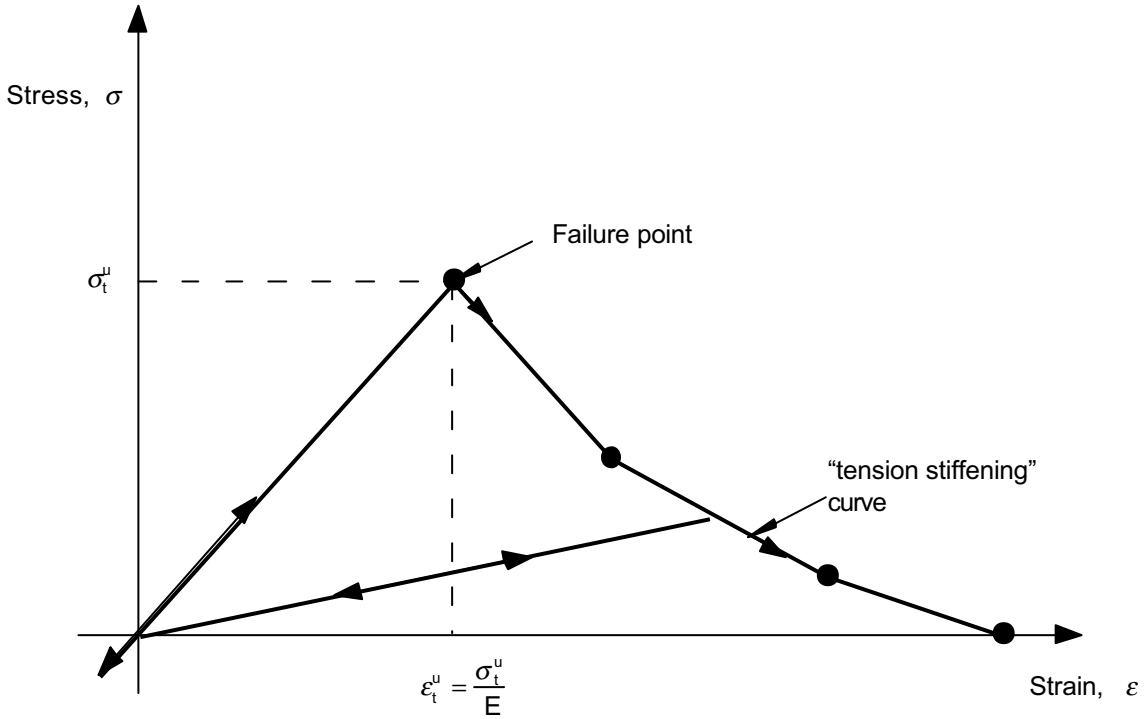


Figure 6.8 Tension stiffening model.

The multiaxial stress surface of failure is shown in Figure 6.9 ABAQUS/Standard User's Manual (1996). The user can define the behavior of concrete with the following ratios:

$\rho_1 = \frac{\sigma_{bc}}{\sigma_{uc}}$ - where - σ_{bc} is the ultimate biaxial compressive stress and σ_{uc} is the ultimate uniaxial compressive stress,

$\rho_2 = \frac{\sigma_{ut}}{\sigma_{uc}}$ - where - σ_{uc} is the value of the uniaxial tensile stress at failure and σ_{uc} is the absolute value of the ultimate uniaxial compressive stress,

$\rho_3 = \frac{\epsilon_{bc}}{\epsilon_{uc}}$ - where - ϵ_{bc} is the principal component of plastic strain at ultimate stress in biaxial compression and ϵ_{uc} is the plastic strain at ultimate stress in uniaxial compression,

$\rho_4 = \frac{\epsilon_{tb}}{\epsilon_{tu}}$ - where - ϵ_{tb} is the tensile principal stress at cracking in plane stress and ϵ_{tu} is the tensile cracking stress under uniaxial tension.

If the above ratios are omitted by the user, default values are applied by ABAQUS.

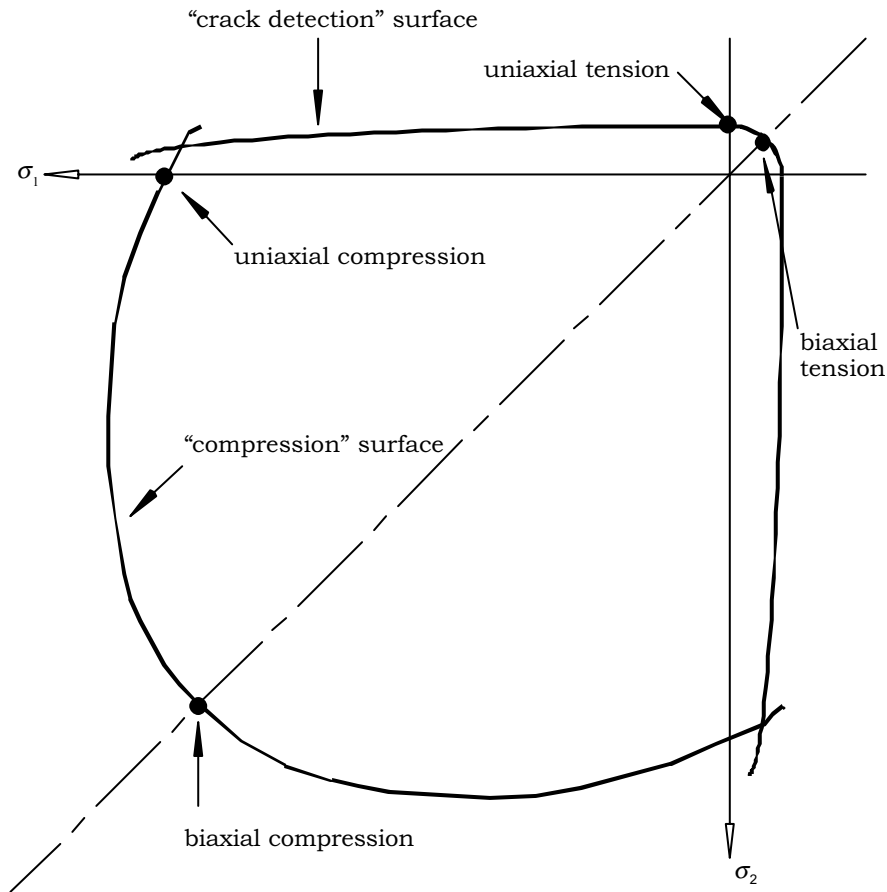


Figure 6.9 Yield and failure surfaces in plane stress

Additionally, the user can specify to diminish the shear stiffness in cracked concrete. This option was omitted in this analysis and the default shear response, unaffected by cracking, was used.

In all of the presented models, reinforcement is defined as two layers of uniformly spaced reinforcing bars. The position of these layers in slab elements and the amount of steel are determined according to the available plans of modeled bridges (Figure 6.26).

In static analysis where actual (not ultimate) dead and live loads are applied, tested bridges show linear elastic behavior. This means that only elastic properties for steel and concrete influence the results. For the ultimate load carrying capacity, the inelastic range is also

investigated. It is difficult, especially for concrete, to determine the actual values of all of these parameters. In such cases average values as reported in the literature can be used.

Boundary conditions

All bridges investigated here are one span superstructures, designed as simply supported. In old bridges, corrosion of the bearings usually causes additional constraints both for rotations and longitudinal displacements. Examination of these examples verified what was also reported by other authors Schultz et al. (1995), that even slight changes in boundary conditions have large effects on the results. To improve support conditions in the model, additional linear elastic spring elements were introduced as shown in Figure 6.10. Springs are attached to the bottom and upper flanges on the ends of each girder. The magnitude of stiffness k was calibrated with field measurements. A comparison of calculated strain values with test data enables the determination of k . Different values of spring stiffness for different girders can also be applied.

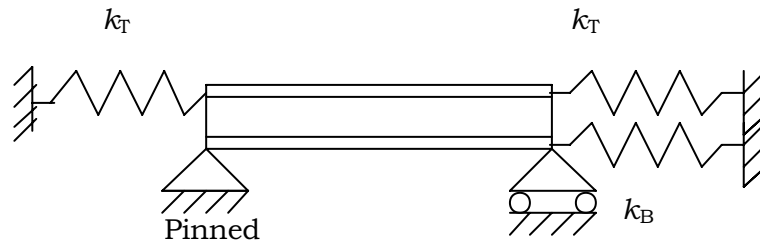


Figure 6.10 Girder simply supported with spring elements.

If test data is not available, theoretical assessment of k can be made. This should be based on the visual inspection of bearings and engineering experience. The process is as follows: first longitudinal displacement and rotations at the girder are calculated without spring elements in the model. Then the magnitude of the stiffness k is determined in such a way that it gives elastically constrained displacements and rotations, which are smaller than the displacements and rotations calculated without constraint.

Composite action

Most of the old slab on girders bridges were designed as noncomposite superstructures. This means that to estimate the maximum stresses induced by bending moments, only steel girders (without concrete slab) were taken into account. Field tests by Schultz et al. (1995) proved that even

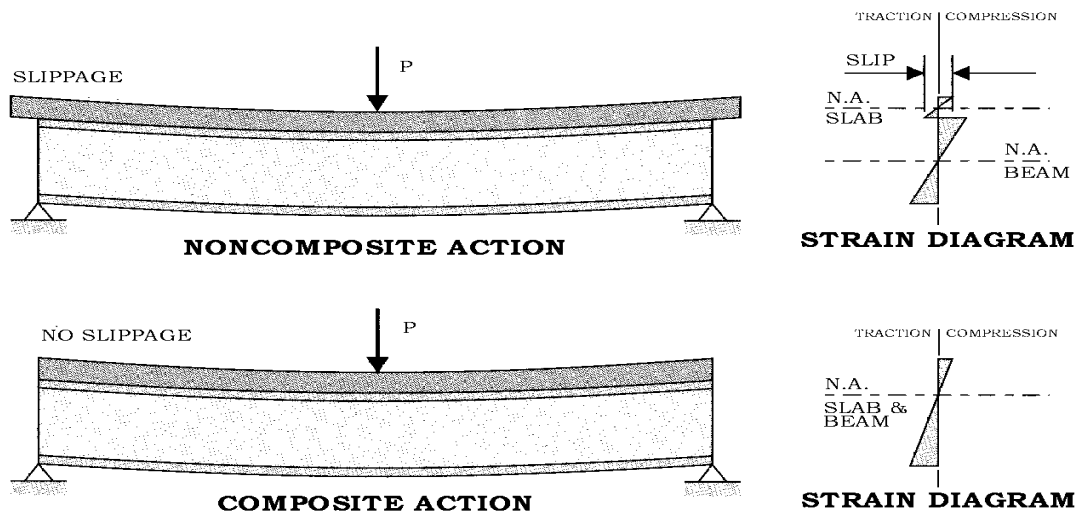


Figure 6.11 Noncomposite and composite action

though there are usually no shear connectors in such old bridges, there is still bonding between the concrete-steel interface. The difference between noncomposite and composite behavior is shown in Figure 6.11. Composite action changes the position of the neutral axis and increases the cross-sectional moment of inertia. It increases the stiffness and diminishes the maximum compression stress. However, the change in strain in the bottom flange caused by live load is usually very small (Figure 6.11). This implies that to investigate the composite behavior during the test, additional strain measurements on the upper flange (or upper part of the web) should be done Schultz et al. (1995).

Composite action is present when there is no slippage between the slab and upper flange. Usually bonding between concrete and steel on the contact surface is enough to carry shear forces induced by dead and live loads. To improve this connection steel shear connectors are used in modern bridges to increase the load limits allowed for composite action.

To model fully-composite behavior, the same nodes are used for upper flange shell elements and for solid elements that form the bottom layer of the slab (Figure 6.12).

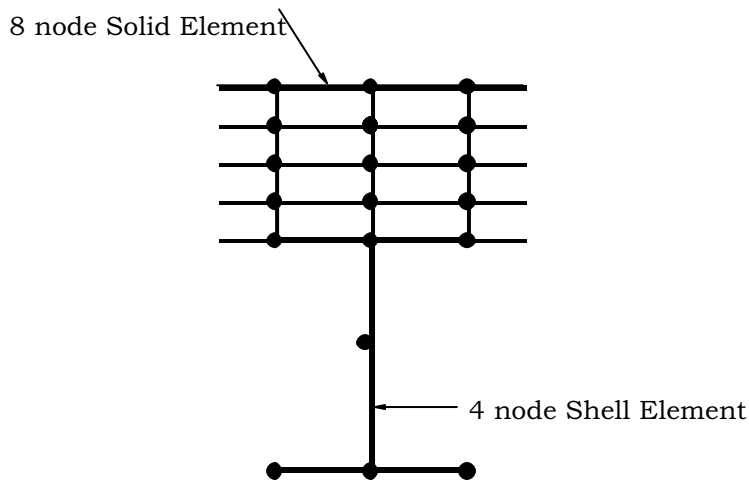


Figure 6.12 Fully composite model.

To model noncomposite or partially composite behavior, the Multi Point Constraints (MPC) option available in ABAQUS is used. This allows imposing constraints between different degrees of freedom of the model. Choosing the type of MPC, the user can define the type of bonding in concrete-steel interface.

Usually composite action is assumed for the investigation of bridge behavior under traffic loads. But when an ultimate load carrying capacity analysis is done noncomposite action is considered Schultz et al. (1995). This is because the bond between concrete and steel would likely fail prior to yielding of the steel. In Schultz et al. (1995), a shear stress of 100 psi for flanges is recommended as a limit for the use of unintended composite action.

Loads

The following loads are included in the presented investigation:

- dead load,
- live load,
- temperature.

Dead load includes the weight of structural and nonstructural components. The weight of structural elements such as slab, sidewalks, barriers, girders and diaphragms is calculated using their volume and material density. The following densities are used:

$$\rho_s = 7.69 \cdot 10^3 \text{ kg/m}^3 \text{ - for steel,}$$

and

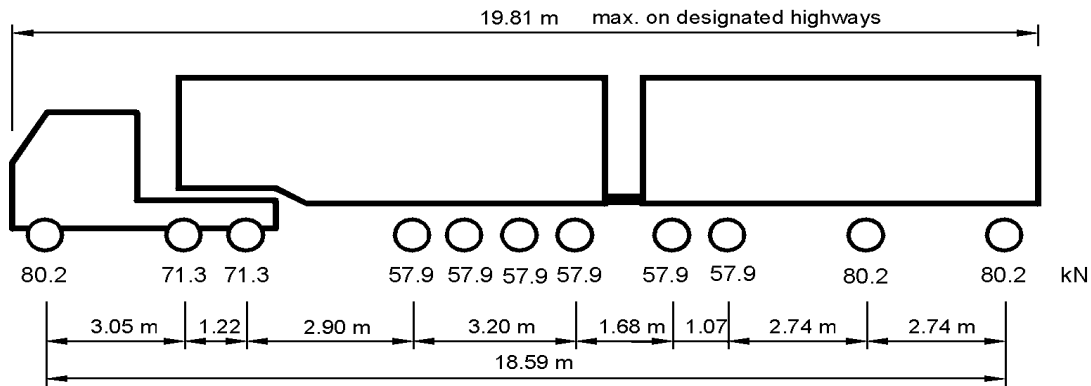
$$\rho_s = 2.50 \cdot 10^3 \text{ kg/m}^3 \text{ for reinforced concrete.}$$

The weight of asphalt overlay (if used) can be included as a uniform pressure applied to the upper face of the solid elements forming the first layer of the slab. The magnitude of this pressure is

$$p_a = \rho_a \cdot h, \tag{6-2}$$

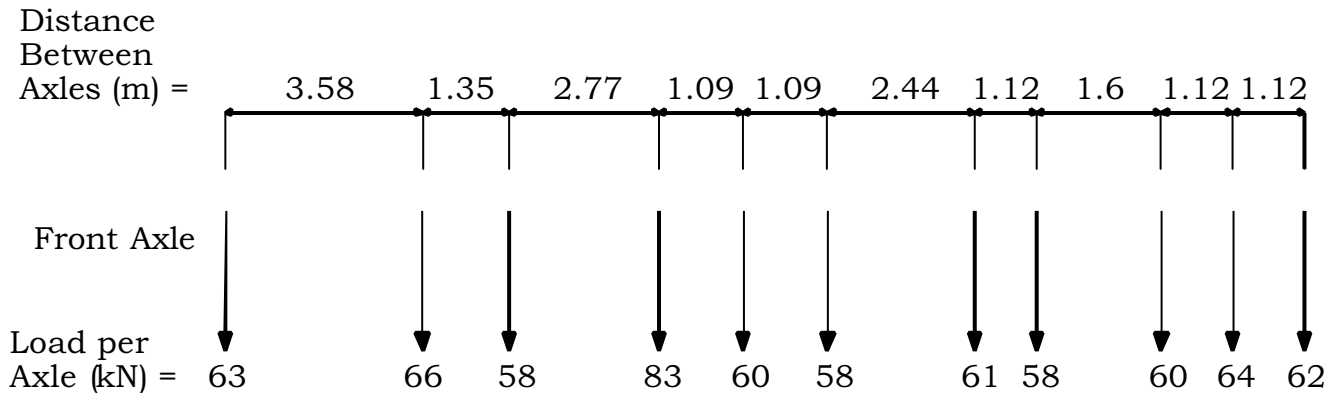
where $\rho_a = 1.3 \cdot 10^3 \text{ kg/m}^3$ is the asphalt density and h is the thickness of asphalt overlay in meters. Other elements such as equipment are not considered in the dead load assessment.

Live loads applied in the form of load 11-axle, three unit trucks (which corresponds to load used during the test). An example of such a truck used in Michigan is presented in Figure 6.13. Such trucks were used as load during field tests. For each truck, the axle weight and spacing were measured. In this way the load configuration, consisting of 22 concentrated forces, was determined as shown in Figure 6.14.



MICHIGAN 11 AXLE THREE UNIT MAX. 730.6 kN

Figure 6.13 Example of Michigan 11 axle three unit truck.



Gross Vehicle Weight = 693 kN

Wheelbase = 17.18 m

Figure 6.14 Typical truck configuration.

For each test run, the transverse position of the truck was measured. Two truck positions are used for each traffic lane: close to the curb and middle of the lane as shown in Figure 6.15.

Longitudinal positions of the trucks could not be measured during the test. The position of loading which gives extreme values of recorded strains and displacements has to be determined first. This was calculated as the position producing the maximum bending

moment at midspan, where strain transducers were located. Figure 6.16 shows bending moment diagrams for different positions of the truck. On the horizontal axis, the location of the first truck axle is given. This is changing using an increment equal to eq. (6-1) and is applied with an assumed longitudinal division of the span into 24 elements. Bending moment at the midspan is calculated using influence curves for the bridge span treated as a simply supported beam.

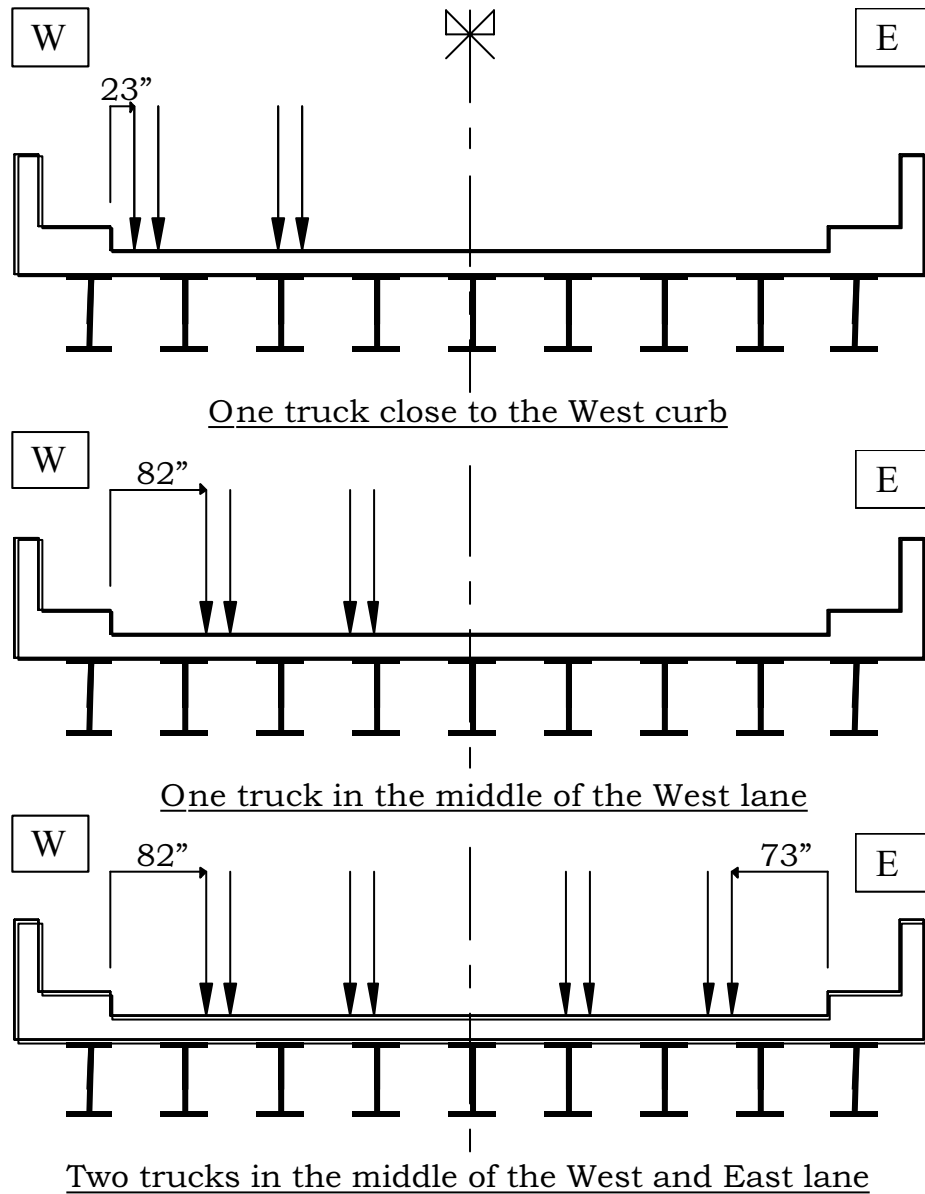


Figure 6.15 Transverse truck positions.

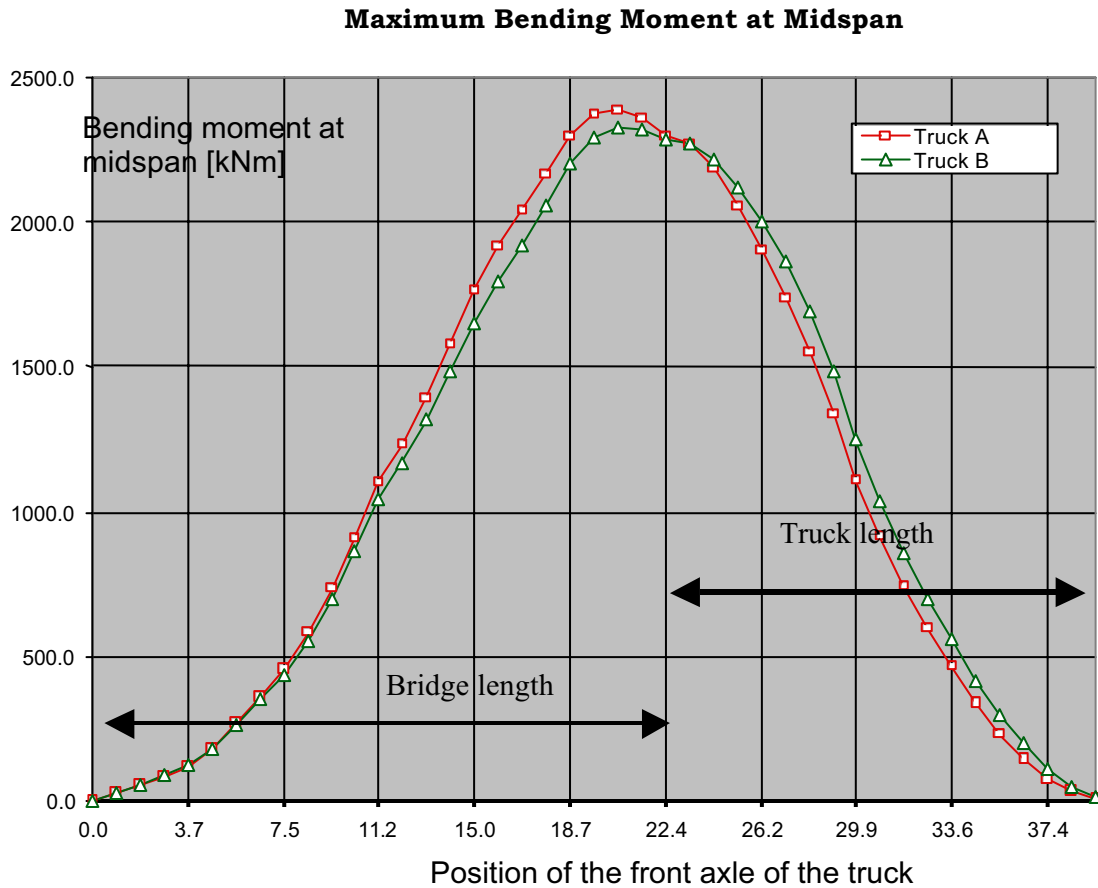


Figure 6.16 Determination of the longitudinal truck position giving the maximum bending moment at midspan.

After determining the truck position on the bridge, concentrated loads are distributed to adjacent nodes in the way presented in Figure 6.17. In this way 22 concentrated wheel loads for one truck are exchanged into 88 equivalent concentrated forces applied to the model nodes.

Temperature loading is determined by temperature gradients defined for the node sets. The same temperature gradient equal to 15 °C is used for the upper part of the deck consisting of barriers, sidewalks and the upper surface of the slab. This is assumed that temperature

gradient in girders, diaphragms and in the bottom surface of the slab is equal to 0 °C. The change of the temperature in the slab thickness is linear. The following thermal expansion coefficients are used:

$$\epsilon_{Ts} = 0.00001 \text{ 1/}^\circ\text{C} \text{ – for steel,} \tag{6-3}$$

$$\epsilon_{Tc} = 0.000001 \text{ 1/}^\circ\text{C} \text{ – for concrete.}$$

Above values allows ABAQUS to calculate strains and stresses caused by thermal expansion.

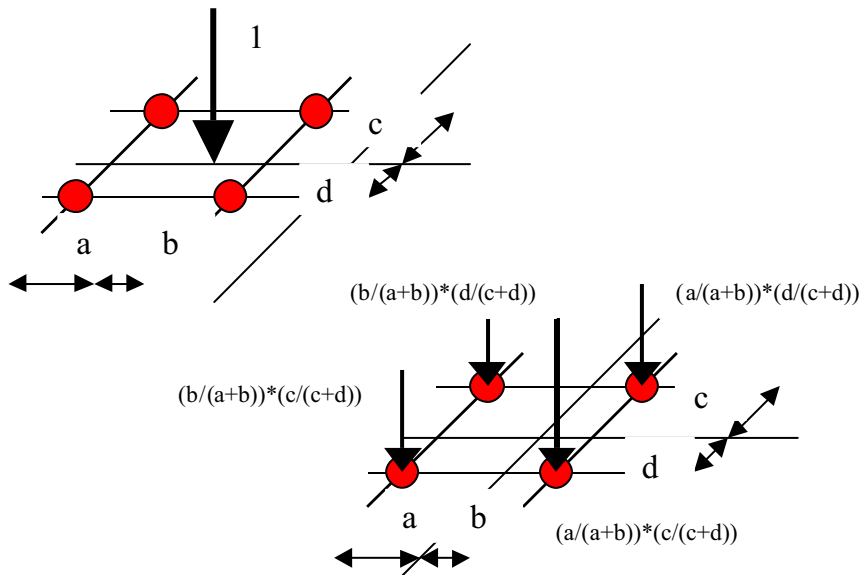


Figure 6.17 Distribution of a concentrated load to adjacent nodes.

6.3.3 Geometry of modeled bridge

An existing bridge was selected to build the numerical model of the superstructure. The bridge was tested under truck load. Strains in girders and the maximum deflection were measured. The test data was used to validate the finite elements model, especially to model boundary conditions for girders. The support conditions should be properly modeled because they strongly affect the behavior of the deck slab.

The bridge designated as M19/MC is located on M-19 over Mill Creek in Brockway, Michigan. This bridge was built in 1928 and rebuilt in 1971. As shown in Figures 6.18 through 6.20 the bridge has two traffic lanes; West (South bound) named W and East (North bound) named E. This was designed as a simply supported single span structure consisting of concrete deck slab, nine steel girders and concrete diaphragms. The total span length is 22.9 m without skew. The span length between supports is 22.4 m. The bridge has a longitudinal grade of 4.421 % from North to South. Figure 6.20 shows cross-section of the bridge that was designed as a composite section. The average thickness of the slab is 227 mm without the asphalt overlay. Figure 6.20 shows the reinforcement in the slab. As shown in Figure 6.20, inside girders are spaced at 1220 mm and outside at 1296 mm. Outside girders have bigger sectional areas due to additional plates in the flanges.

The deck slab is in good condition probably because of the slope and good water drainage. Only few small cracks were found during visual inspection. Corrosion was observed at the support areas.

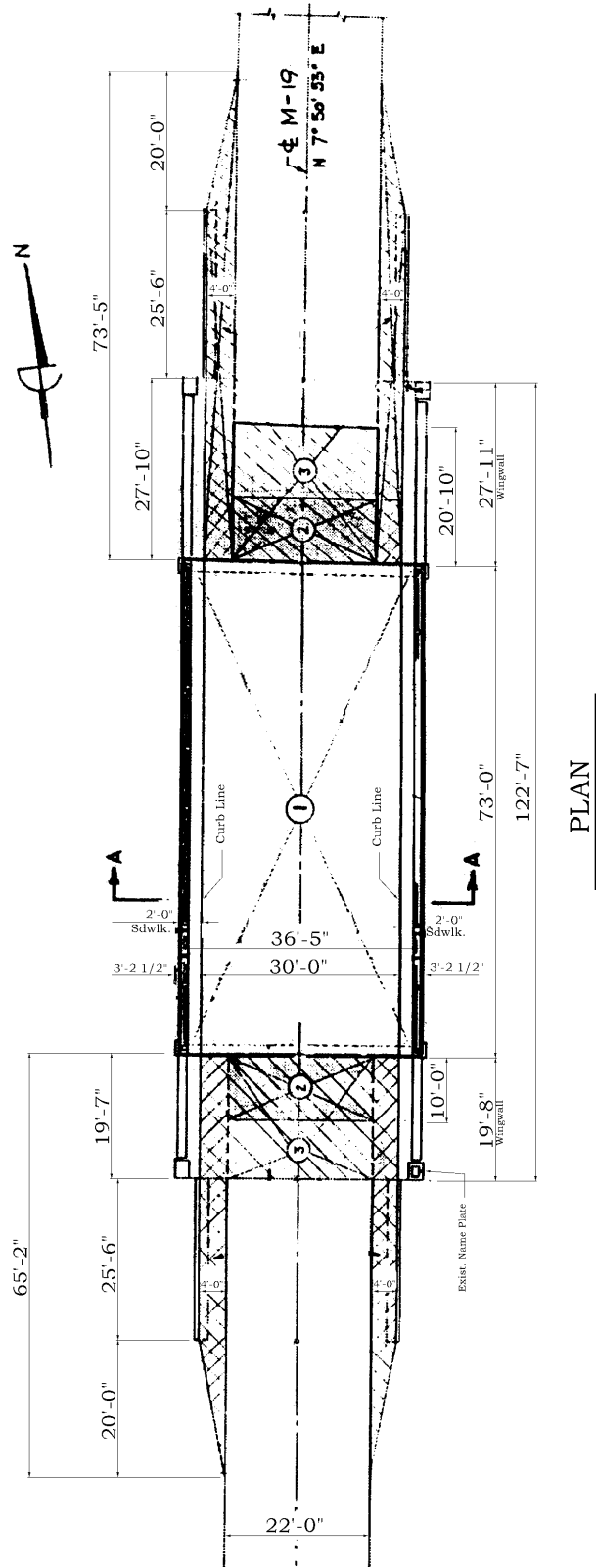


Figure 6.18 – Plan View of the Bridge M-19 over Mill Creek in Brockway
(conversion factor for SI units: 1' = 0.305m, 1" = 0.025m)

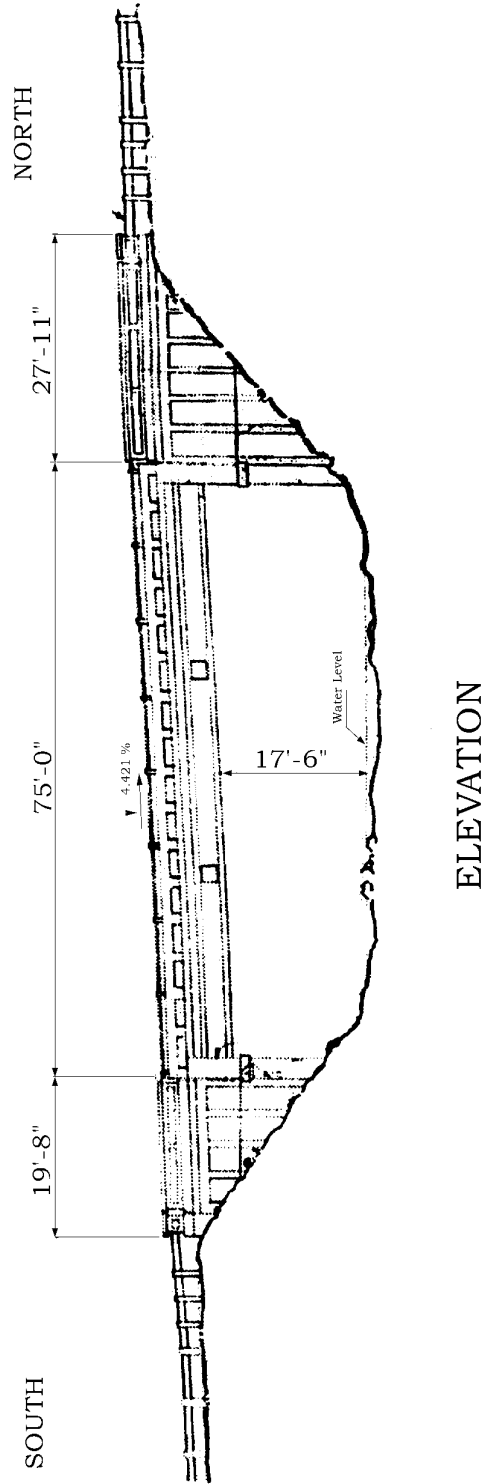
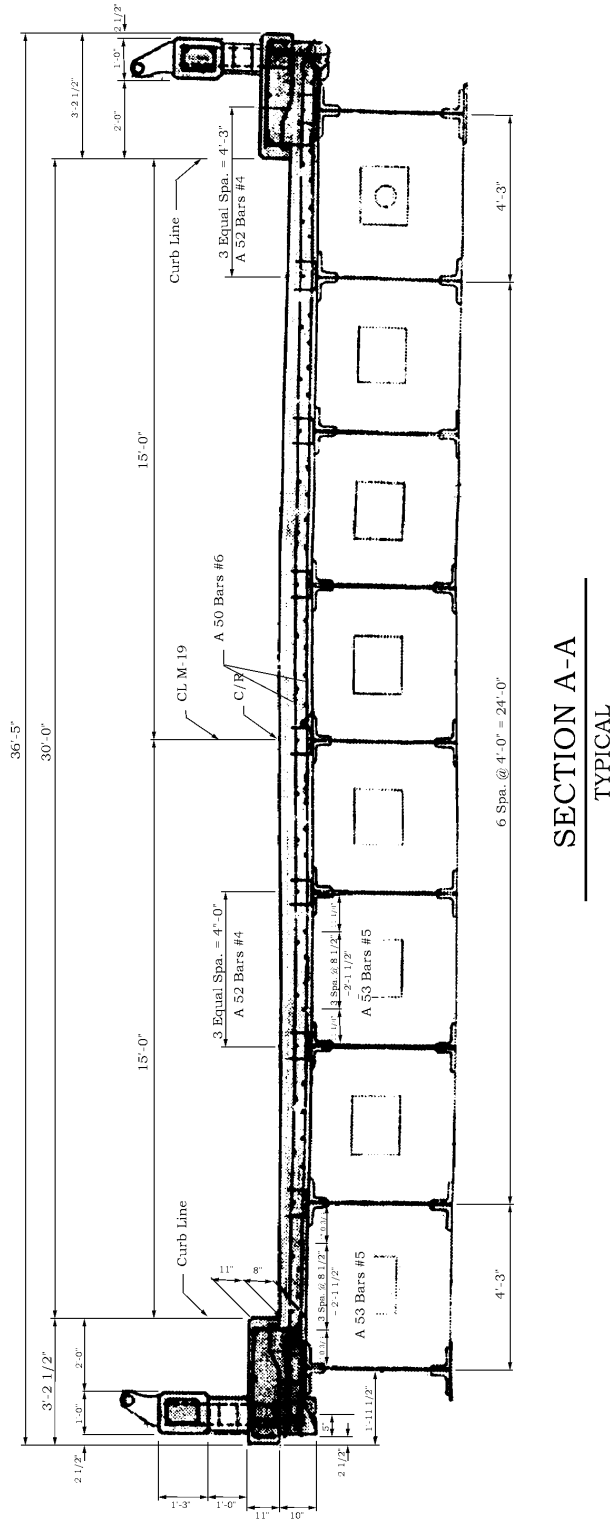


Figure 6.19 – Elevation of Bridge M-19 over Mill Creek in Brockway
(conversion factor for SI units: 1' = 0.305m, 1" = 0.025m)



SECTION A-A
TYPICAL

Figure 6.20 – Section A-A of Bridge M-19 over Mill Creek in Brockway
(conversion factor for SI units: 1' = 0.305m, 1" = 0.025m)

6.3.4 Field test

The field test was performed on June 24, 1999. Strain transducers were installed on the bottom flanges of girders in the middle of the span and close to the supports as it is shown in Figure 6.21. Two gravel hauling trucks, A and B were used with axle configurations as shown in Figures 6.22 and 6.23. The test included 16 runs. Each run is described in Table 6.1 where transverse position and speed are given. There were two transverse positions for each truck, close to curb named WC for West lane and EC for East lane and center of lane named EL or WL. For every run precise transverse position of the truck was measured.

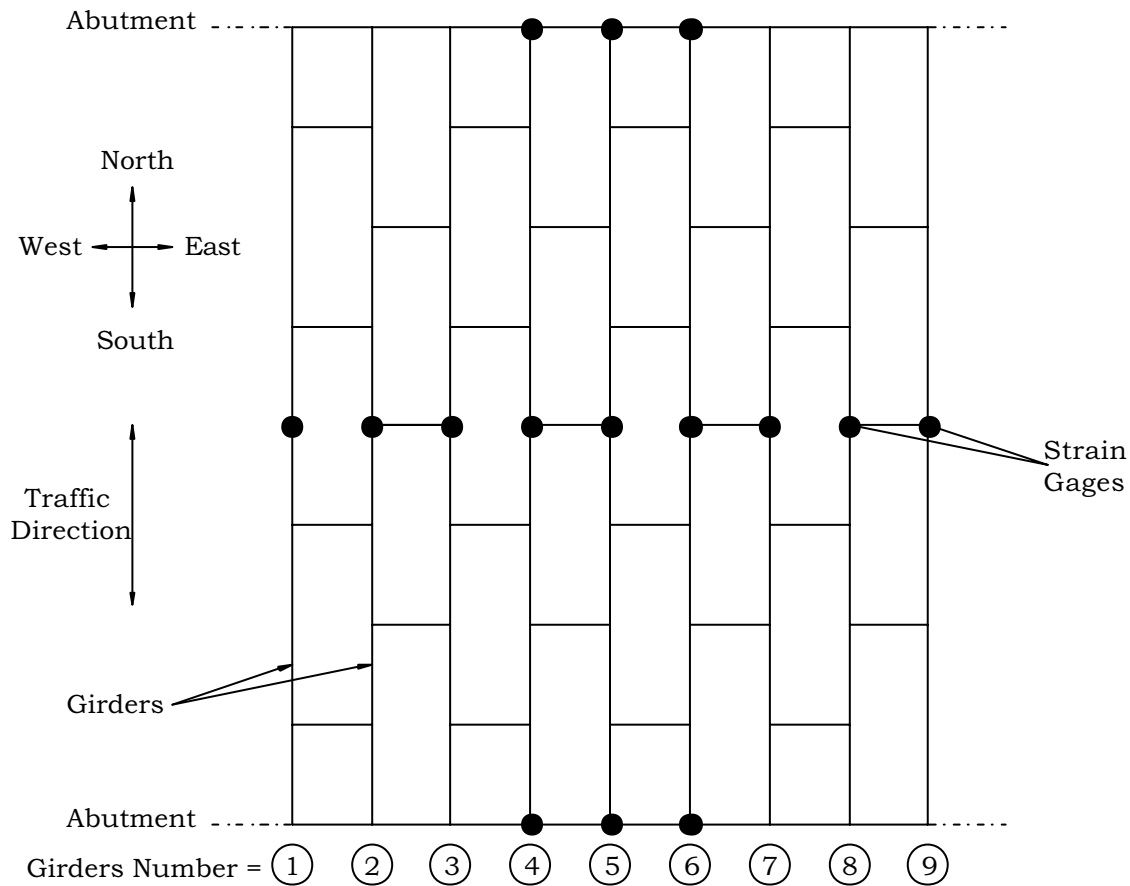


Figure 6.21 – Strain transducer locations in Bridge M19/MC in Brockway.

Table 6.1 Sequence of runs over the bridge

Run #	Truck	Lane	Position in lane	Transverse distance	Truck speed
1	truck A	East	Center	1.52 m	Crawling
2	truck A	East	Curb	0.53 m	Crawling
3	truck B	East	Center	1.91 m	Crawling
4	truck B	East	Curb	0.53 m	Crawling
5	truck B	East	Center	2.21 m	46 km/h
6	truck A	East	Center	2.08 m	53 km/h
7	truck A	West	Center	2.08 m	Crawling
8	truck A	West	Curb	0.58 m	Crawling
9	truck B	West	Center	2.08 m	Crawling
10	truck B	West	Curb	0.58 m	Crawling
11	truck B	West	Center	2.11 m	Crawling
12	truck A	West	Center	2.21 m	40 km/h
13	truck A & truck B	Both	Center	truck A 2.08 m truck B 1.85 m	40 km/h
14	truck B & truck A	Both	Center	truck B 1.91 m truck A 1.88 m	Crawling
15	truck A & truck B	Both	Center	truck A truck B	37 km/h
16	truck B & truck A	Both	Center	truck B truck A	56 km/h

. Table 6.2 Maximum microstrains measured during the test.

Run #	Load configuration	Girders								
		1	2	3	4	5	6	7	8	9
1	Truck A EL 1.52 m	3.355	11.74	26.37	38.09	49.76	52.5	54.36	44.9	32.53
2	Truck A EC 0.53	-1.04	3.7	14.9	22.4	36.2	42.6	57.1	57.4	60.1
3	Truck B EL 1.91 m	2.8	11.63	26.3	36.98	48.8	50.35	53.8	44.98	33.65
4	Truck B EC 0.53 m	-1.73	3.7	14.5	21.7	34.2	39.8	55.4	56.4	59.5
5	Truck B EL 2.21 m H Speed	1.73	9	23.6	33.1	47.2	47	52.7	44.3	34.7
6	Truck A EL 2.08 m H Speed	2.8	10.6	26.3	37.5	50.7	49.8	53.24	44.3	31.96
7	Truck A WL 2.08 m	33.3	40.9	56.4	61.5	48.8	35.6	22.5	15.4	3.84
8	Truck A WC 0.58 m	59	54	56.6	51.3	33.4	22.4	10.8	6.7	-0.5
9	Truck B WL 2.08 m	32	39.2	54.8	59.3	48.2	35.9	22.8	15.5	4.3
10	Truck B WC 0.58 m	58.4	53.7	55.1	50.1	33.1	22.3	10.67	6.95	-1
11	Truck B WL 2.11 m H Speed	29.6	37.8	54	59	49.6	35.9	23.4	15.3	4.3
12	Truck A WL 2.21 m H Speed	29	39.8	54.6	58.9	49.7	36.7	23.6	14.9	3.3
13	Truck A 2.08 m Truck B 1.85 m	35.4	50.5	81.2	95.9	96.4	85.8	76.8	61	38.4
14	Truck B 1.91 m Truck A 1.88 m	34.8	50.5	79.6	94.2	95.3	85.3	75.3	59.9	35.1
15	Truck A W Truck B E HS	39.1	54	83	97.4	97	84.9	73.8	57.5	33.5
16	Truck B W Truck A E HS	35	50	81	95.9	98.9	86	77	62	40

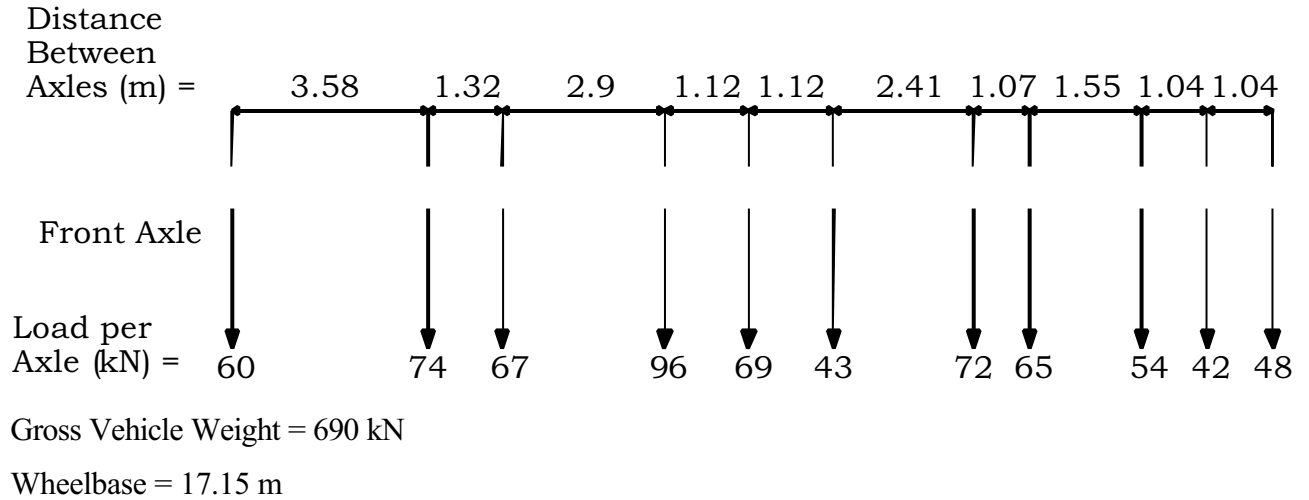


Figure 6.22 – 11-Axle Truck A configuration, Bridge M-19 over Mill Creek in Brockway.

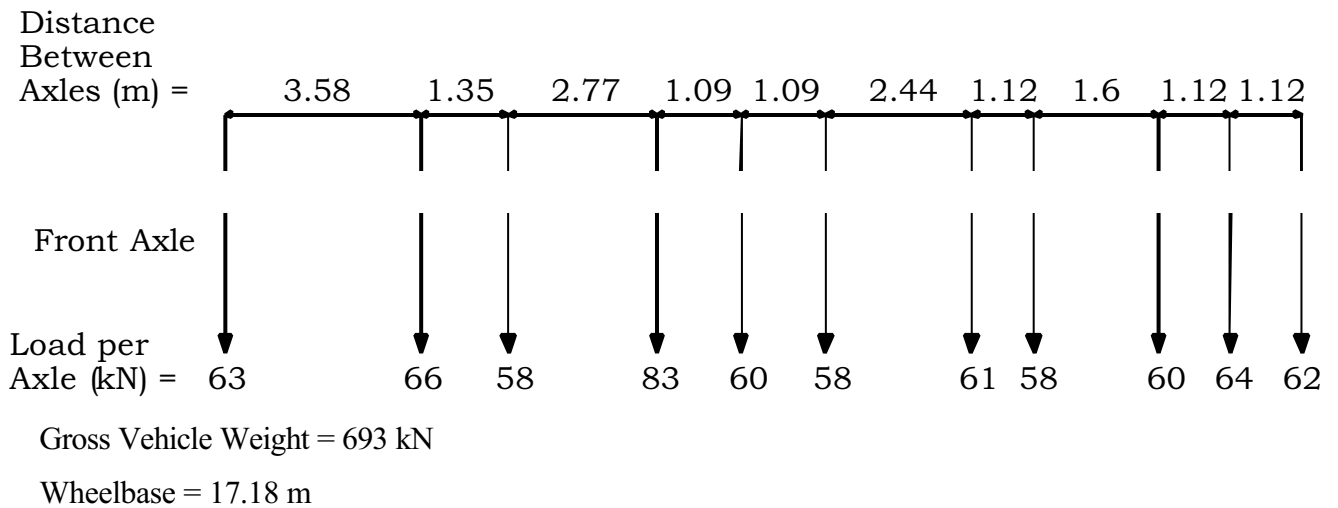


Figure 6.23 – 11-Axle Truck B configuration, Bridge M-19 over Mill Creek in Brockway.

6.3.5 Description of FE model

Table 6.19 presents microstrains measured during the test. Presented results are used for comparison with numerical values in the calibration process.

The FE model for M-19 bridge over Mill Creek is presented in Figure 6.24. The deck slab is modeled using four layers of 8-node solid elements. An additional layer is used for each sidewalk and one longitudinal row of elements for each barrier. The transverse division of elements, their dimension and spacing are presented in Figure 6.25. All elements have the same longitudinal dimension

$$\Delta L_e = 0.935 \text{ mm,}$$

calculated according to (6-1).

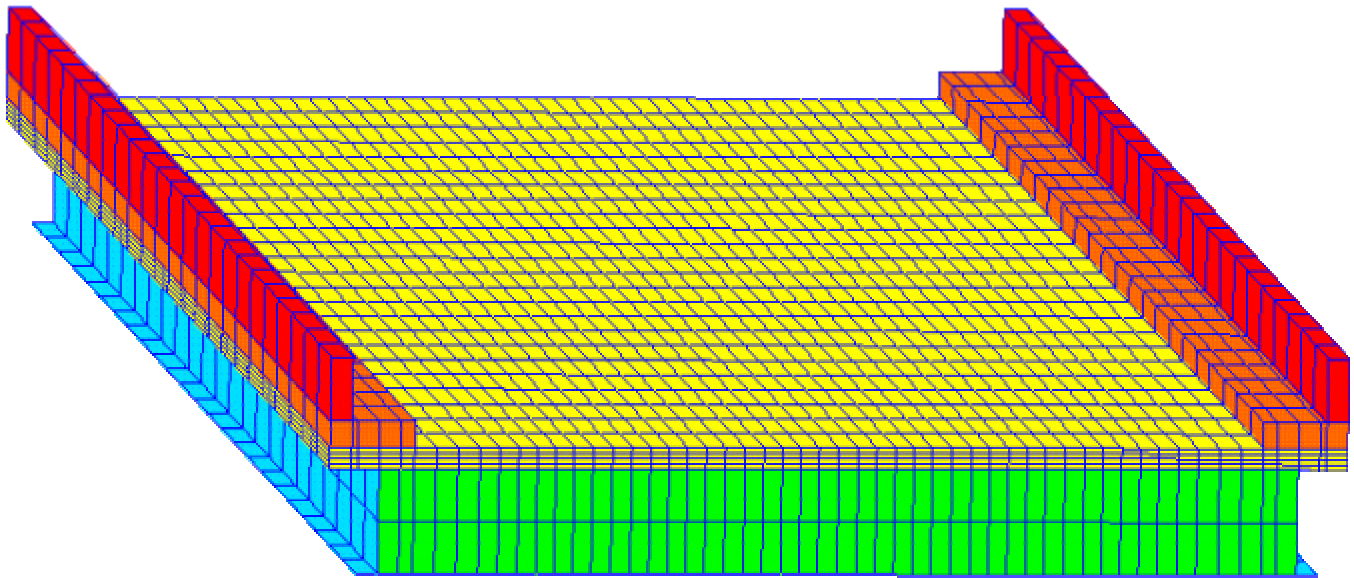


Figure 6.24 Isometric view of FE model

Four layers of uniformly distributed reinforcement were applied in the solid elements forming the slab. The position of reinforcement is shown in Figure 6.26. The same amount of steel was used for both directions, transverse and longitudinal, in the top and bottom layers. According to available bridge structural drawings, the reinforcement consists of 19

mm diameter bars spaced at 203 mm. The reinforcement is modeled as uniformly spread layers (see part 6.3.2).

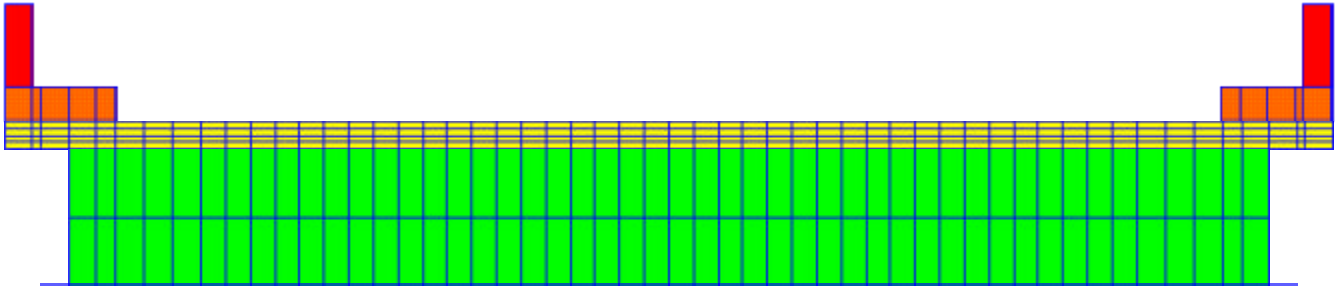


Figure 6.25 Cross-section of the bridge model

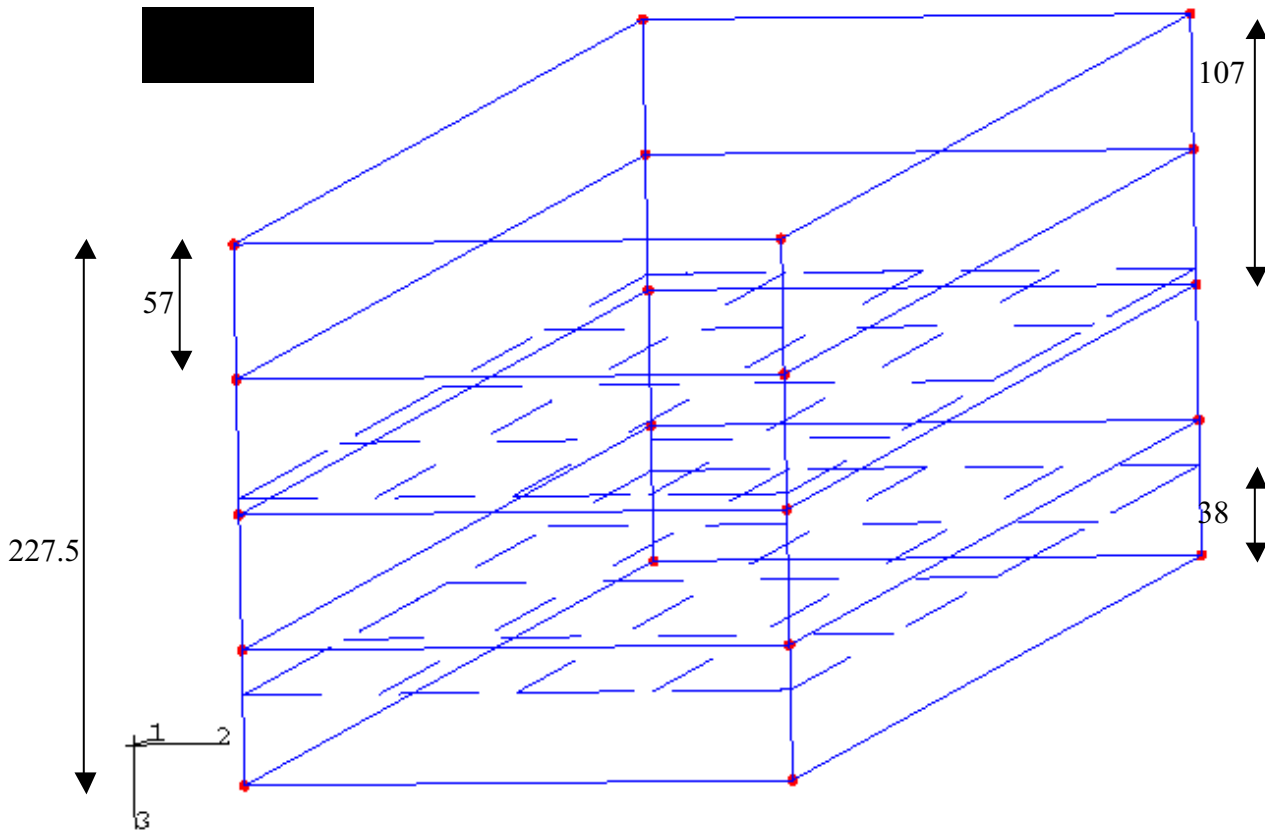


Figure 6.26 Layers of uniformly smeared reinforcement

The actual girders consist of bolted plates and angle beams. Girders in the model are represented by 4 node shell elements. The cross-section of each girder is divided into 6 elements as shown in Figure 6.4. The beam depth, width of flanges and web thickness in the model are the same as in the actual structure. The thickness of flange elements is determined in such a way that the moment of inertia is the same as in the actual girder.

Concrete diaphragms are discretized using a number of shell elements. As it is shown in Figure 6.25, two layers of elements are used with the transverse division identical to that in the slab. The following material data was applied for reinforcement and girders:

$$f_{YR} = 276 \text{ MPa (40 ksi) for rebars,}$$

$$f_{YG} = 248 \text{ MPa (36 ksi) for girders.}$$

The concrete parameters were estimated during the field test (see part 6.3.2):

$$E_c = 19.7 \text{ GPa}$$

$$\nu_c = 0.18,$$

$$f_{c1}' = 0.4 * f_{c2}' = 15.35 \text{ MPa,}$$

$$f_{c2}' = 38.37 \text{ MPa,}$$

$$\varepsilon_{Yc2} = 0.6\%.$$

6.4 Calibration of the FE model

Calibration refers to the determination of unknown model parameters, based on the comparison of calculated values and the available test data. Parameters which influence

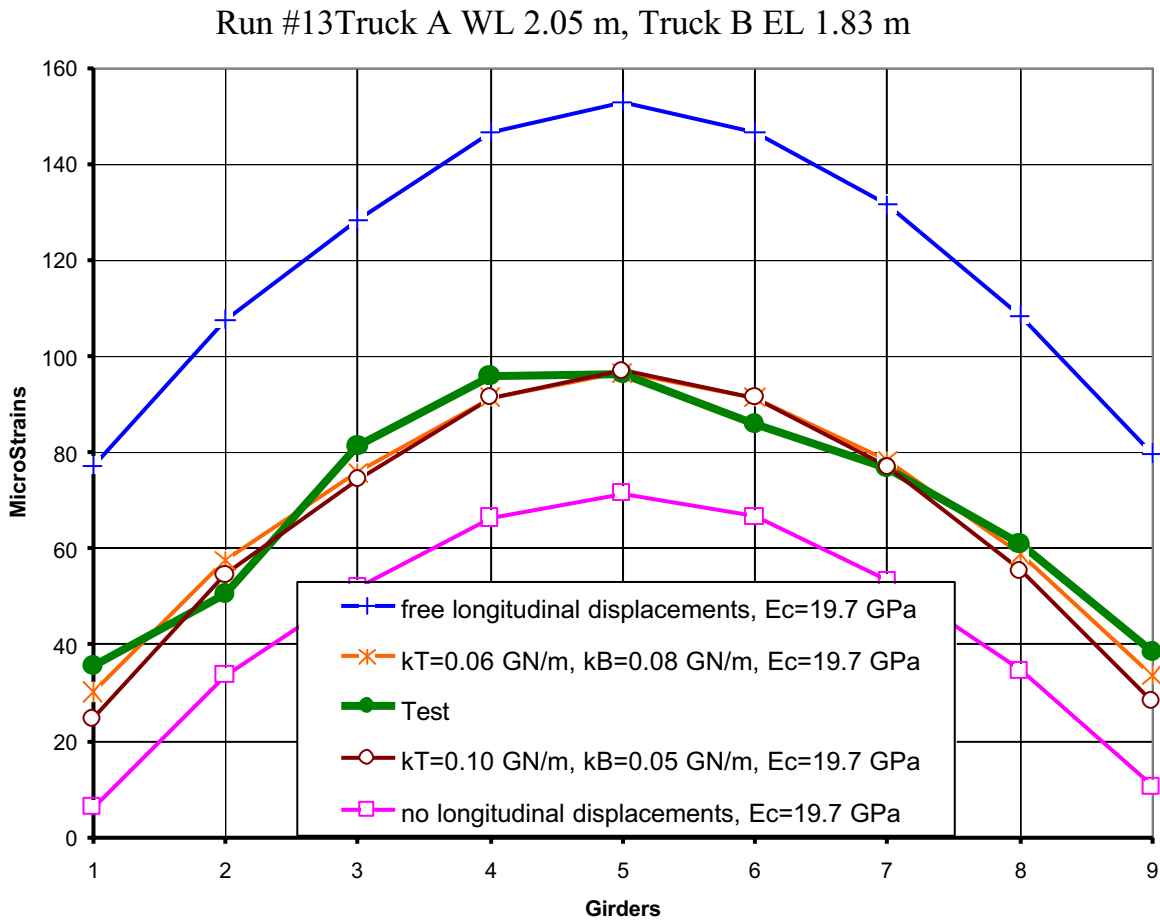


Figure 6.27 Strains in girders for different boundary conditions.

calculated structural and material values, are discussed in the part 6.3.1. The most difficult of this is the assessment of boundary conditions. Corrosion of the bearings causes significant changes in the support condition.

In Figure 6.27, calculated microstrains for the bottom flanges of a girder at midspan are presented. They are compared with test results. This comparison is made for the maximum live load used during the test. This consists of two trucks, each placed in the center of traffic

lanes. The upper curve represents the calculated values for a simple support with free longitudinal displacement at one end. This is the support condition usually assumed by designers. Comparison with test results shows that for such boundary conditions, we receive much bigger values than the actual strains. In the case where longitudinal displacement (in bottom flanges) is completely constrained, calculated strains are presented in Figure 6.27 by the bottom curve. This means that boundary conditions of the actual bridge are somewhere between the simple support (with free longitudinal displacement) and the case where both girder ends are longitudinally fixed. To model such conditions special spring elements available in ABAQUS are used. The linear spring element is described by the value of the stiffness k , direction x_i , and the label of the node to which the spring is attached. Given by the user, spring stiffness defines the relation between the displacement u_i of the node i , in the direction x_i and the reaction in the spring

$$R_i = k * u_i . \tag{6-4}$$

Additional springs applied to the top flanges are used to simulate the elastic constraints for rotations. After many runs it was discovered that the following three unknown parameters have the influence on the stiffness of the modeled superstructure

k_T – stiffness of the top springs,

k_B – stiffness of the bottom springs,

E_c – modulus of elasticity for the concrete slab.

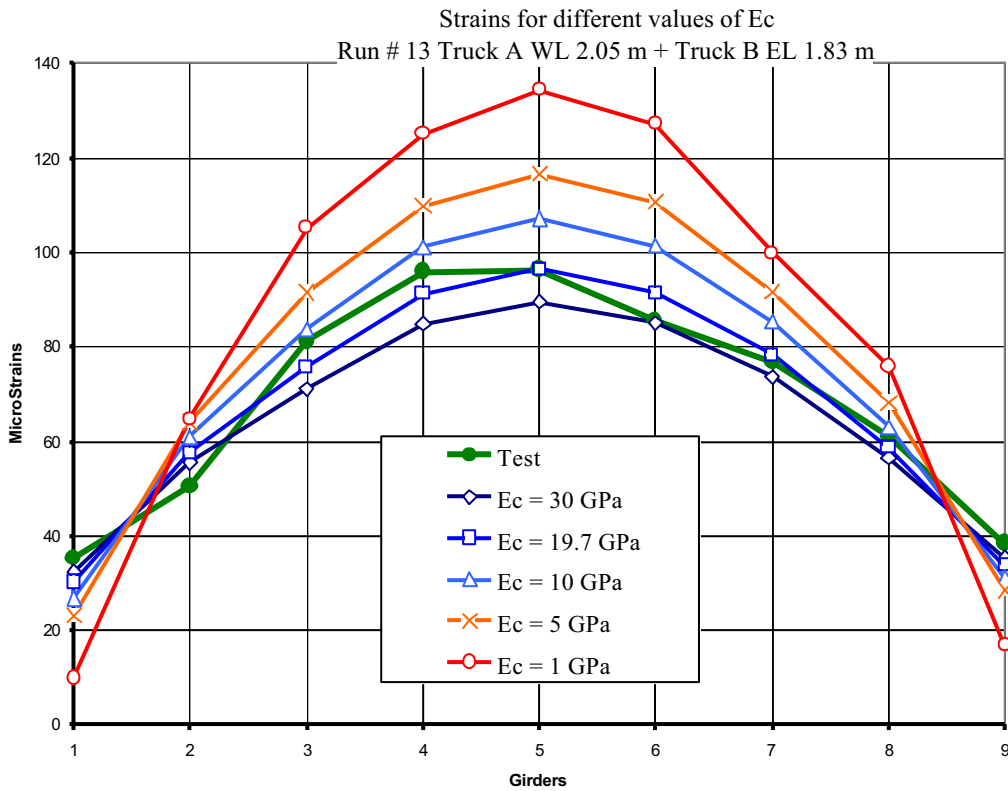


Figure 6.28 Strains for different values of E_c .

These three values influence the magnitude of strains at the midspan, where strains were measured during the test. In each case this influence is different. This means that there should be only one optimum set of values for these parameters. For example, the stiffness of the top springs changes not only the magnitude of all strains but also the curvature of the girders. If the bottom spring constants are also changed, it can lead to different values of maximum deflections with the same strains. Modulus of elasticity for concrete changes the “shape” of the strain curve presented in Figure 6.28. The stiffness of springs: $k_T=0.06$ GN/m and $k_B=0.08$ GN/m (see Figure 6.27) was used to calculate strains in Figure 6.28. Values for $E_c = 19.7$ GPa taken from field test gives the best fit to strains. The value used in the model for E_c represents the real material properties with cracking taken into account.

To estimate the optimum magnitude of unknown parameters, more test data is needed. For example, at least one girder should be instrumented with transducers placed along its length on both bottom and top flanges. Transducers on top flanges can help to

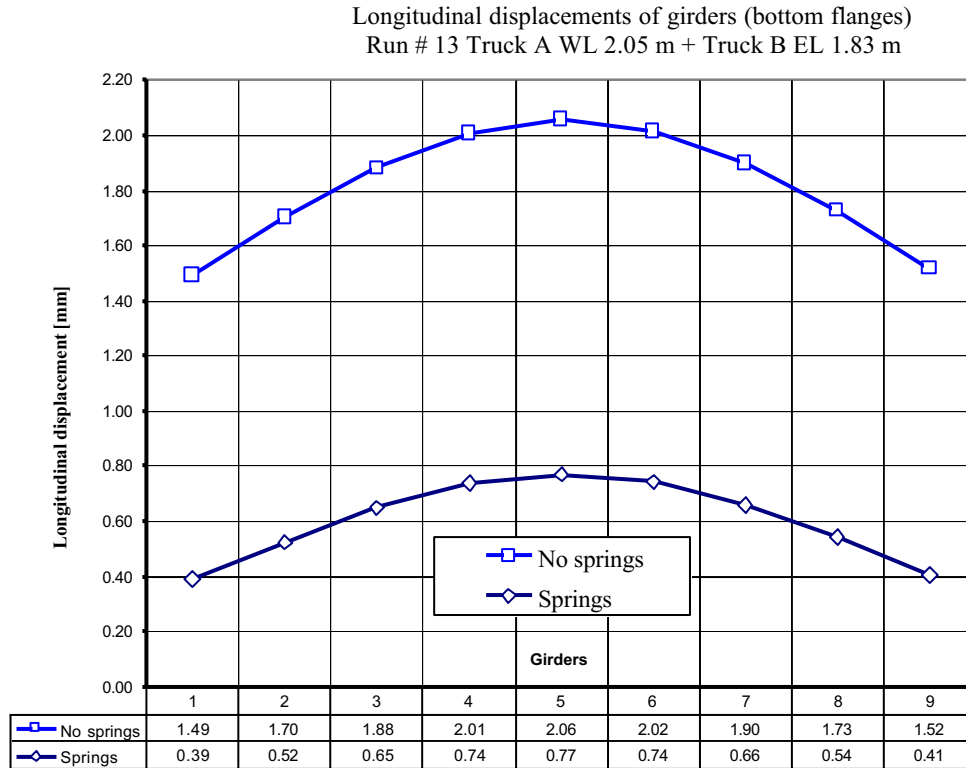


Figure 6.29 Longitudinal girder displacements

determine whether there is composite or noncomposite action Schultz et al. (1995). In the model described here, fully composite action was assumed. It is consistent with the way the slab - girder connection was constructed in the actual bridge. Figure 6.20 shows steel shear connectors welded to the top flanges.

Additional transducers placed along the bottom flange of the girder allow for the determination of curvature. As mentioned previously, the shape of a deflected girder is strictly influenced by the rotation constrains.

Based on the available test data the following optimum values were estimated

$$k_T = 0.06 \text{ GN/m} - \text{stiffness of the top springs}, \tag{6-5}$$

$$k_B = 0.08 \text{ GN/m} - \text{stiffness of the bottom springs}.$$

The value of $E_c = 19.7$ GPa used in the model was determined from a field test using the ultrasonic impulse method.

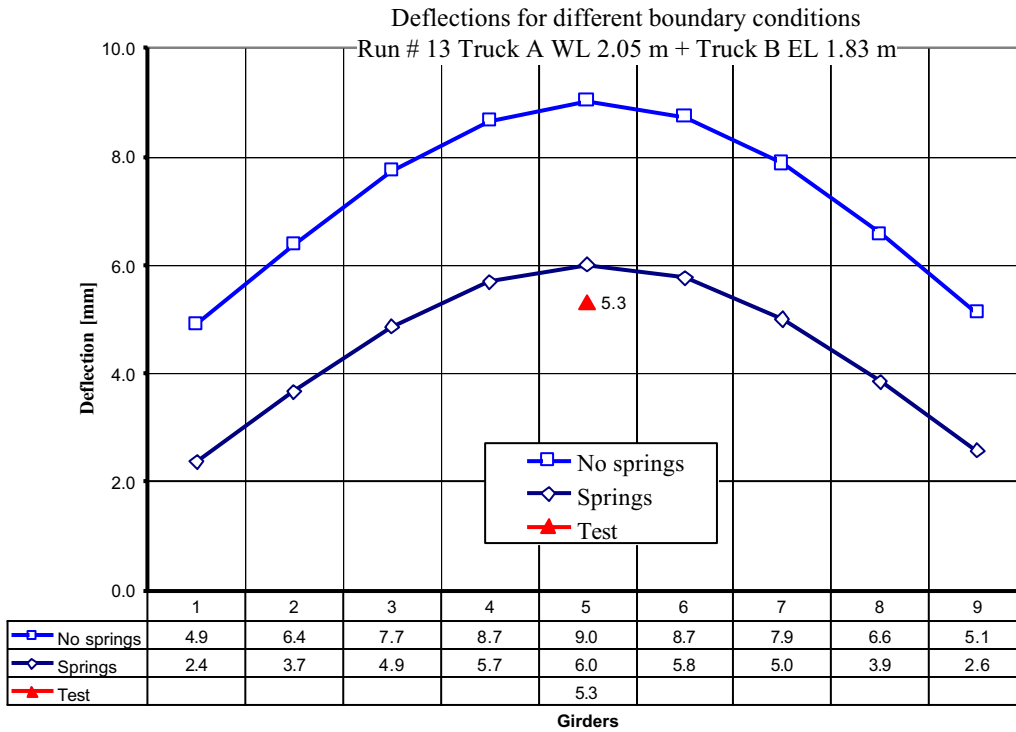


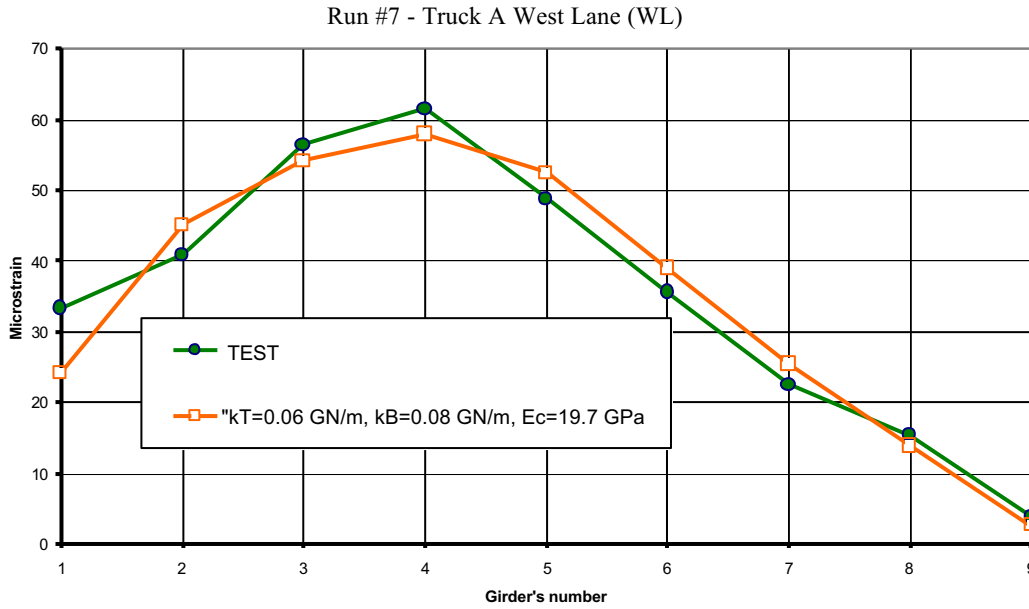
Figure 6.30 Deflections for different boundary conditions

The stiffness of springs is dependent on their number (number of nodes to which they are attached). These values should be treated as artificial parameters strictly connected to a model, not with an actual bridge. In the case where the test data is not available the following procedure should be used for spring stiffness estimation. First calculations for a simply supported model should be made. This allows determination of the magnitude of longitudinal displacements for nodes to which springs are to be attached. Then the evaluation of the actual displacements should be done, based on the engineering assessment of support conditions.

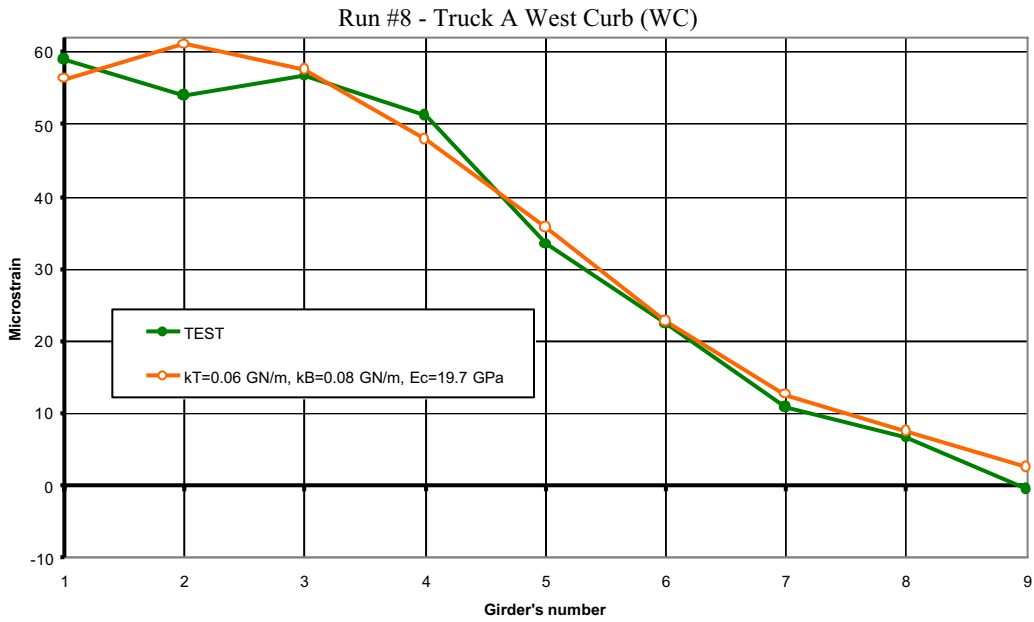
Figure 6.29 shows the longitudinal displacements at the girder supports with and without springs in the model. This can be seen that these displacements are reduced up to 37 % of the value without springs. Figure 6.30 shows vertical displacements in the midspan for

different boundary conditions. During the test, deflection of the fifth (middle) girder was measured using laser.

The correlation between test data and numerical results for different load configurations is presented in Figures 6.31 - 6.33. Because of the limitation of available test data, the presented correlation is recognized as the best possible.



Figures 6.31 Comparison of calculated and measured strains for run # 7



Figures 6.32 Comparison of calculated and measured strains for run # 8

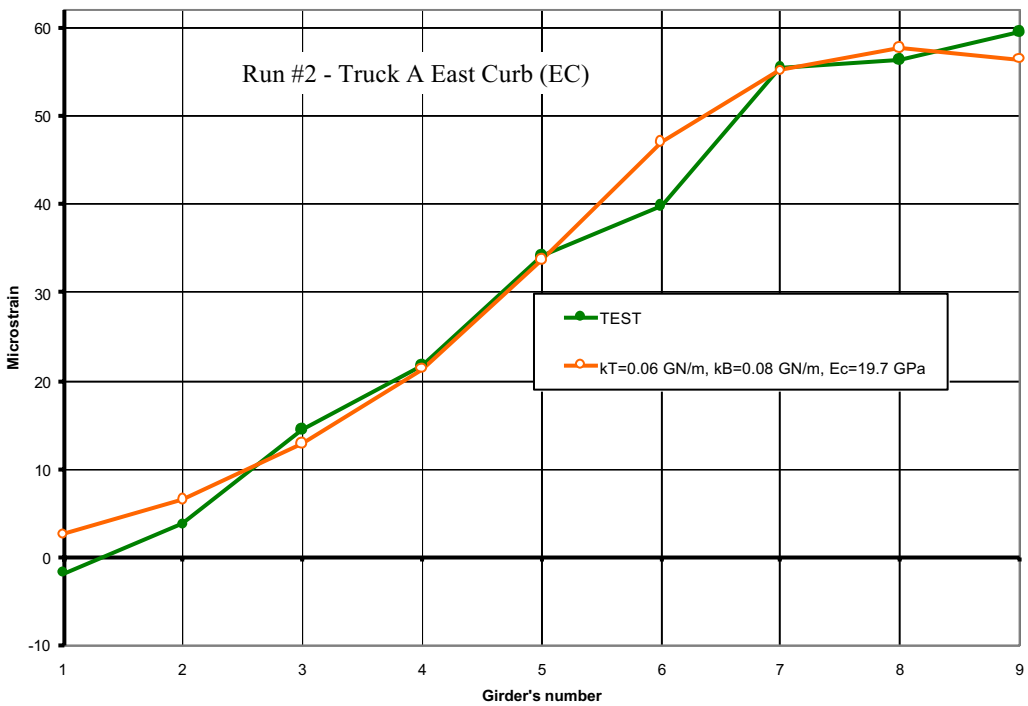


Figure 6.33 Comparison of calculated and measured strains for run # 2

6.5 Summary of analytical results

6.5.1 Parametric study

The structural behavior of highway bridges, especially slab on girder bridges can change during the years of service. It is mainly due to quantity changes of material properties for concrete deck slabs. The main reason of that is extensive cracking and delamination. Deterioration of concrete affects its modulus of elasticity, which according to BS 5400 Code of Practice (1990) can be reduced even by half.

This part focuses on the relation between changes of modulus of elasticity for concrete and the behavior of the bridge superstructure. Two examples are tested. In the first example,

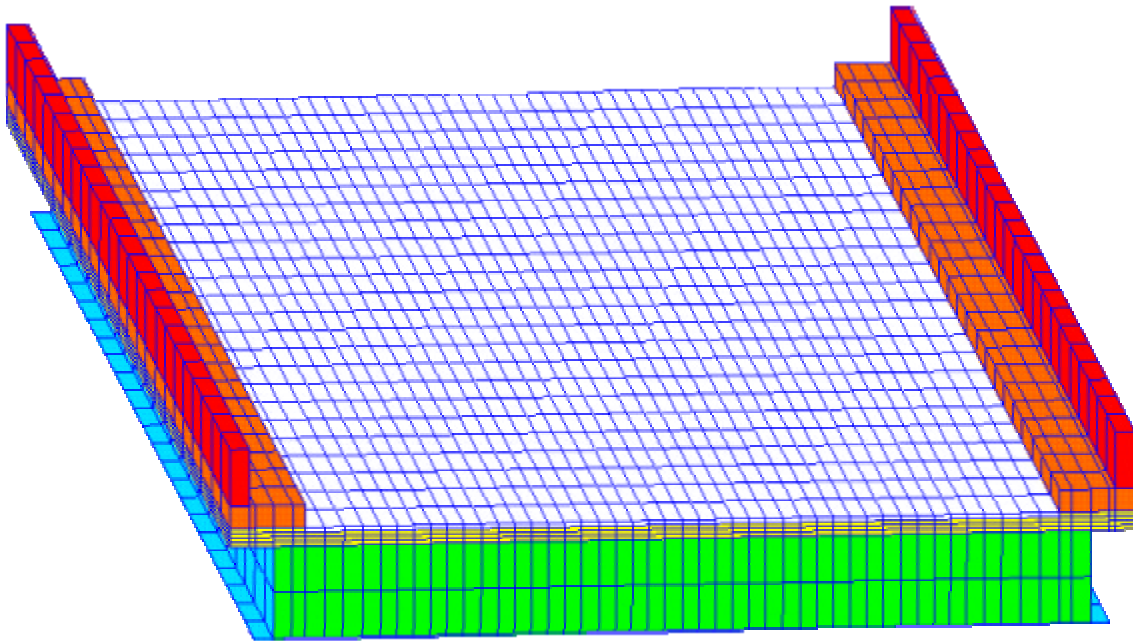


Figure 6.34 FE model with top layer deteriorated $E_c \approx 0$ GPa

only the top layer of the deck was deteriorated due to the delamination or extensive cracking caused by freezing and thawing. It was assumed that up to one fourth of the slab thickness was completely deteriorated and E_c for this part of the deck was reduced to practically a

value of zero Figure 6.34. In Figure 6.35 calculated values of strains for this case are compared with data from test measurements. The case when a live load consisted of two trucks placed in the center of traffic lanes is concerned. It can be seen that the change in structural stiffness is small. In Figure 6.36 the comparison is made for dead load (gravity) and the same live load taken together.

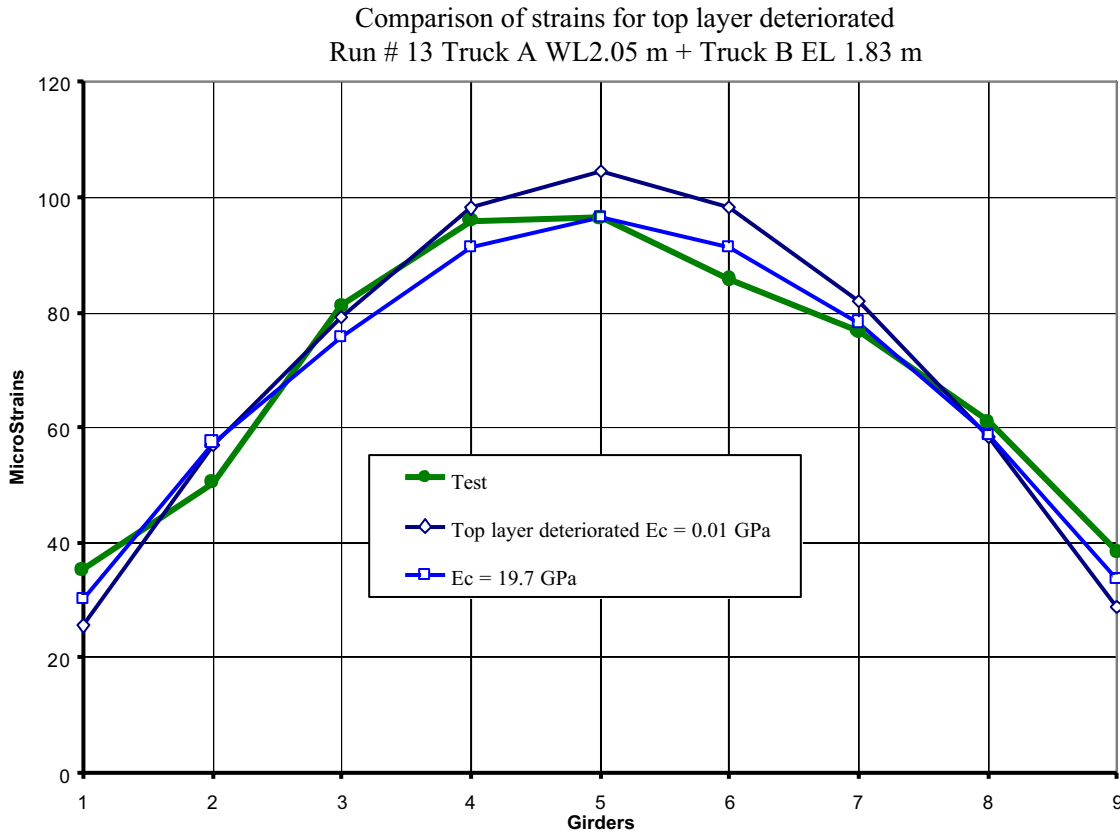


Figure 6.35 The influence of the deterioration of top deck layer on strains caused by live loads.

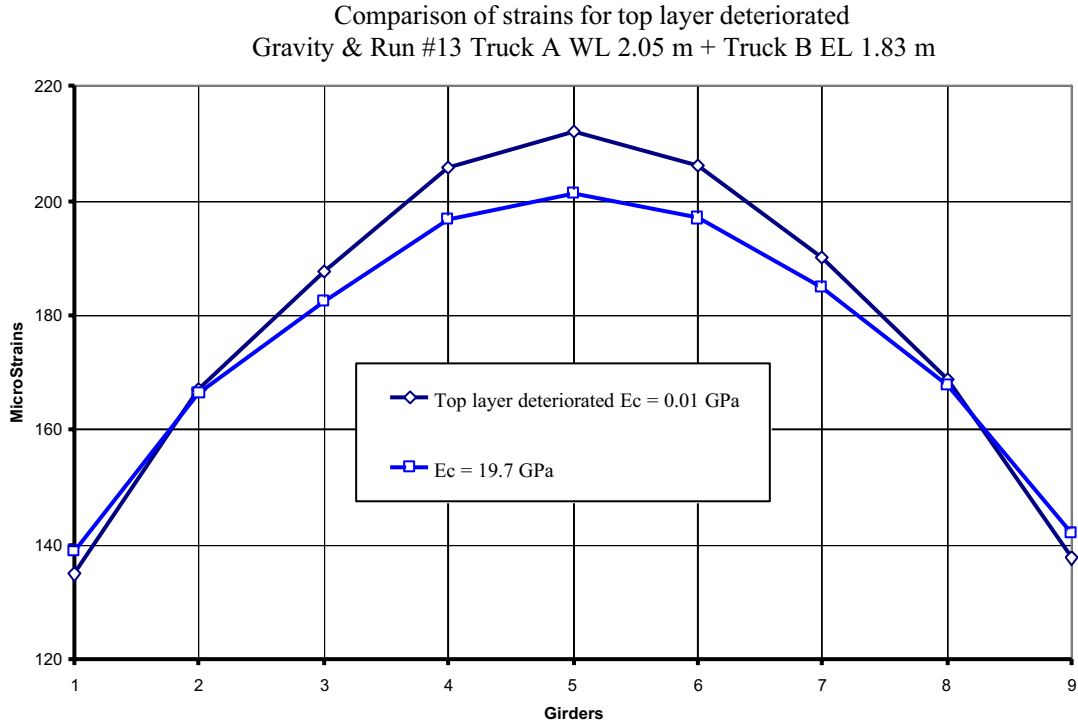


Figure 6.36 The influence of the deterioration of top deck layer on strains caused by dead and live load.

The next case investigated here was when modulus of elasticity for concrete in the entire deck slab changes its value gradually. Figure 6.37 shows strains in girders caused by live load only and for changing magnitude of E_c . The reduction of value $E_c = 19.7$ GPa (estimated for actual bridge) to only 1.0 GPa causes increase of maximum strain in the middle girder from 96.5 to 134.4 microstrains. This means that the reduction of E_c by 20 times gives only 39% increase of girder strain.

Strains for different values of E_c
Run # 13 Truck A WL 2.05 m + Truck B EL 1.83 m

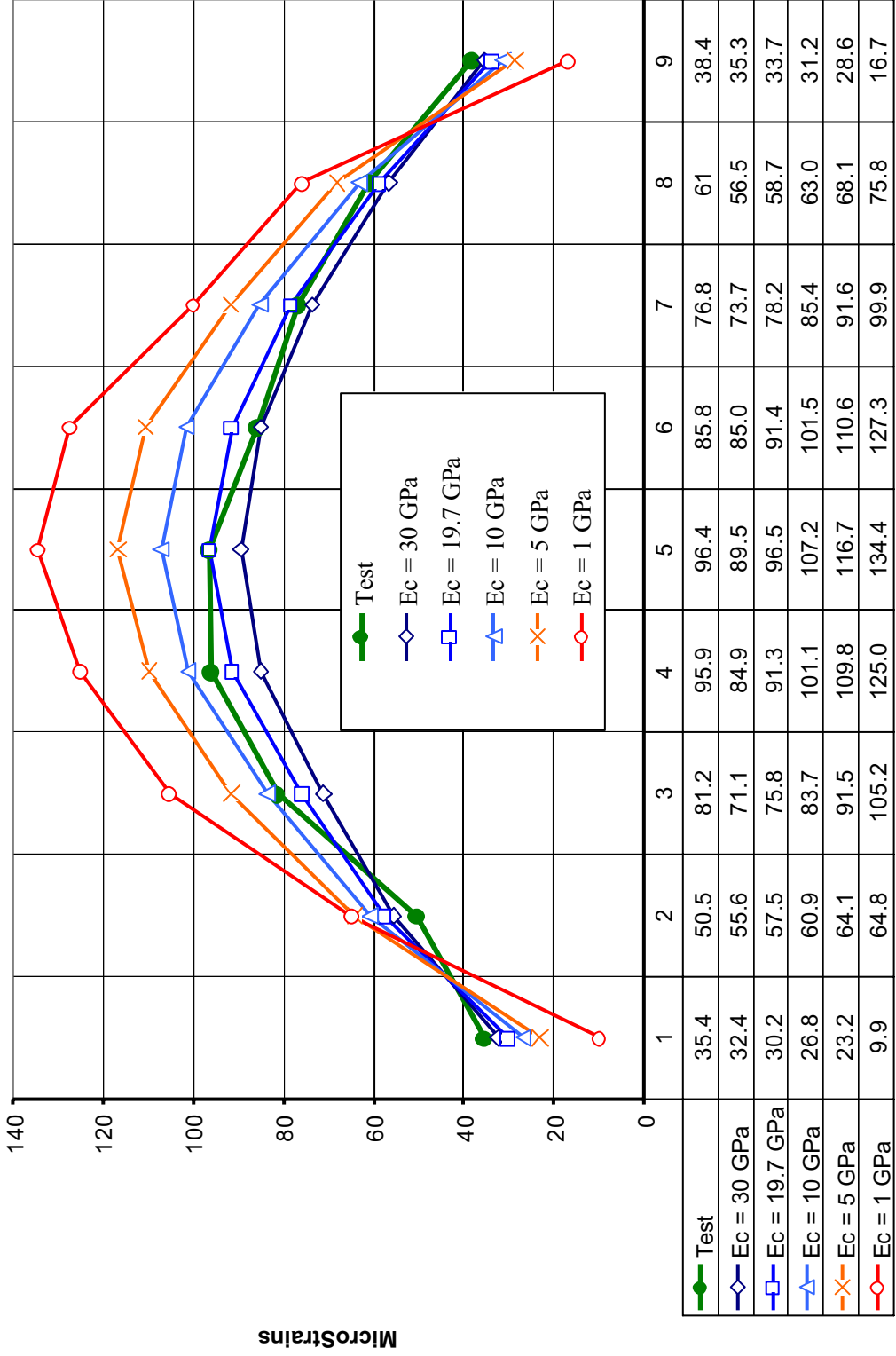


Figure 6.37 Girder strains caused by live load for different values of E_c .

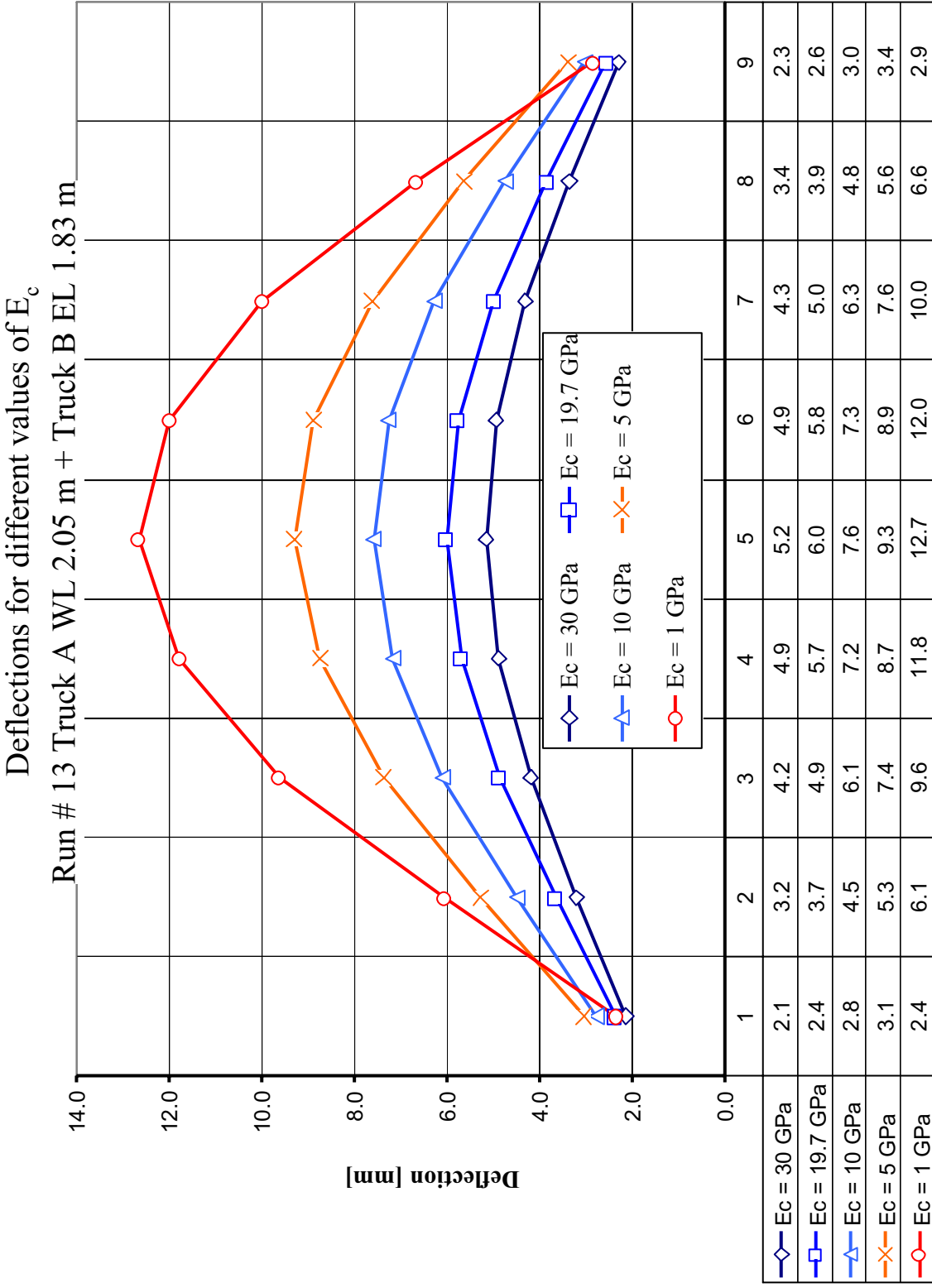


Figure 6.38 Deflections for live loads with different values of E_c .

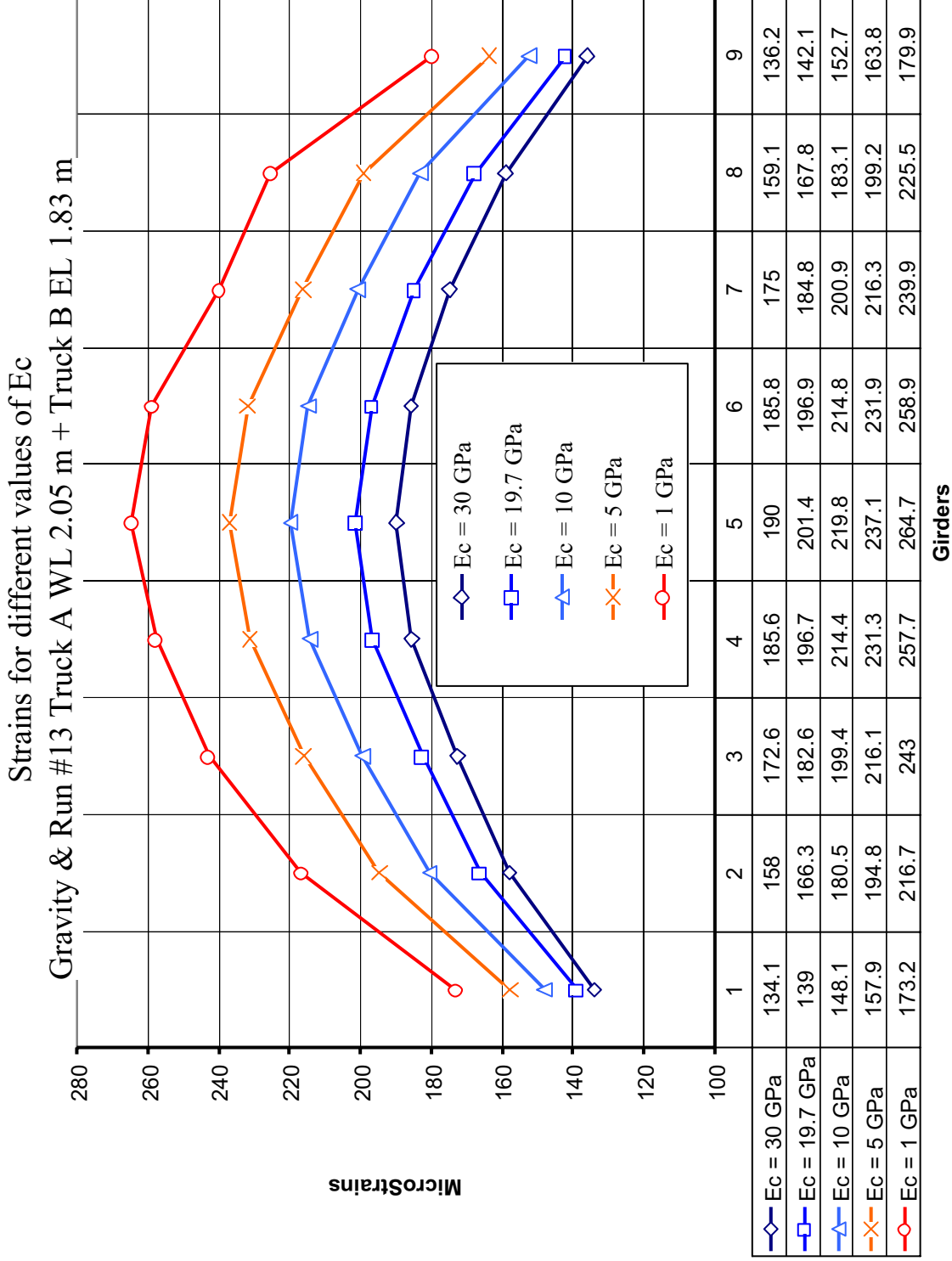


Figure 6.39 Strains of gravity and live loads with different E_c values.

Deflections for different values of E_c
Gravity & Run #13 Truck A WL 2.05 m + Truck B EL 1.83 m

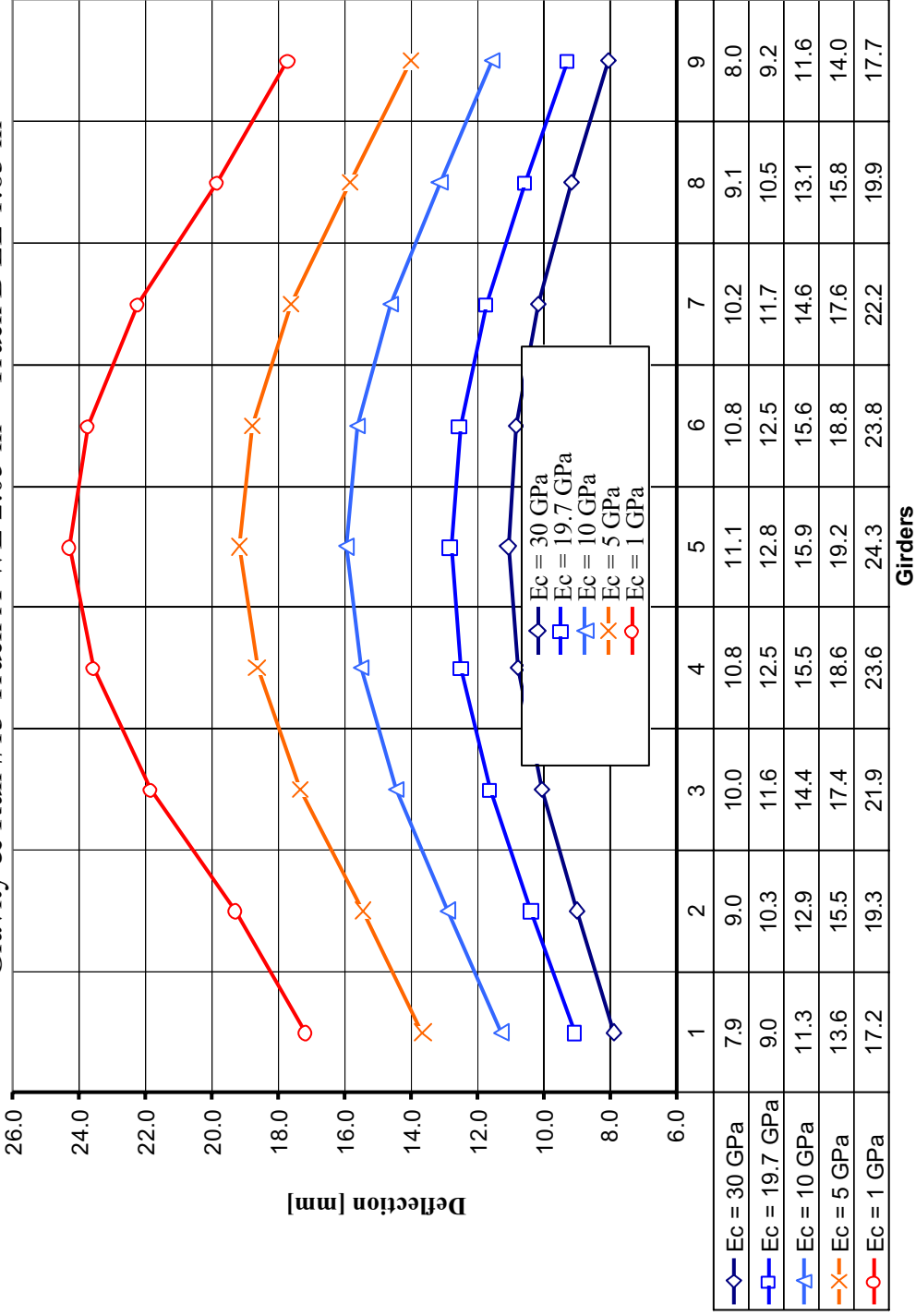


Figure 6.40 Deflections of gravity and live loads with different E_c values.

In Figure 6.38 the comparison is made for deflections in the midspan. The maximum growth of deflections is 112 %.

To estimate the drop in the stiffness of the actual bridge weight (gravity) and live loads are taken into account. In Figure 6.39 strains for changing E_c are presented. Even for reduction of E_c down to the hypothetical value of 1 GPa, maximum strain in girder equals 265.7 microstrains is much smaller than yielding strain

$$\varepsilon_{pl} = \frac{f_y}{E_c} = \frac{248}{200000} \times 10^6 = 1240 \text{ microstrains} \quad (6-6)$$

Figure 6.40 shows deflections for the same load configuration (gravity and live load). Maximum deflection for live loads and $E_c = 1 \text{ GPa}$ $u_3 = 12.7 \text{ mm}$ (Figure 6.38) is still smaller than ultimate deflection

$$u_3^{\max} = 12.7 \text{ mm} < \frac{L}{800} = \frac{22,420}{800} = 28 \text{ mm}. \quad (6-7)$$

Presented calculated results show that E_c magnitude has small influence on the structural stiffness. Global structural behavior of the bridge is mostly connected with girder properties. The main role of the concrete slab is to transmit loading to steel girders. The influence of E_c on local behavior of concrete deck slab is not investigated here. This is difficult to include the effect of cracks in a detailed investigation of the local deck behavior.

6.5.2 Final results for dead and live loads

In this part calculated deformations, strains and stresses for dead and live loads are presented. All results are received for the calibrated model described in part 6.4.

Deformations of the bridge components

Figures 6.41-6.46 show deformations of different bridge components. In postprocessing there is ability to extract any set of elements and present results only for them. Of course calculations are made for the whole model consisting of all the components described in part 6.3.5. Calculations for dead and live loads are made in two steps. In the first step only gravity is taken into account. In the next step additionally live load is applied. Final results are for dead and live loads taken together.

Figures 6.41 and 6.42 show top and bottom views of deformed bridge. Because deflections are very small increased magnification factor is used.

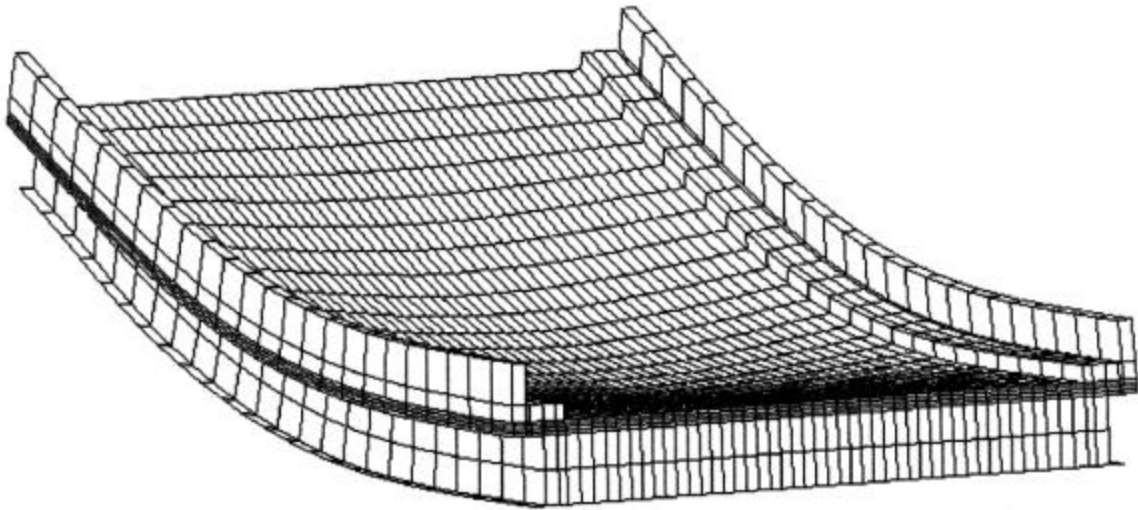


Figure 6.41 Top view of the deformed bridge.

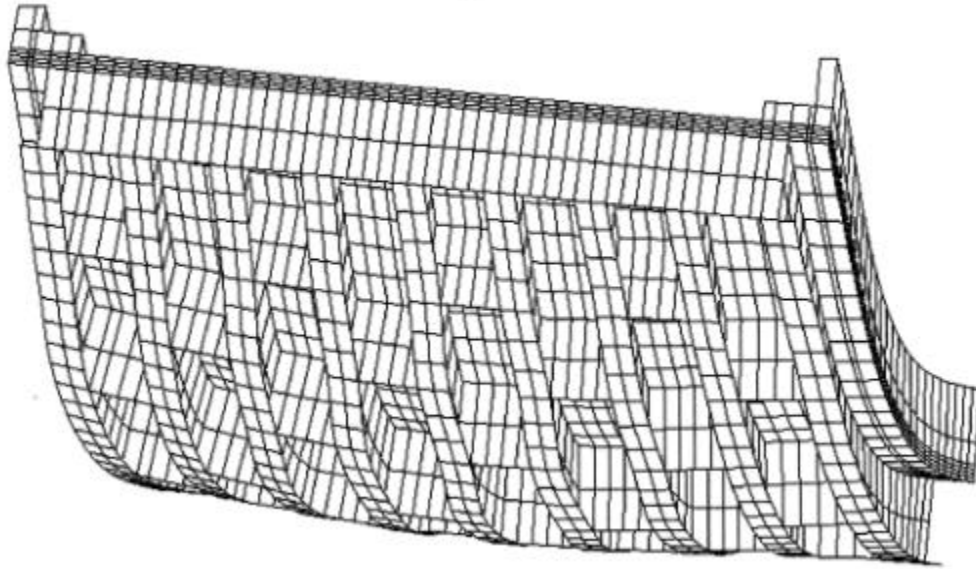


Figure 6.42 Bottom view of the deformed bridge.

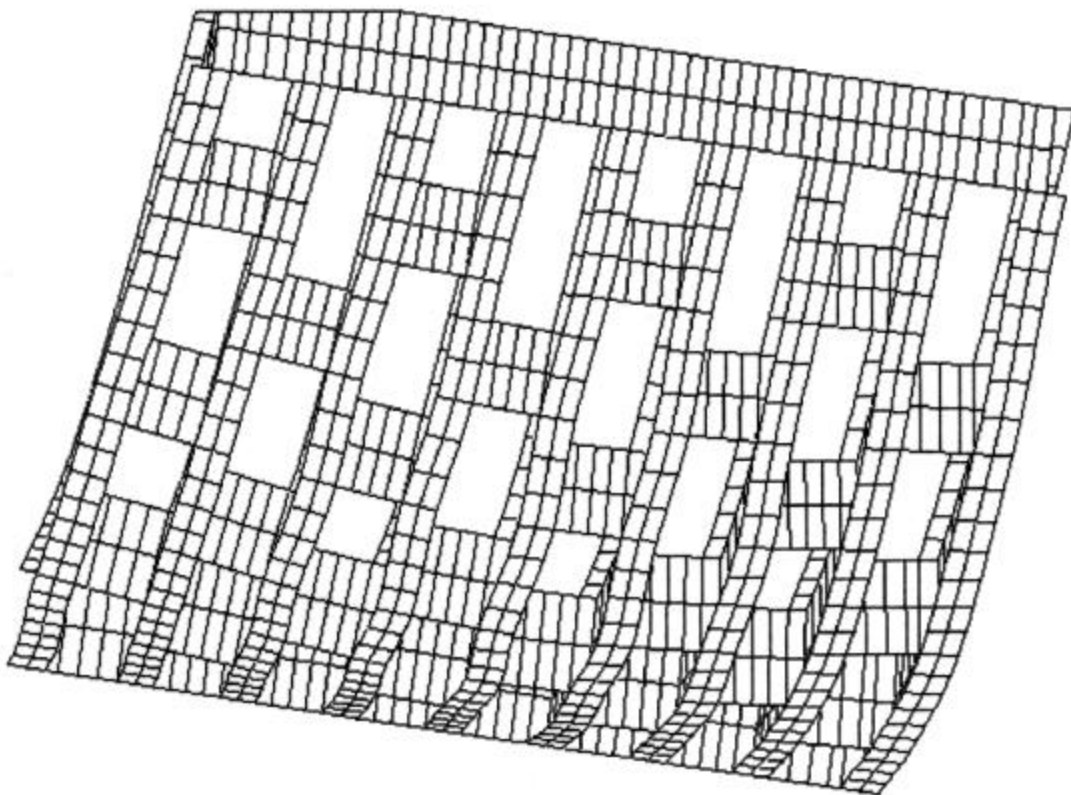


Figure 6.43 Deformed girders and diaphragms.

In Figure 6.43 only girders and diaphragms are presented. Figures 6.44-6.46 show deflected slab for 3 different load configurations: gravity, live load as in run # 13 (see Table 6.1) and both.

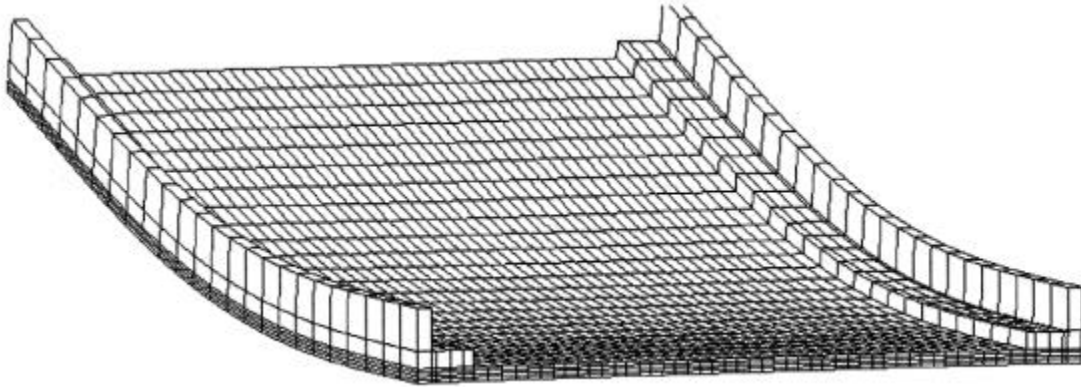
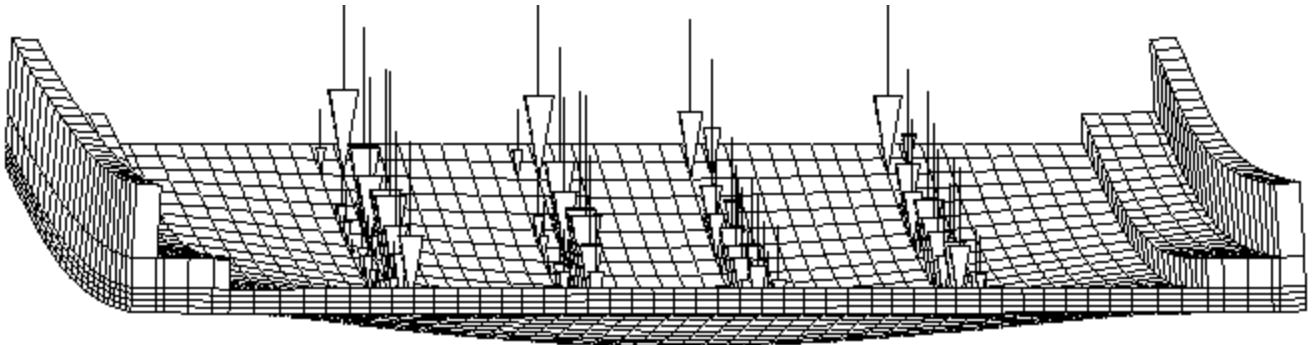


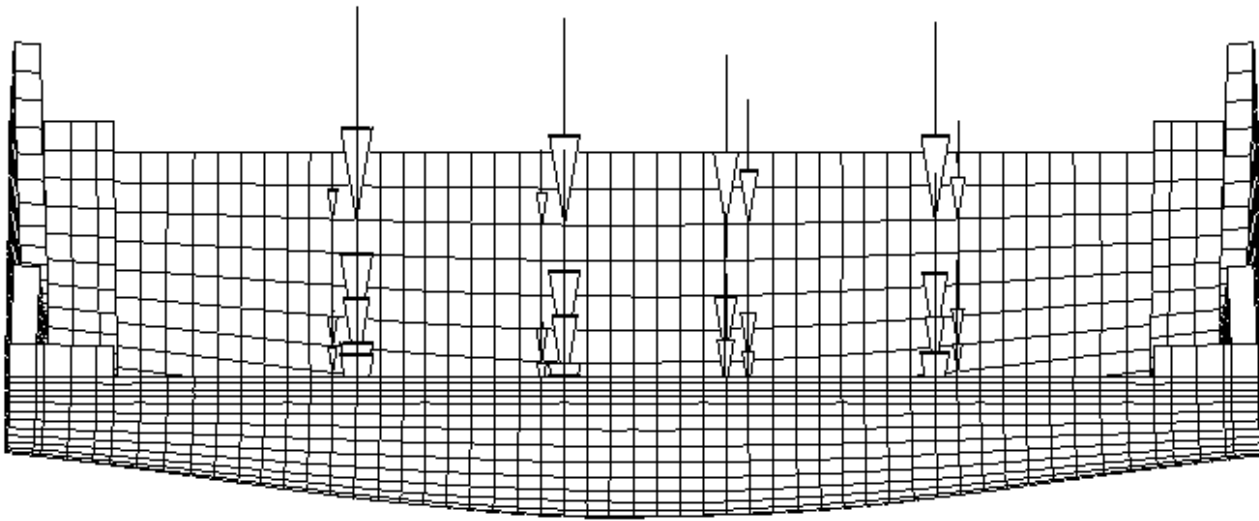
Figure 6.44 Deformed deck slab for dead load.



DISPLACEMENT MAGNIFICATION FACTOR = 150.
 RESTART FILE = TWJE4L20GPa STEP 1 INCREMENT 1
 TIME COMPLETED IN THIS STEP 1.00 TOTAL ACCUMULATED TIME 1.00
 ABAQUS VERSION: 5.8-1 DATE: 15-OCT-1999 TIME: 13:48:10

1 — 2
 |
 3

Figure 6.45 Deformed deck slab for live load – run #13.



DISPLACEMENT MAGNIFICATION FACTOR = 150.

RESTART FILE = G+TWJE4L20GPa STEP 2 INCREMENT 1

TIME COMPLETED IN THIS STEP 1.00 TOTAL ACCUMULATED TIME 2.00

ABAQUS VERSION: 5.8-1 DATE: 20-OCT-1999 TIME: 11:27:28

1
2
3

Figure 6.46 Deformed deck slab for dead and live loads.

Strains in the slab

In Figures 6.47-6.56 contours of longitudinal and transversal strains are presented. All contours here are plotted for the slab only. Figures 6.47-6.48 show strains for dead load. In Figures 6.49-6.54 different configurations of live loads described in Table 6.1 are taken into account. Figures 6.55-6.56 present strain contours for dead and live loads together. In Table 6.3 maximum values of calculated compression and tension strains in the slab are included.

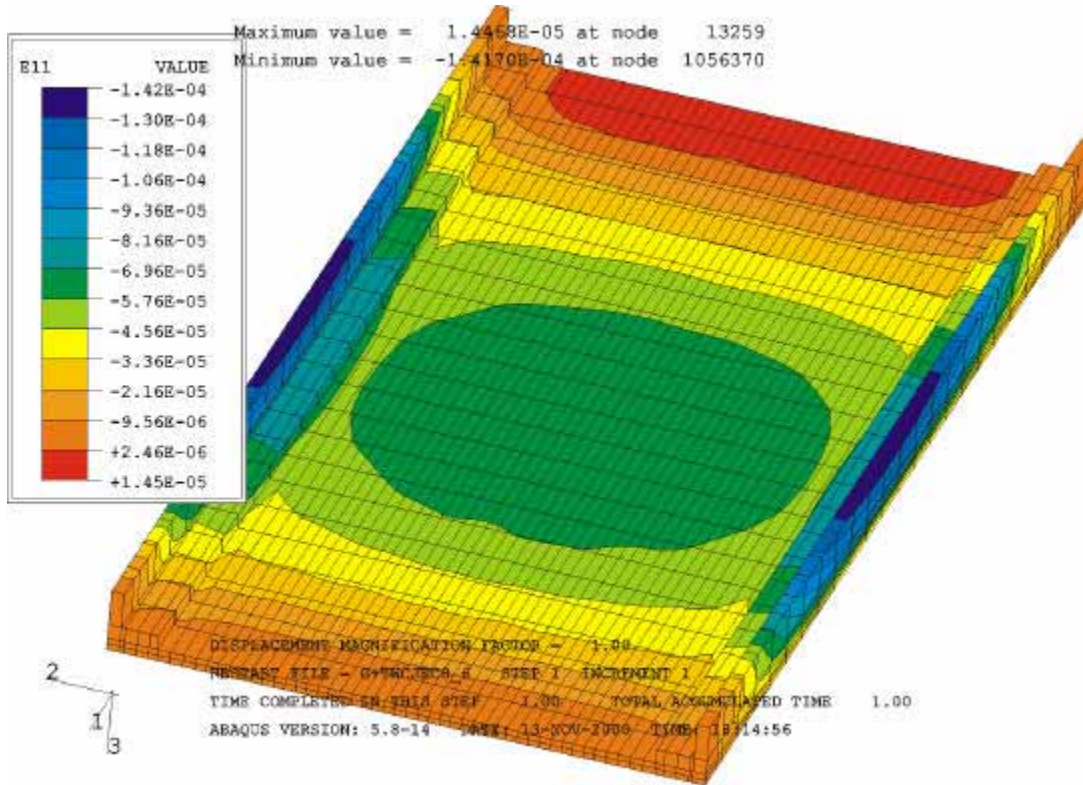


Figure 6.47 Contours of longitudinal strain for dead loads.

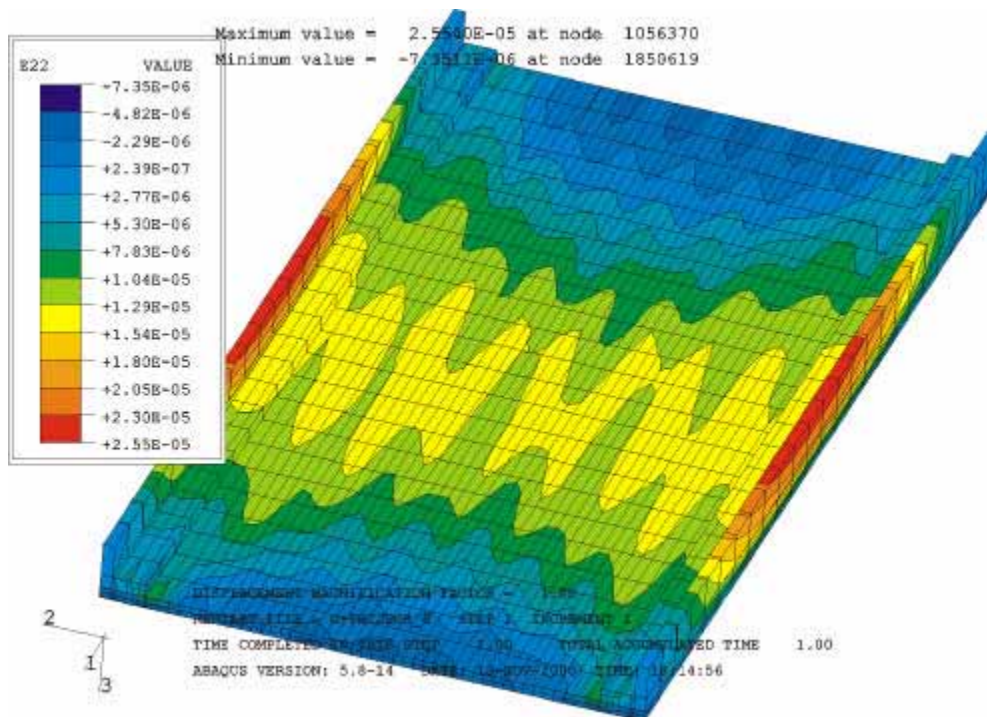


Figure 6.48 Contours of transverse strain for dead loads.

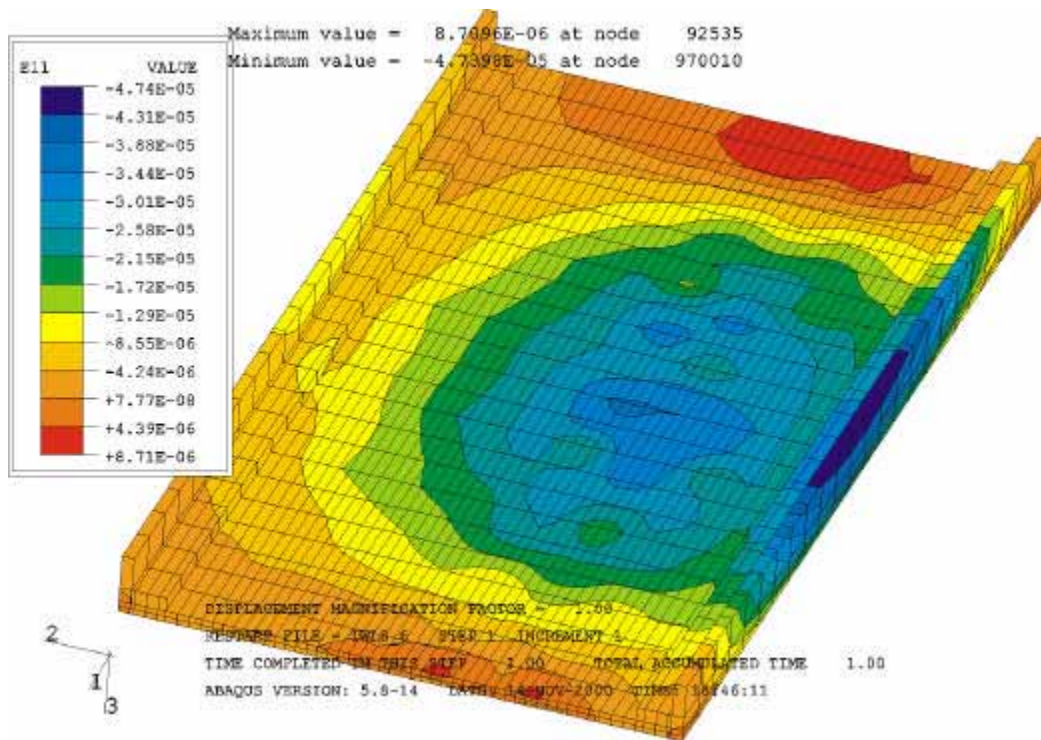


Figure 6.49 Contours of longitudinal strain for live load, run #7 – truck A, center of lane.

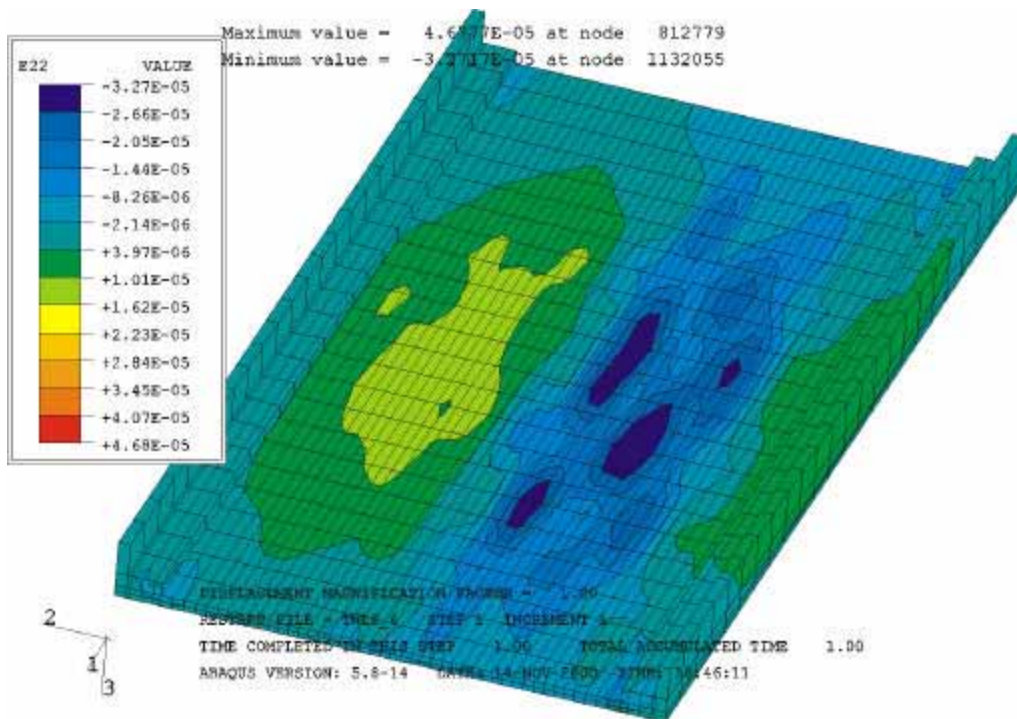


Figure 6.50 Contours of transverse strain for live load, run #7 – truck A, center of lane.

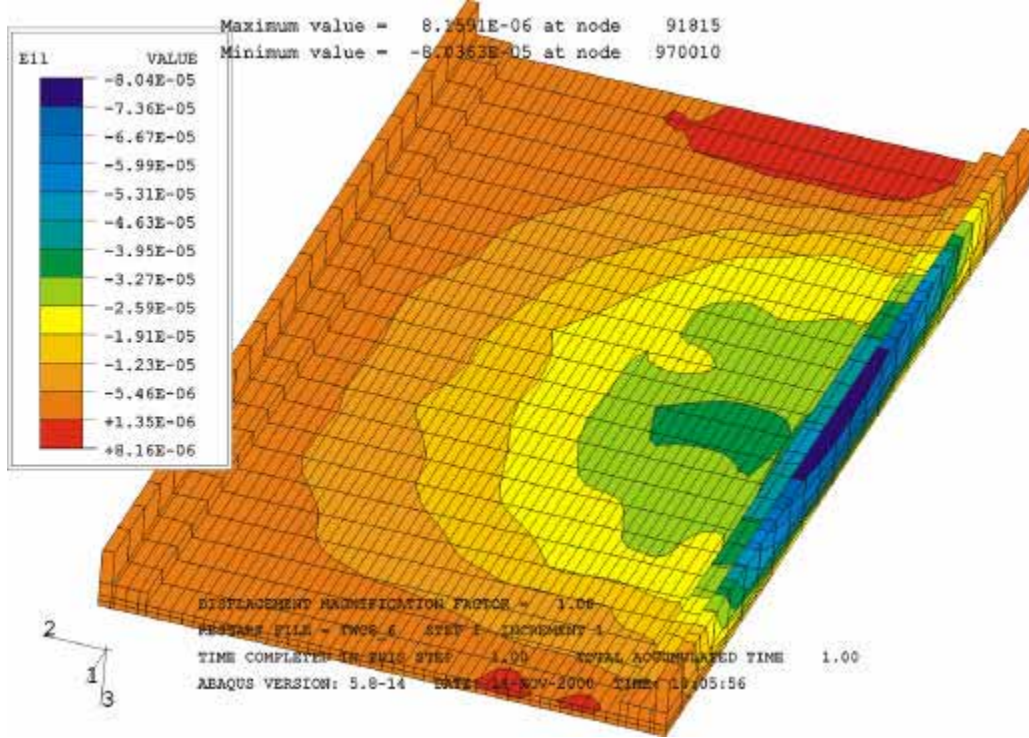


Figure 6.51 Contours of longitudinal strain for live load, run #8 – truck A, close to curb.

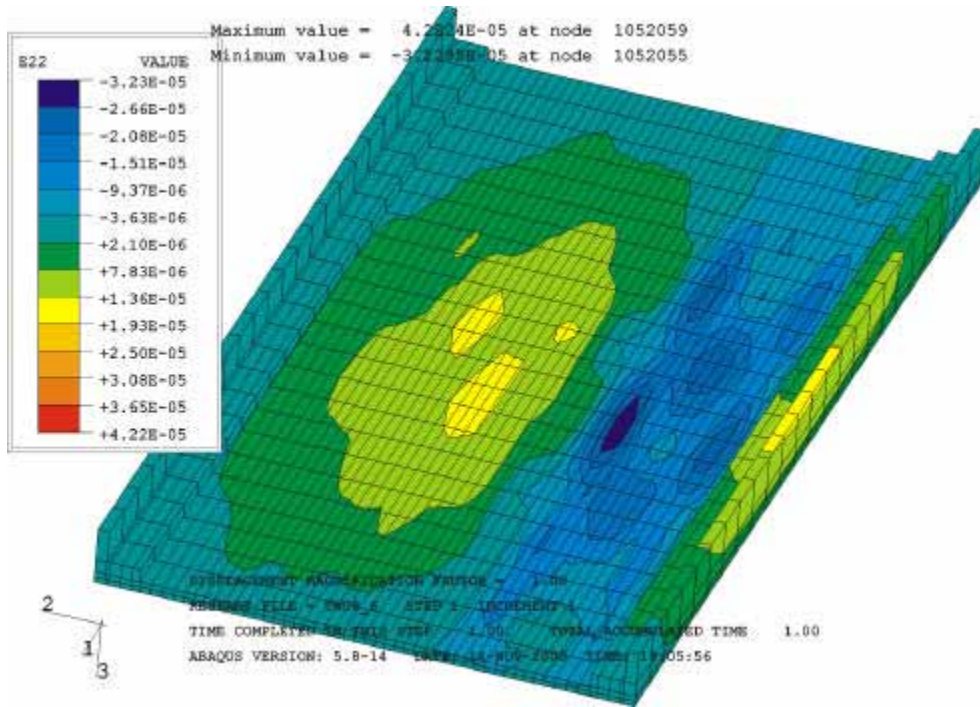


Figure 6.52 Contours of transverse strain for live load, run #8 – truck A, close to curb.

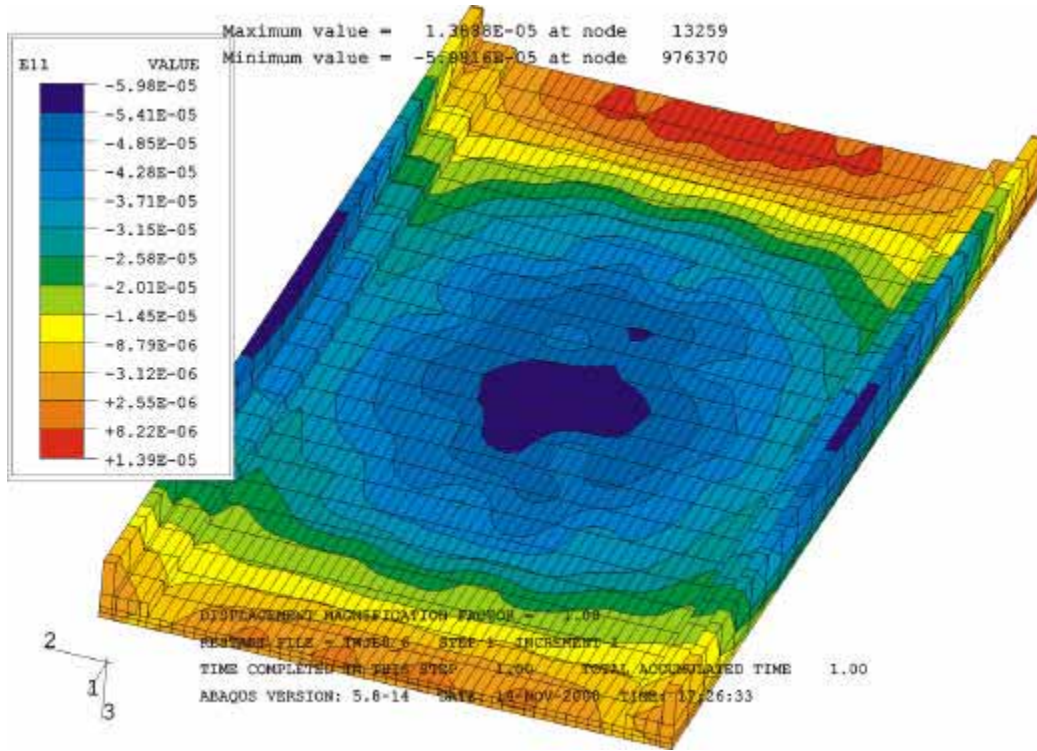


Figure 6.53 Contours of longitudinal strain for live load, run #13 – truck A and B, center of lanes.

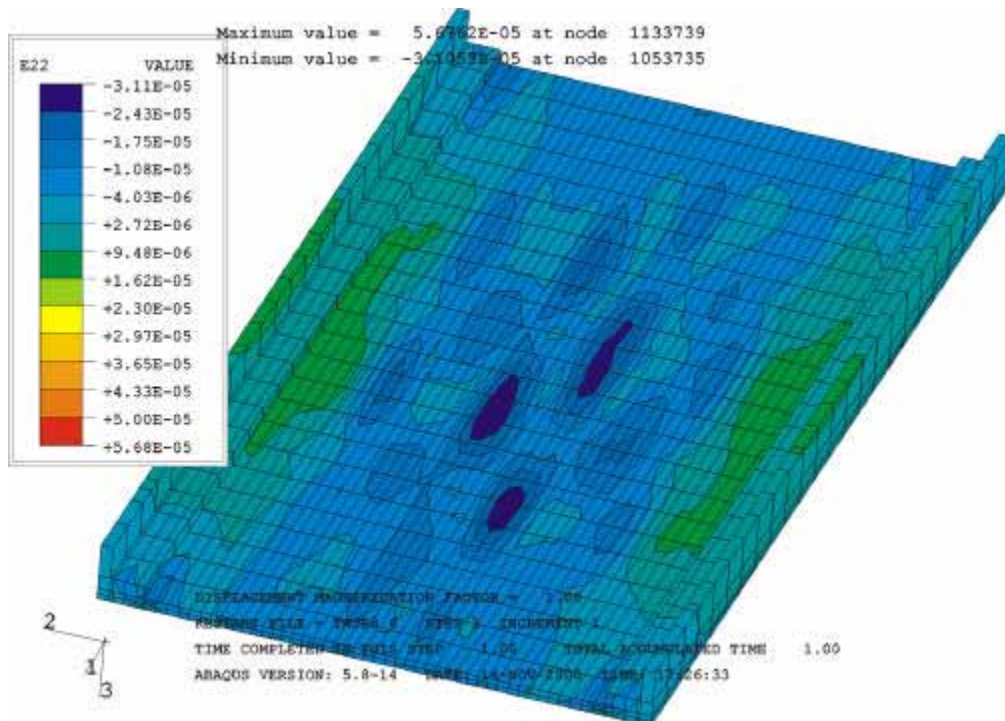


Figure 6.54 Contours of transverse strain for live load, run #13 – truck A and B, center of lanes.

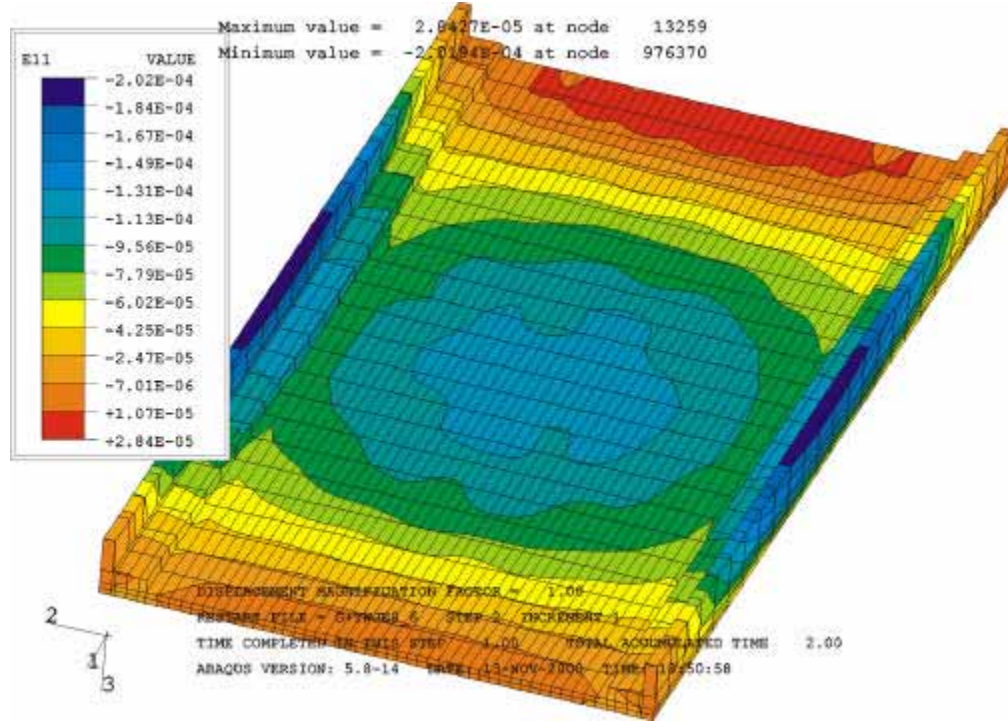


Figure 6.55 Contours of longitudinal strain for dead and live loads – gravity and run #13.

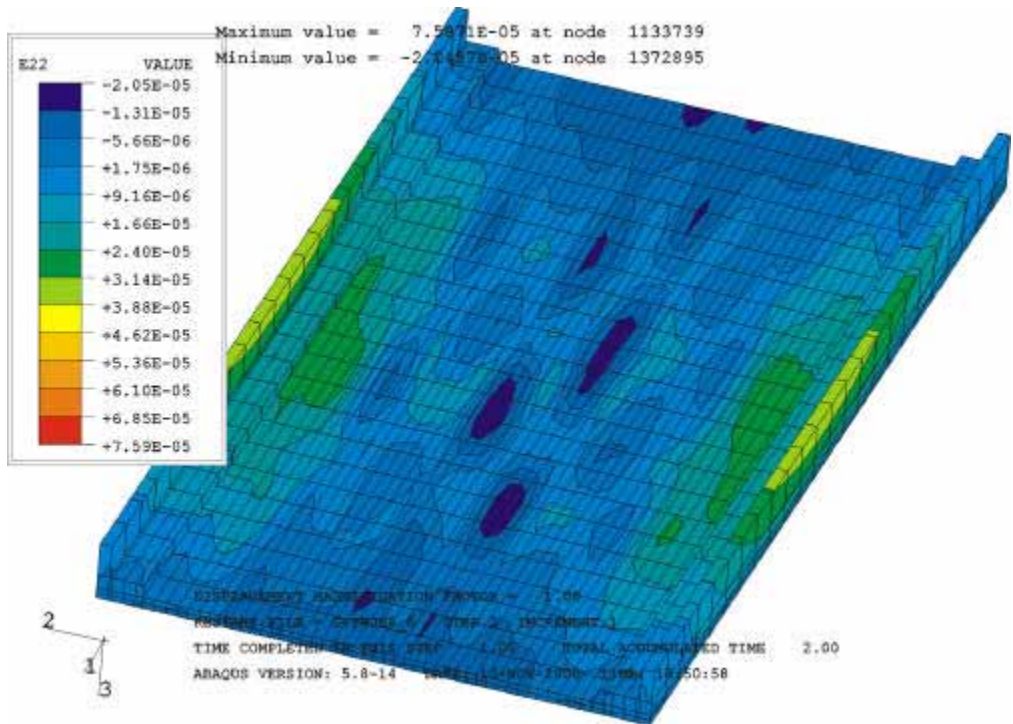


Figure 6.56 Contours of transverse strain for dead and live loads – gravity and run #13.

Table 6.3 Extreme strains in the slab for different load configuration.

#	Load configuration	Range of longitudinal microstrains in the slab	Range of transverse microstrains in the slab
1	Dead load	-142 - +14.5	-73.5 - +25.5
2	Live Load – run # 7, Truck A center of lane	-47.4 - +87.1	-32.7 - +46.8
3	Live Load – run # 8, Truck A close to curb	-80.4 - +81.6	-32.3 - +42.2
4	Live Load – run # 13, Truck A and B center of lanes	-59.8 - +13.9	-31.1 - +56.8
5	Dead and Live Loads Gravity and run # 13	-202 - +28.4	-20.5 - +75.9

(+) indicates tension, (-) indicates compression

Stress in the slab

Figures 6.57-6.66 show contours of longitudinal and transversal stresses on the top of the deck, for the same load configurations as previously. In Table 6.4 maximum values for calculated compression and tension stresses in the slab are presented. The values included in Table 6.4 show that the range of stresses in the slab is very low. The compression stresses are much lower than the assumed $f_{c1}' = 15.25$ MPa - absolute value of compressive stress defining the first stress-strain point of initial yielding (for zero plastic strain) Figure 6.7. This means that for all concerned load configurations the behavior of the superstructure is within linear elastic range. This was also proven by the test (see part 6.3.4). Calculated maximum tension stress in the transverse direction appears in the bottom surface of the slab (Figure 6.68).

Table 6.4 Maximum stresses in the slab for different load configuration

#	Load configuration	Range of longitudinal stress in the slab MPa	Range of transverse stress in the slab MPa
1	Dead load	-2.79 - +0.27	-0.17 - +0.21
2	Live Load – run # 7, Truck A center of lane	-0.93 - +0.15	-0.80 - +0.87
3	Live Load – run # 8, Truck A close to curb	-1.58 - +0.15	-0.78 - +0.78
4	Live Load – run # 13, Truck A and B center of lanes	-1.32 - +0.25	-0.85 - +1.01
5	Dead and Live Loads Gravity and run # 13	-3.98 - +0.52	-0.85 - +1.22

(+) indicates tension, (-) indicates compression

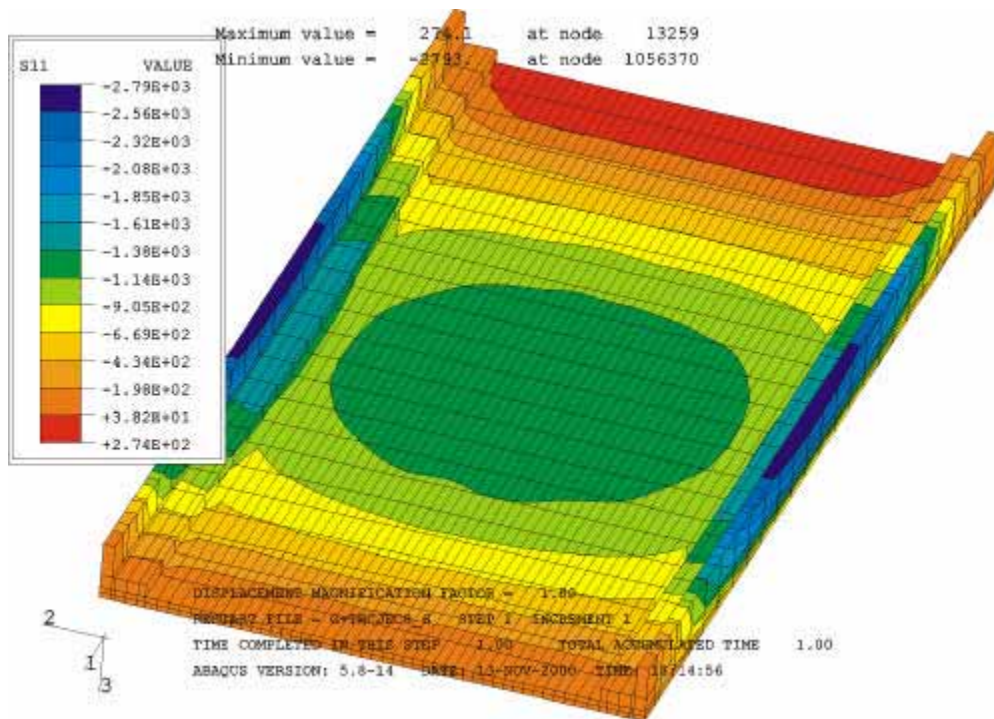


Figure 6.57 Contours of longitudinal stress for dead load – gravity. Top surface of deck

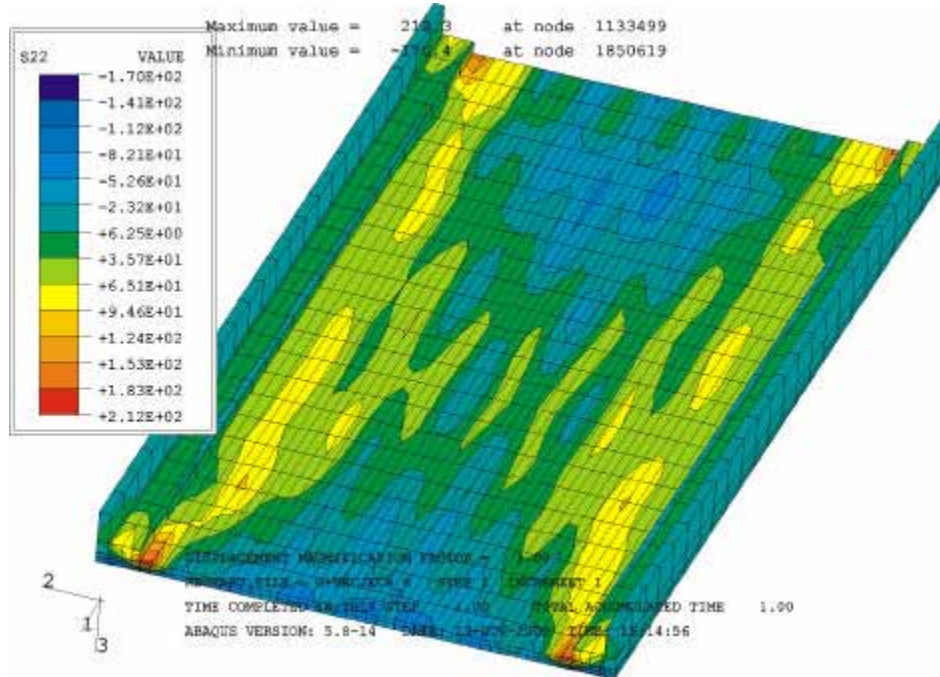


Figure 6.58 contours of stress transverse stress for dead load – gravity. Top surface of deck

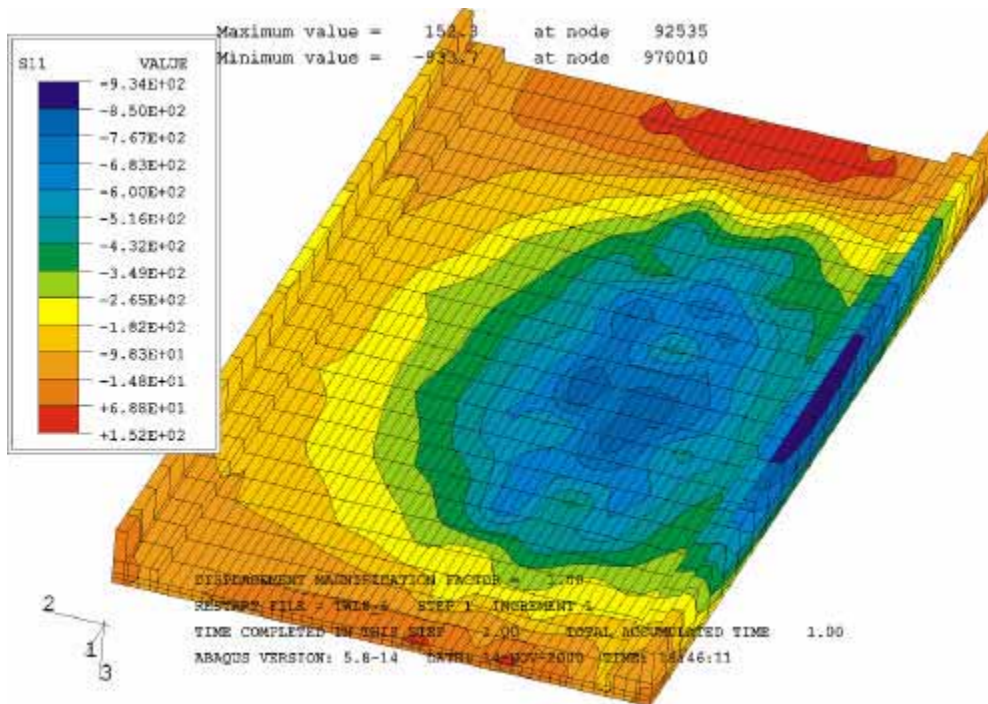


Figure 6.59 Contours of longitudinal stress for live load, run #7 – truck A, center of lane. Top surface of deck

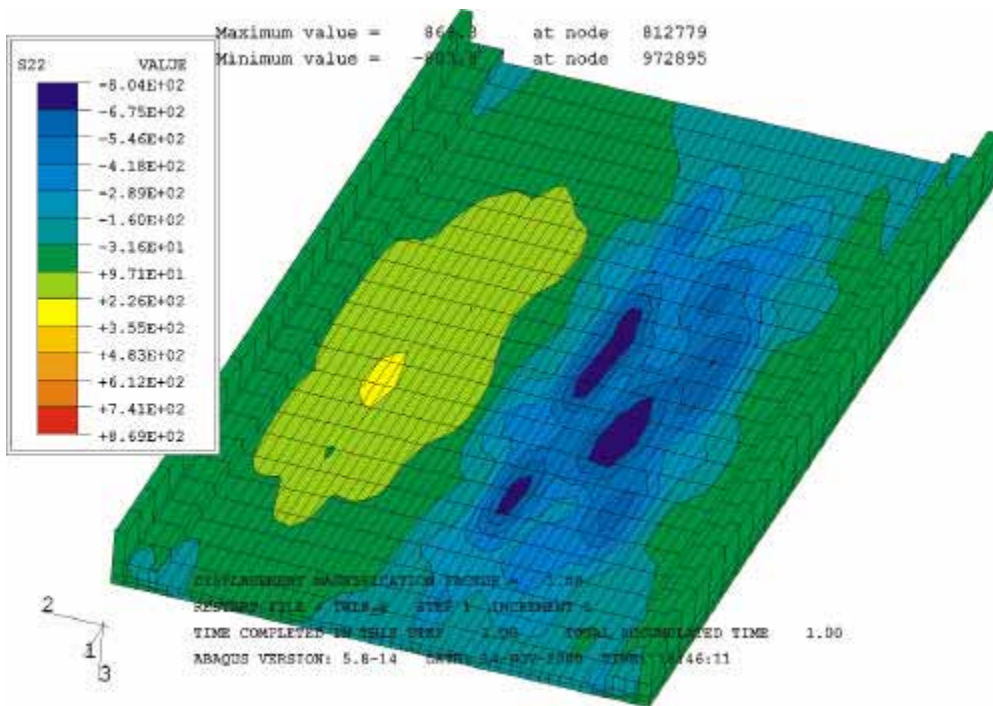


Figure 6.60 Contours of transverse stress for live load, run #7 – truck A, center of lane. Top surface of deck

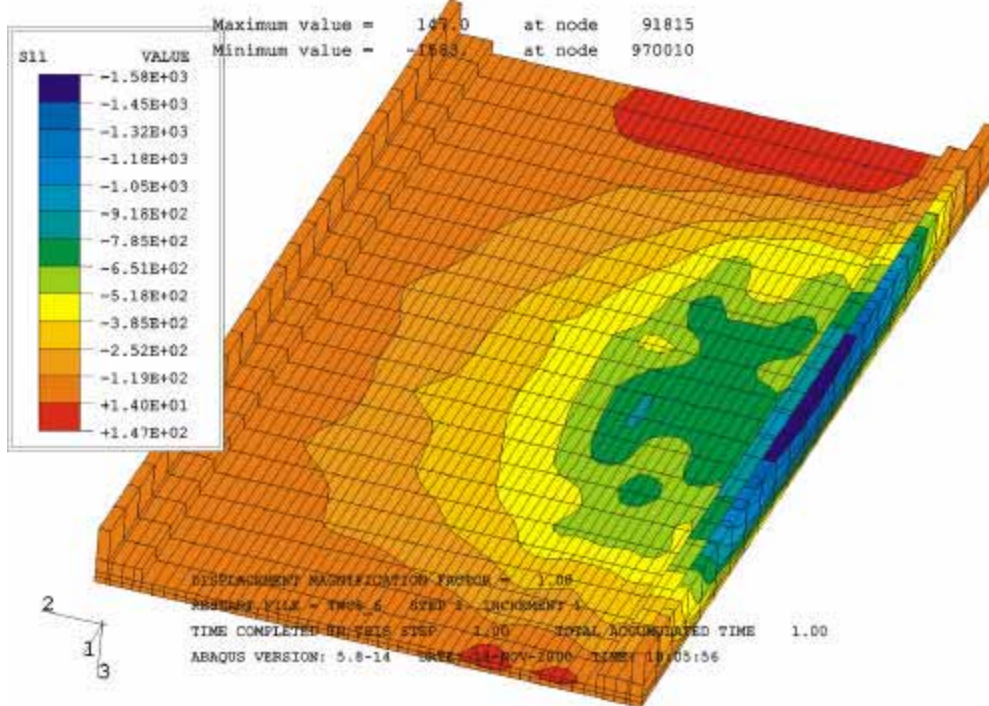


Figure 6.61 Contours of longitudinal stress for live load, run #8 – truck A, close to curb. Top surface of deck

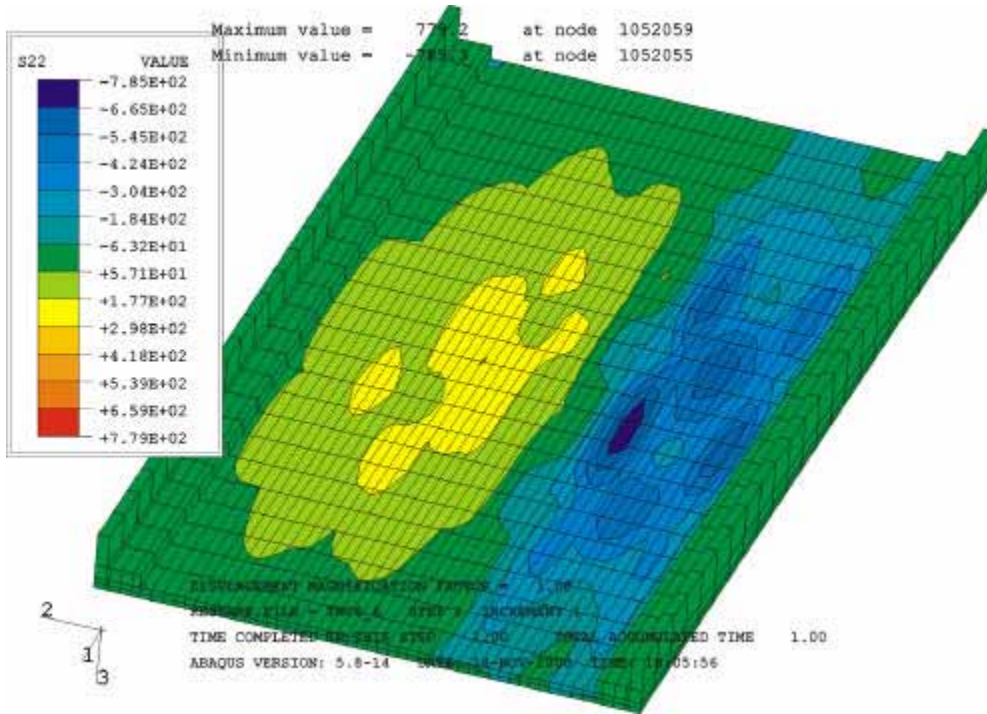


Figure 6.62 Contours of transverse stress for live load, run #8 – truck A, close to curb. Top surface of deck

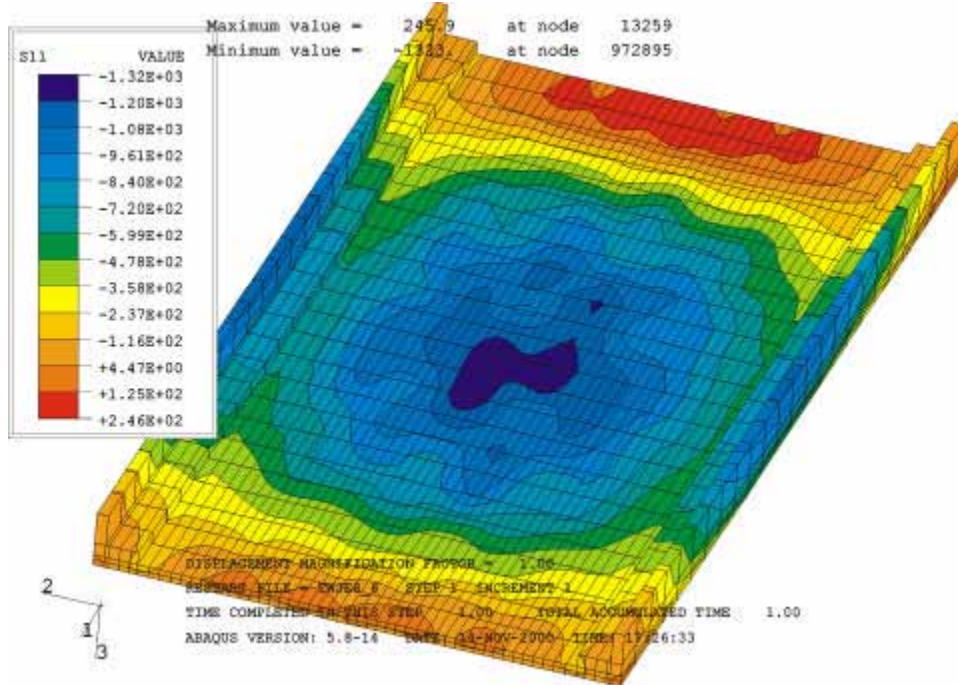


Figure 6.63 Contours of longitudinal stress for live load, run #13 – truck A and B, center of lane. Top surface of deck

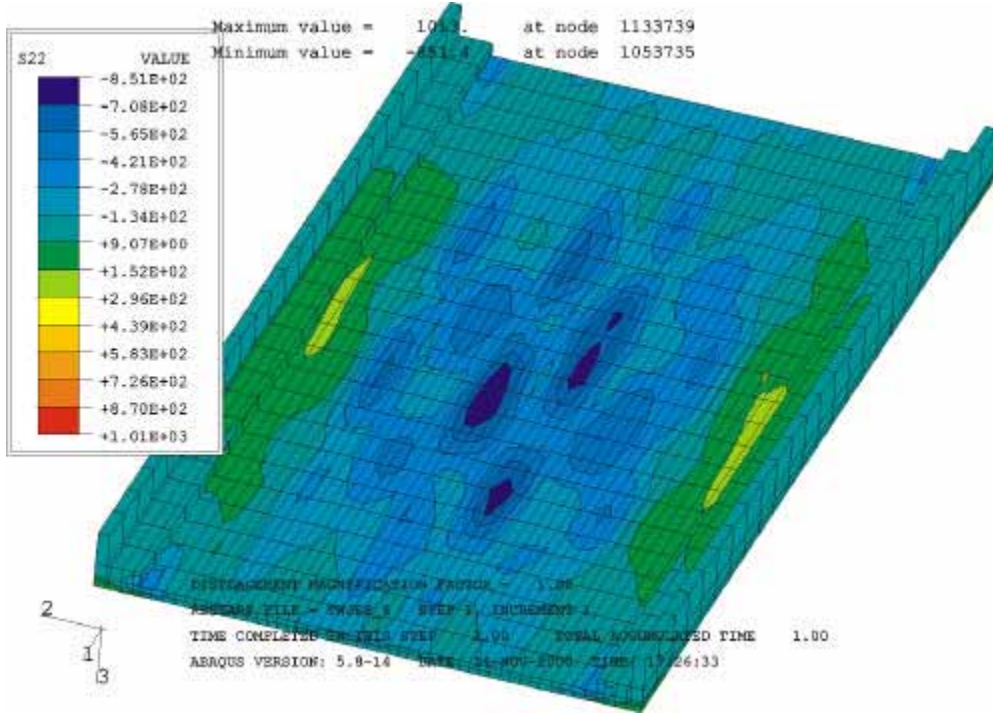


Figure 6.64 Contours of transverse stress for live load, run #13 – truck A and B, center of lane. Top surface of deck

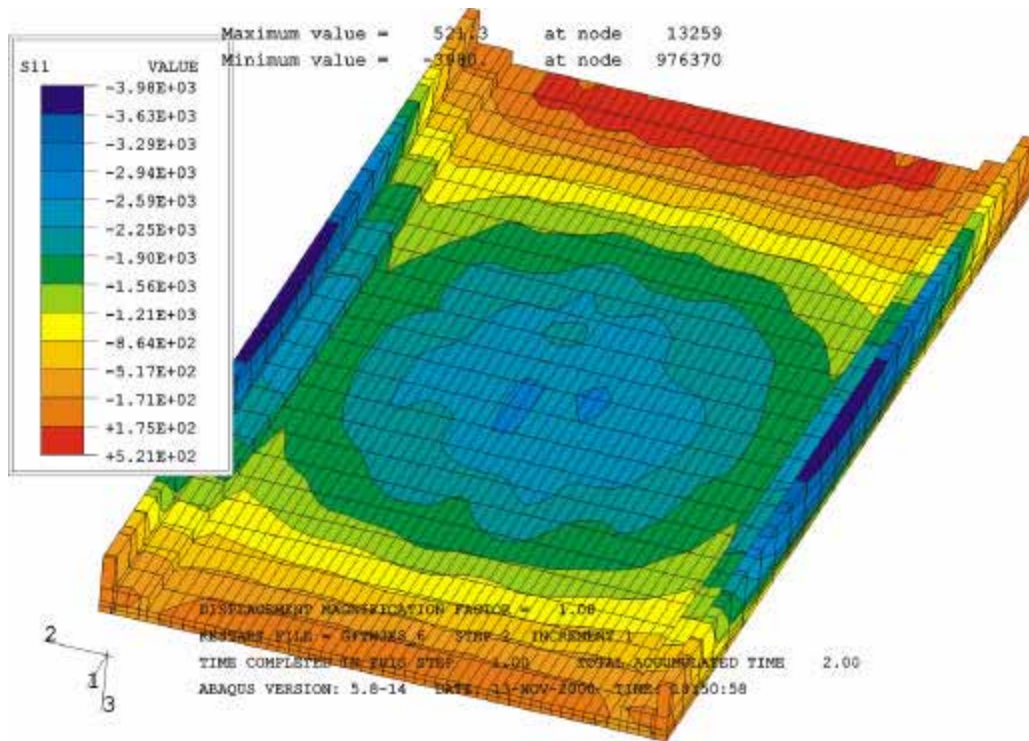


Figure 6.65 Contour of longitudinal stress for dead and live loads – gravity and run #13. Top surface of deck

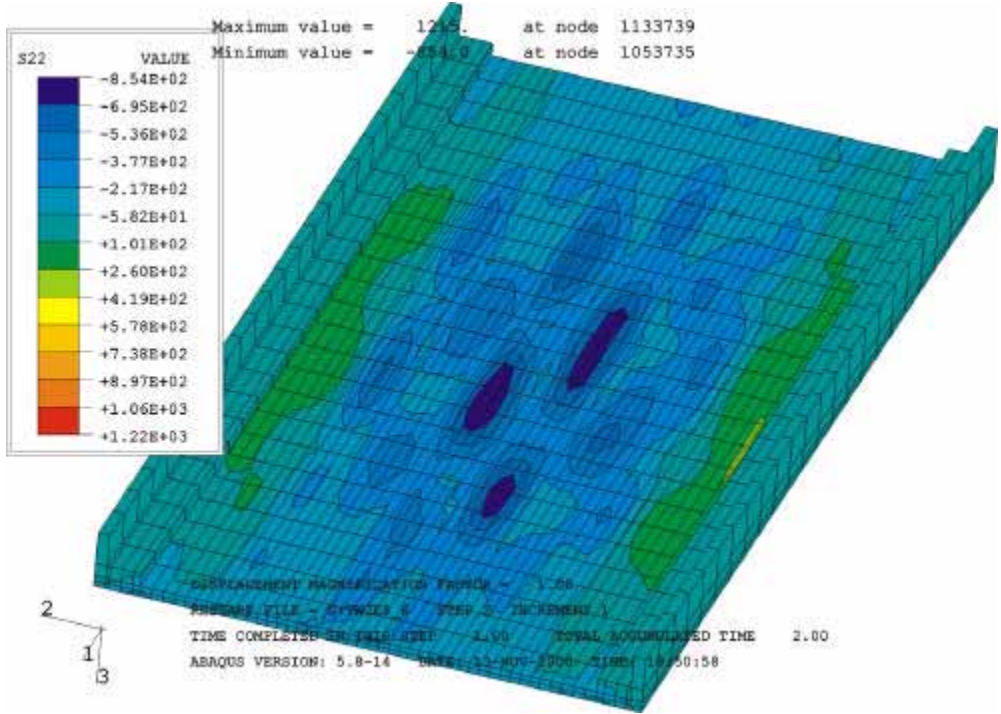


Figure 6.66 Contour of transverse stress for dead and live loads – gravity and run #13. Top surface of deck.

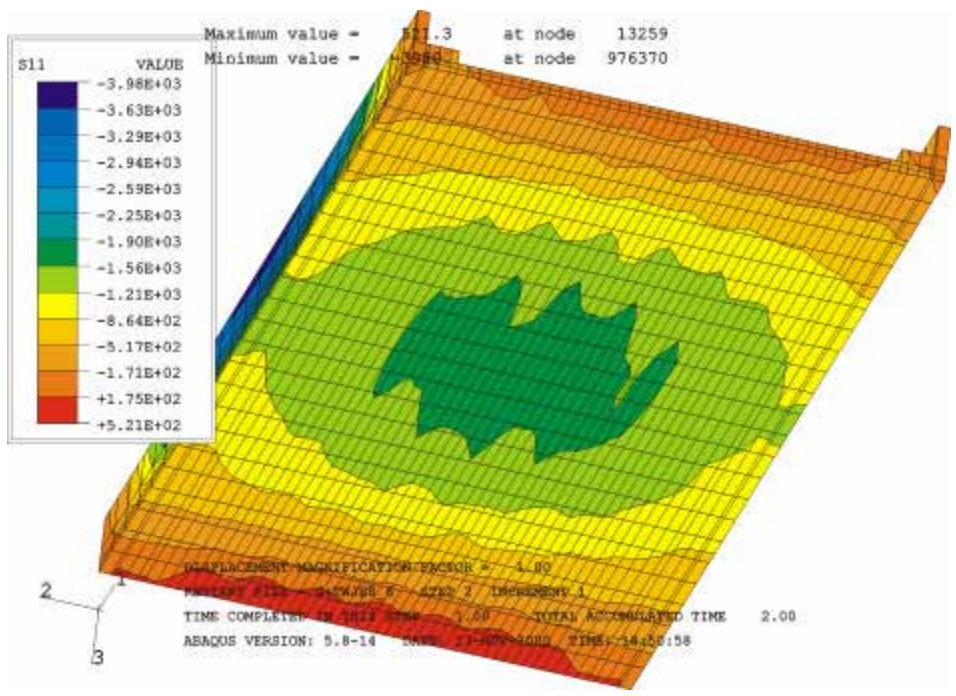


Figure 6.67 Contour of longitudinal stress for dead and live loads – gravity and run #13. Bottom surface of deck

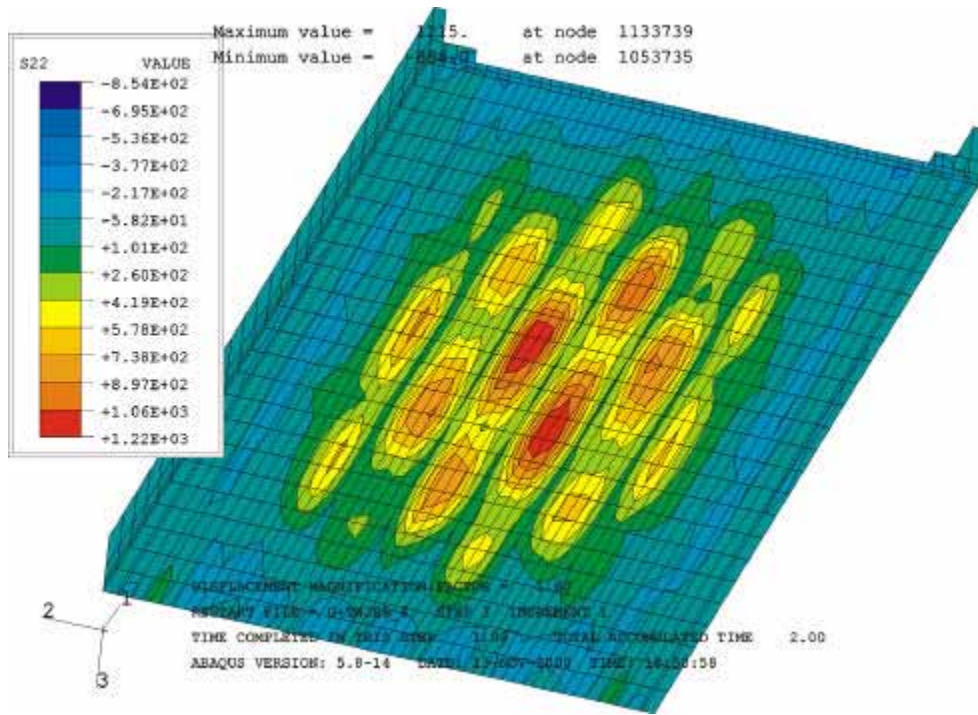


Figure 6.68 Contour of transverse stress for dead and live loads – gravity and run #13.
 Bottom surface of deck

6.5.3 Temperature

To check the influence of temperature changes on the concrete deck slab the following temperature loading is used. The maximum gradient of temperature is assumed to be 15 °C. This gradient is applied in the model to the nodes belonging to barriers, sidewalks and the top surface of the deck. It is assumed that the temperature gradient changes its value linearly in the slab depth, reaching the value of 0 °C at its bottom surface. In girders and diaphragms there is no temperature changes (gradient equal 0 °C). The distribution of applied temperature gradient in the slab thickness is presented in Figure 6.69.

Figures 6.71-6.75 show contours of strains and stresses. In Table 6.5 extreme values of strains and stresses are included. Presented calculated data shows that maximum tension occurs in the transversal direction (see Figures 6.72 and 6.74 showing contours for transverse strain and stress). This tension is concentrated in the places where girders are connected with the slab, Figure 6.75. This means that possible cracks in the slab caused by temperature changes should have longitudinal direction. They can be initiated in the top surface where there is bigger distance from the upper layer of reinforcement.

Table 6.5 Range of strains and stresses in the slab for temperature loading.

#	Strains and stresses	Range of strains and stresses
1	longitudinal microstrains	+5.4 - +22.4
2	transverse microstrains	+2.2 - +23.1
3	longitudinal stress [MPa]	-0.22 - +0.25
4	transverse stress [MPa]	-0.25 - +0.44

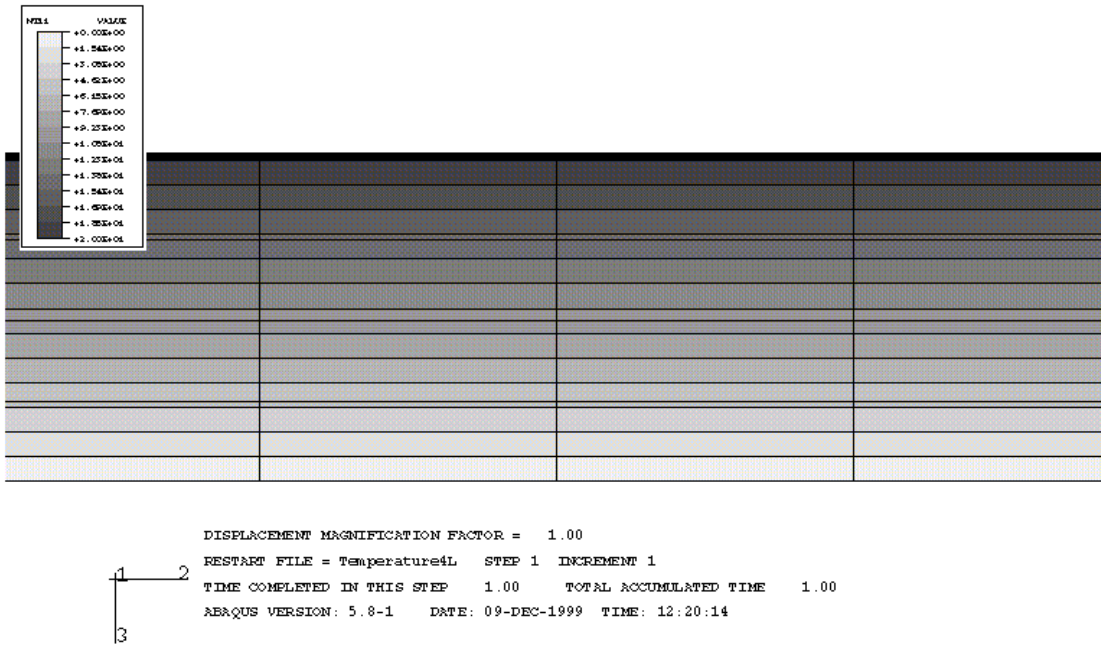


Figure 6.69 Distribution of applied temperature gradient in the slab thickness.

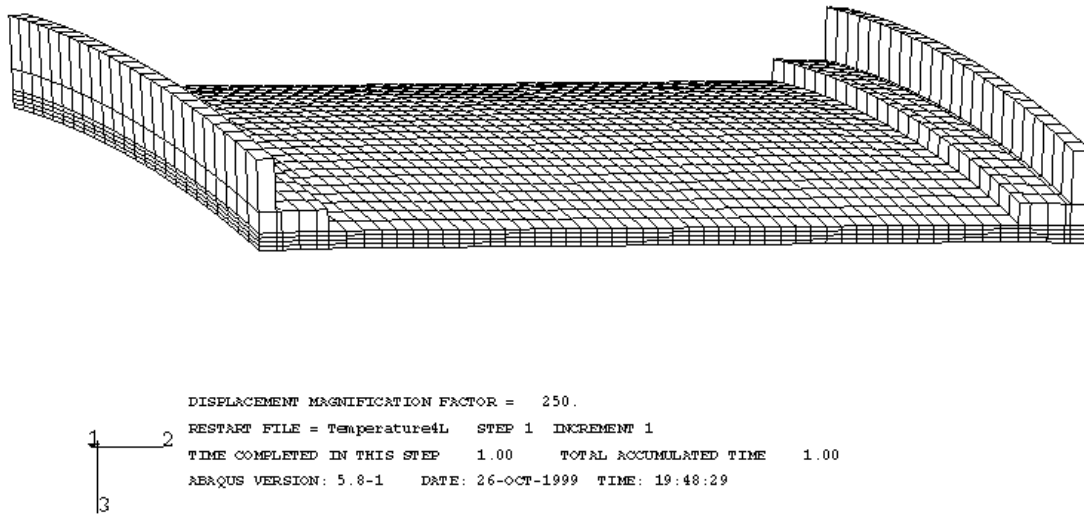


Figure 6.70 Deformation of the slab for temperature gradient $\Delta t = 15^\circ\text{C}$.

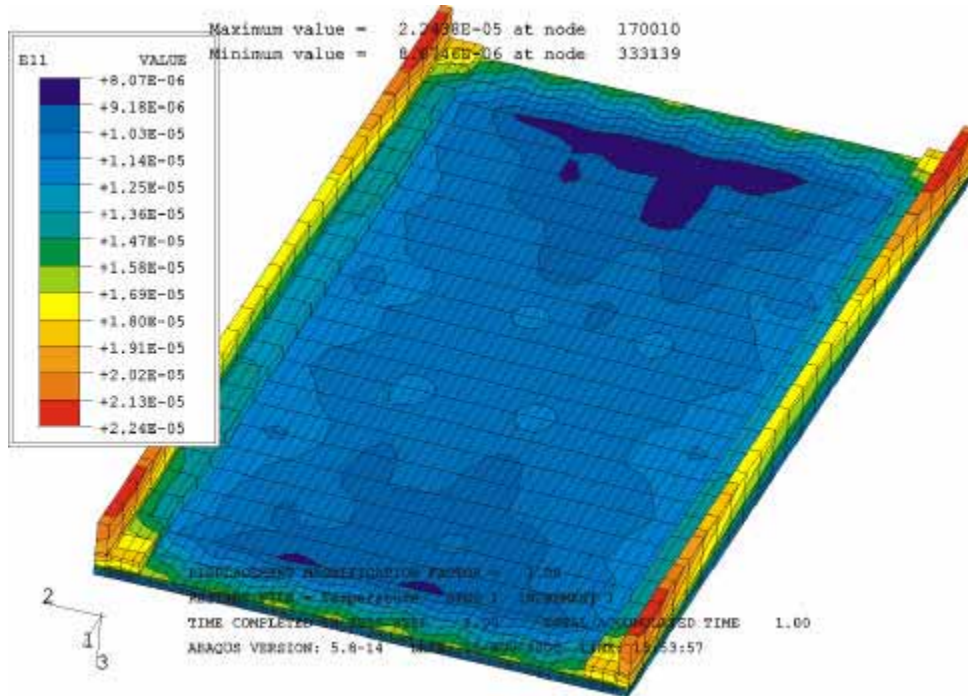


Figure 6.71 Contours of longitudinal strains in the slab for temperature gradient $\Delta t = 15$ °C. Tension on top surface.

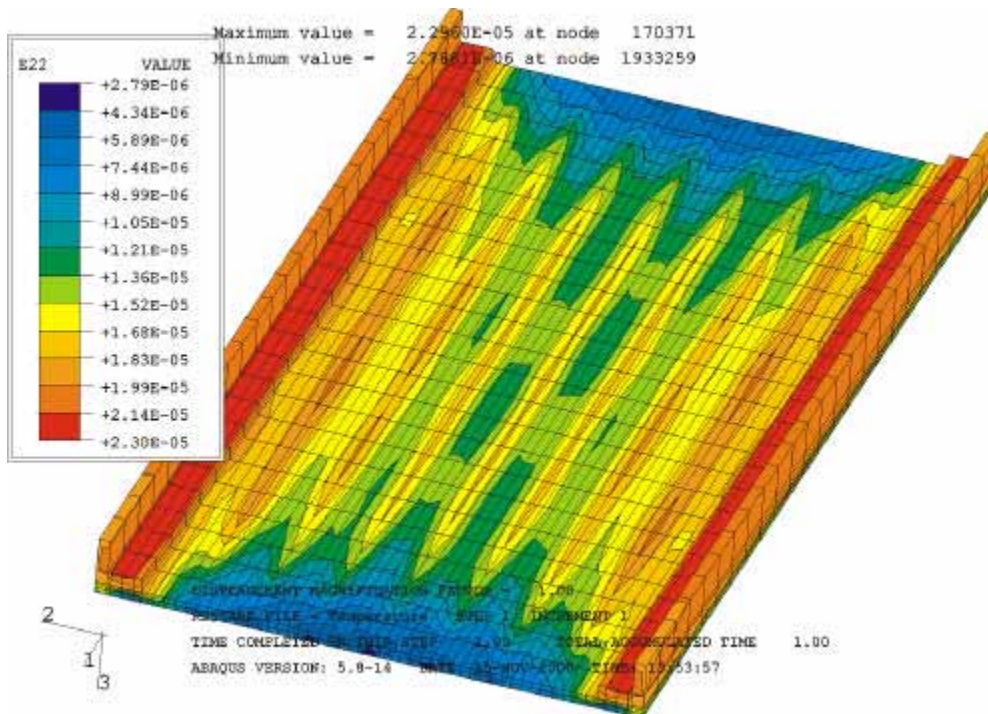


Figure 6.72 Contours of transverse strains in the slab for temperature gradient $\Delta t = 15$ °C. Tension on top surface

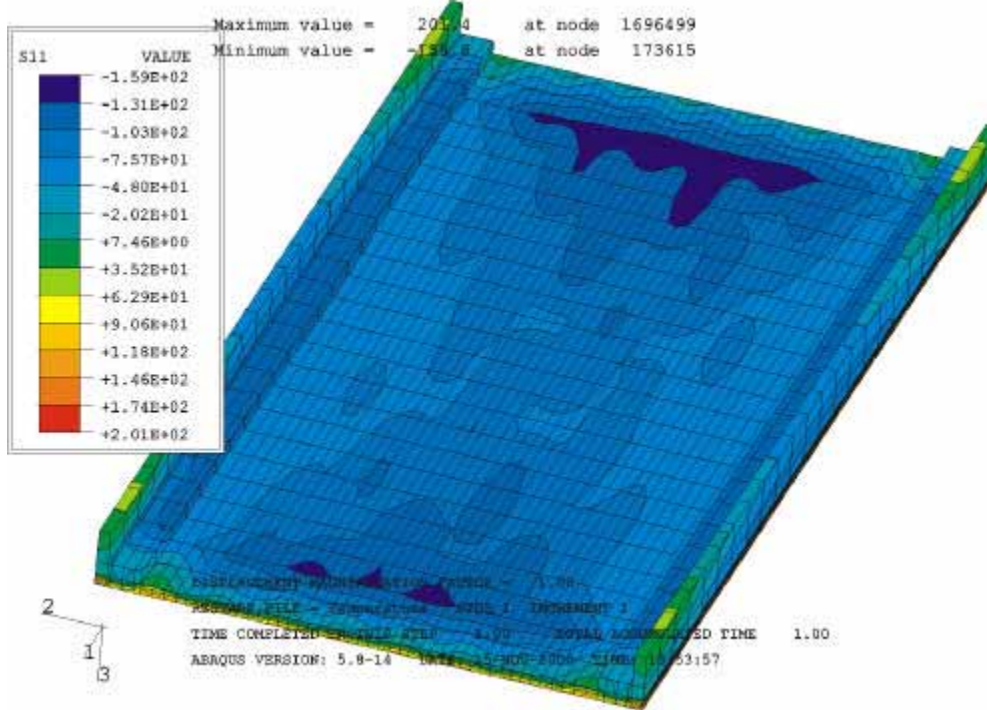


Figure 6.73 Contours of longitudinal stresses in the slab for temperature gradient $\Delta t = 15$ °C. Top surface of deck; maximum value in tension = 201.4 kPa, minimum value in compression = 156.8 kPa.

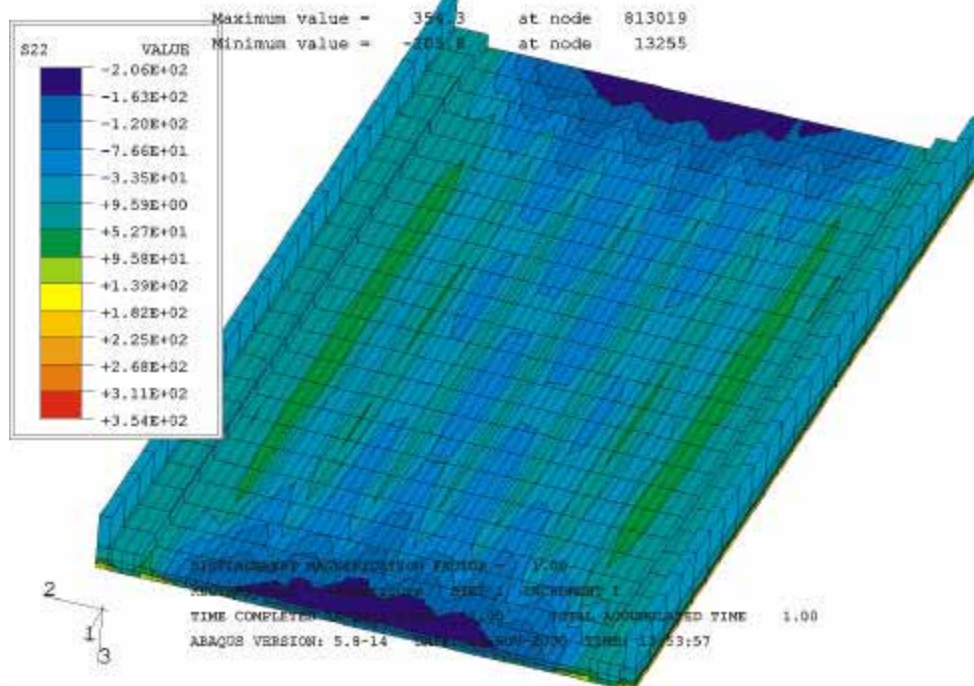


Figure 6.74 Contours of transverse stresses in the slab for temperature gradient $\Delta t = 15$ °C. Top surface of deck; maximum value in tension = 354.3 kPa, minimum value in compression = 205.8 kPa.

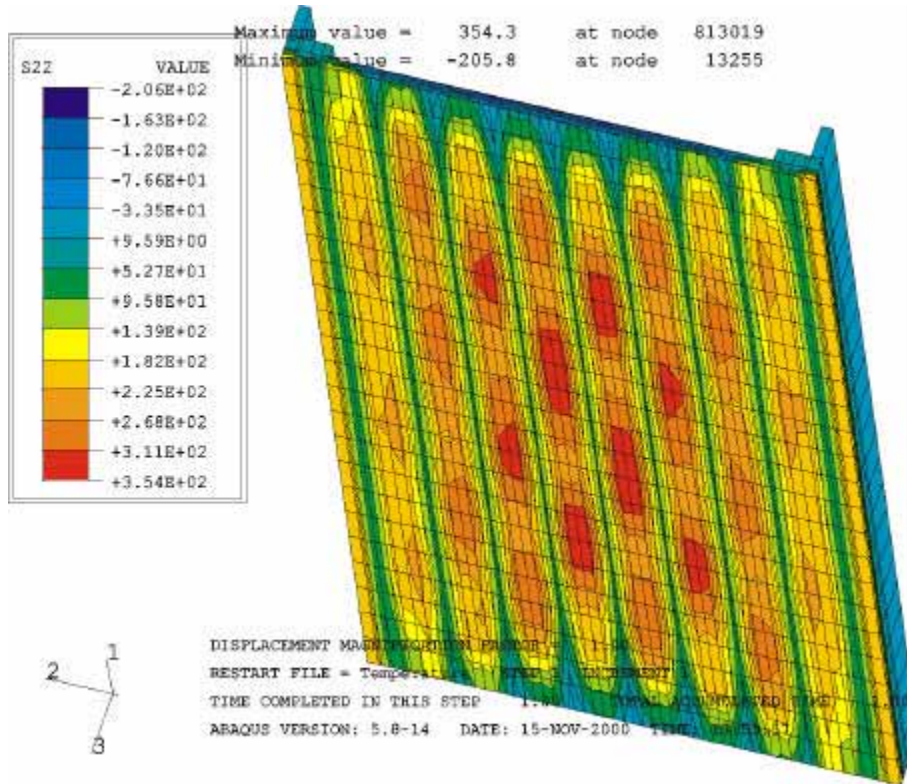


Figure 6.75 Contours of transverse stresses in the slab for temperature gradient $\Delta t = 15$ °C. Bottom surface of deck; maximum value in tension = 354.3 kPa, minimum value in compression = 205.8 kPa.

6.5.4 Conclusions

The following conclusions have been made after completing the Finite Element Analysis of deck slab bridges.

The developed finite element (FE) model of girder bridges provides accurate representation of the actual behavior. The parameters were calibrated using field measurements.

- Properly modeled boundary conditions are very important for the behavior of deck slab and girders. They were verified by comparison with field data.
- In the cases where the test data is not available approximate assessment of boundary conditions can also be achieved. It should be based on the visual inspection and engineering experience.
- Calculations made for the calibrated model with different dead and live load configurations gave small values of strain and stress in the deck slab. The magnitude of received stress in the slab is much smaller than assumed f_{c1}' - absolute value of compressive stress defining the first stress-strain point of initial yielding in concrete.
- Tension stresses in the slab due to dead and live loads are small too, so reinforcement should be enough to protect the slab against cracking. Calculated tensile stresses for the slab are bigger in the bottom surface than in the top. It seems that dead and live loads are not the direct causes of slab cracking.
- The temperature gradient of $\Delta t = 15$ °C was applied in the model as a possible day - night temperature change on the deck surface. Received results show that extreme tension strains, which have transversal direction, concentrate in the connections between girders and slab. Possible cracks due to temperature change should have longitudinal direction and spacing similar to the distance between girders.

It should be pointed that FE analysis was applied here only for short single span bridges designed with simple support. Conclusions presented here should be limited only to such cases.

7. PUNCHING SHEAR FAILURE MODE

Punching shear failure mode is considered in this study, corresponding to the ultimate limit state. The analysis is based on field inspections, field-testing, and additional structural analysis.

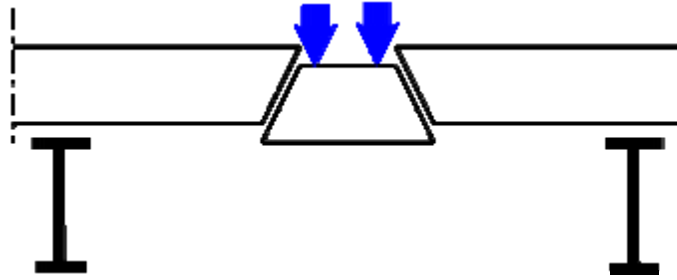


Figure 7.1. Punching shear failure.

The truck wheel load is based on the actual data documented in the report “Measurement of Truck Load on Bridges in Detroit Area” (Nowak et al. 1997). The critical load is caused by a front truck wheel (steering axle), because it is a single tire with smaller contact area compared with non-steering axles (dual tire). It is assumed, that punching shear damage occurs when the shear stress caused by vertical force applied to wheel contact area exceeds the ultimate punching shear strength for concrete.

The statistical distribution functions of axle load were taken from measurements taken on M-39 over M-10 (Nowak et al. 1997). The analysis was performed for two values of wheel load: 42.5 kN, with the probability of being exceeded of 0.10, and 49 kN, with the probability of being exceeded of 0.05. The static force is increased by the dynamic force occurring when the wheel hits a pot-hole in the deck. This additional force depends on the mass of wheel, vehicle speed and the hole size.

The punching shear stress depends on the value of the vertical load; contact area and the force transfer area. The latter depends on the slab thickness. The analysis is performed for three different concrete strengths, a wide spectrum of slab thickness, and several different dimensions of pot-holes (length) in the deck.

The dynamic force is generated when the rolling wheel hits the edge of the hole (bump effect). Value of the force depends on the size of the hole (length and depth). The dynamic force is considered only when the hole is bigger than the tire contact area, otherwise it is neglected. The equation to calculate the vertical dynamic force, F_{dyn} , is derived from kinetic energy balance before and after the impact,

$$F_{dyn} = \tan(\varphi)[m(v_o - v_1)v_o]/c \quad (7-1)$$

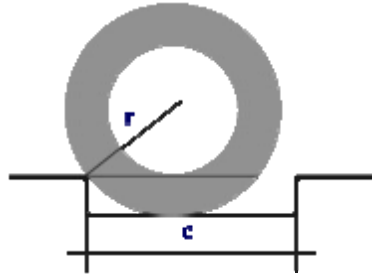
where:

m = mass of the wheel [kNsec²/m]

v_o = speed of the vehicle before hitting the pot-hole [m/sec]

v_1 = speed of the vehicle after passing the pot-hole [m/sec]

c = length of the pot-hole (in the direction of driving) [m]



The values of F_{dyn} , calculated for different size of the hole and different vehicle speeds are shown in Table 7-1.

The punching shear stress, f_v , is calculated as the ratio of applied force and transfer area. The wheel contact area for steering wheel is assumed equal to 190 x 250 mm (500 x 250 mm for a dual tire), and the transfer area $(190 + d) \times (250 + d)$, where d denotes the thickness of the slab. The applied force is the sum of the static and dynamic wheel load (the largest dynamic force was used in calculations). The resulting values of punching shear stress are shown in Table 7-2a,b for two load levels, with probabilities of being exceeded equal to 0.10 and 0.05.

Table 7-1. Dynamic Forces for Different Sizes of the Hole and Vehicle Speeds

Length of the hole c_h (m)	Depth of the hole d_h (mm)	Dynamic force, F_d (kN)			
		$v = 60$ km/h	$v = 70$ km/h	$v = 80$ km/h	$v = 110$ km/h
0.30	20	17.92	24.37	31.84	60.00
0.40	40	9.80	13.32	17.40	32.80
0.50	60	6.06	8.24	10.76	20.12
0.60	80	4.01	5.45	7.12	13.67
0.70	110	2.76	3.75	4.90	9.10

The dynamic force increases with the vehicle speed and the relationship is linear. The increase depends on the size of the hole.

Table 7-2a. Punching Shear Stress for Wheel Load with Probability of being Exceeded of 0.10

Thickness of Slab (mm)	Transfer Area (m^2)	Punching Shear (kPa)			
		110 km/h	80 km/h	70 km/h	60 km/h
230	0.200	512.5	371.7	336.3	304.1
215	0.190	539.5	390.0	350.7	316.8
200	0.180	569.4	411.7	370.2	334.4
190	0.170	603.0	435.9	392.0	354.1
180	0.160	640.6	463.2	416.5	376.2
165	0.150	683.3	494.1	444.3	401.3
150	0.140	732.1	529.4	476.0	430.0
140	0.130	788.5	570.1	512.6	463.0
130	0.120	854.2	617.6	555.3	501.6
115	0.110	931.8	673.7	605.8	547.2

Table 7-2b. Punching Shear Stress for Wheel Load with Probability of being Exceeded of 0.05

Thickness of Slab (mm)	Transfer Area (m ²)	Punching Shear (kPa)			
		110 km/h	80 km/h	70 km/h	60 km/h
230	0.200	545.0	404.2	366.8	334.6
215	0.190	573.7	425.2	385.9	351.9
200	0.180	605.6	448.8	407.3	371.5
190	0.170	641.2	475.2	431.3	393.3
180	0.160	681.2	504.9	458.3	417.9
165	0.150	726.7	538.6	488.8	445.8
150	0.140	778.6	577.1	523.7	477.6
140	0.130	838.5	621.5	564.0	514.4
130	0.120	908.3	673.3	611.0	557.3
115	0.110	990.9	734.4	666.5	607.9

A typical MDOT deck slab is not reinforced for shear stresses, so the ultimate shear stress depends on the compressive strength of the concrete, f_c' [MPa], and is equal to $0.17\sqrt{f_c'}$.

Punching shear stress increases with decreasing slab thickness, for example when slab thickness is reduced due to deterioration (cracks, crashed concrete, pot-holes and delamination).

The actual value of shear stress depends on the truck load (wheel force), which is a random variable. The calculations were performed for two live load levels, the upper 10th percentile, with probability of being exceeded equal to 0.1, and the upper 5th percentile, with the probability of being exceeded equal to 0.05. The resulting relationship between the shear stress and slab thickness is shown in Figure 7-4 for the 10th percentile live load, and Figure 7-5 for the 5th percentile live load, for truck speed from 60 to 110 km/h. For comparison, the ultimate shear stress, $0.17\sqrt{f_c'}$, is also shown in Figures 7-4 and 7-5 for $f_c' = 20$ to 31 MPa.

Figures 7-4 and 7-5 indicate that punching shear failure can occur in case of poor quality of concrete, low strength of concrete, or when the upper portion of the deck has been considerably deteriorated. The forms of failure include cracking, spalling, and formation of

through-holes. Falling pieces of concrete were observed on a number of bridges in the Detroit area.

In fact, vertical force in the slab changes sign when the axle load is moving along the slab length and the shear stress is applied as cycles of loading with reverse sign. Cyclic stress applied with a reverse sign are much more damaging than fatigue load in compression or even tension only. This has been confirmed by research work carried out by Matsui (1997) in Japan.

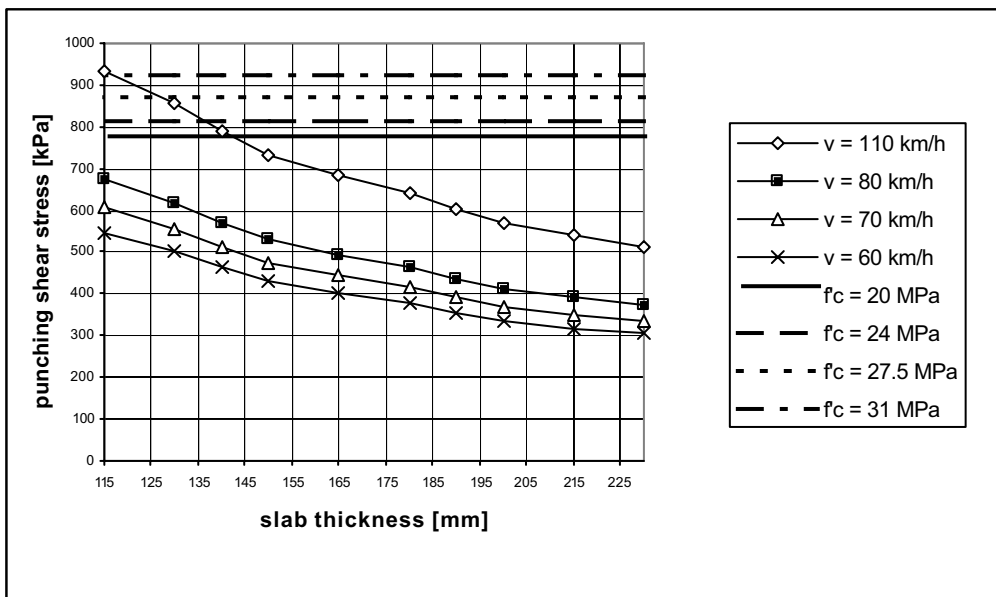


Figure 7-4. Punching Shear Stress versus Slab Thickness, Probability = 0.10.

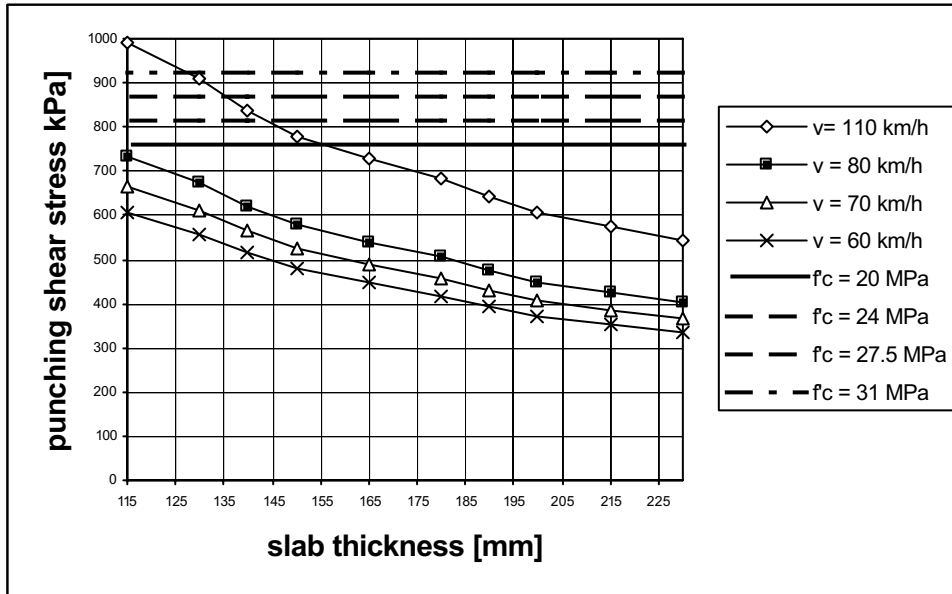


Figure 7-5. Punching Shear Stress versus Slab Thickness, Probability = 0.05.

8. SUMMARY

The report contains the background information for the Michigan Evaluation Guide. The considered topics include models for concrete shrinkage and fatigue, documentation on field tests (compressive strength and modulus of elasticity of concrete), the results of bridge decks review, and analysis of deck's deterioration pattern based on MDOT Bridge Inspection File. The finite element model of bridge superstructure is presented to investigate the influence of deck degradation (by changing the properties of concrete), live load effect, and temperature effect on bridge deck behavior. Finite element model was calibrated by adjusting support conditions, using data from the field load test. The report provides information on stress and strain level in the deck slab under the dead load, live load (depending on load position), and temperature gradient. In addition, the sensitivity analysis shows the relationship between the deck slab behavior and stiffness of the slab. The shear failure mode in the deck slab is also discussed.

REFERENCES

- AASHTO LRFD Bridge Design Specifications, American Association of State Highway and Transportation Officials, Washington, DC, 1994 and 1998.
- ABAQUS/Standard User's Manual, Version 5.6, Hibbitt, Karlson & Sorensen, Inc. 1996.
- Alaylioglu H., Alaylioglu A., Static behavior simulation of a bridge structure by an FE-PC model, *Simulation Practice and Theory* 5, pp. 49-63, 1997.
- Bhatt P., *Programming the Matrix Analysis of Skeletal Structures*, Ellis Horward, Chichester, England, 1986.
- Boothby, T.E. and Laman, J.A., Cumulative Damage to Bridge Concrete Deck Slabs due to Vehicle Loading, *Journal of Bridge Engineering*, Feb. 1999.
- De Brito, J., Branco, F.A., Thoft-Christensen, P. and Sorensen, J.D., An expert system for concrete bridge management, *Engineering Structures*, Vol. 19, No. 7, pp. 519-526, 1997.
- BS 5400 Code of Practice, British Standard Steel, Concrete and Composite Bridges, Part 4: Code of Practice for Design of Concrete Bridges, British Standards Institution, 1990.
- Cornelissen, H.A., Hordijk, D.A. and Reinhardt, H.W., Experimental determination of crack softening characteristics of normal weight and lightweight concrete, *Fracture mechanics and structural aspects of concrete*, Heron, Vol. 31, No 2, 1986.
- Cussens A.R., *Bridge Deck Analysis*, Wiley, London, 1975
- Enright, M.P. and Frangopol, D.M., Service-Life Prediction of Deteriorating Concrete Bridges, *Journal of Structural Engineering*, Vol. 124, No 3, 1998.
- French, C., Eppers, L., Le, Q. and Hajjar, J.F., *Transverse Cracking in Concrete Bridge Decks*, Transportation Research Record, Washington, DC, 1999.
- Hambly E.C., *Bridge Deck Behavior*, Chapman & Hall, London, 1991.
- Hays C.O. Jr., Sessions L.M., Berry A.J., Further studies on lateral load distribution using finite element methods, *Transp. Res. Rec.*, Transportation Research Board, Washington D.C., 6-14, 1997.
- Holmen, J.O., *Fatigue of concrete by constant and variable amplitude loading. Fatigue of concrete structures*, ACI, Publ.SP 75, Detroit, 1982.

- Kim, S-J., Sokolik, A.F., and Nowak, A.S., 1997, "Measurement of Truck Load on Bridges in the Detroit Area", *Transportation Research Record*, No.1541, pp. 58-63.
- Mabsout M.E., Tarhini K.M., Frederick G.R., Kesserwa A., Effect of Multilanes on wheel Load distribution in steel girder Bridges, *Journal of Bridge Engineering*, Vol. 4, No.2, 1999.
- Matsui, S., "Technology Developments for Bridge Decks" – "Innovations on Durability and Construction", *Kyouryou To Kiso* (8), 1997, pp. 84-92.
- Miner M.A. Cumulative Damage in Fatigue. *Trans. ASME*, Vol.67, 1945.
- Non-Structural Cracks in Concrete, Technical Report No 22, Third Edition, The Concrete Society, 1992.
- Nowak, A.S., "Load Distribution for Plank Decks", UMCEE 97-11, Report submitted to US Forest Service, April 1997.
- Nowak, A.S., Kim, S-J., Laman, J., Saraf, V. and Sokolik, A.F., "Truck Loads on Selected Bridges in the Detroit Area", Final Report submitted to MDOT, November 1994.
- Nowak, A.S., Laman, J. and Nassif, H., "Effect of Truck Loading on Bridges", Final Report submitted to MDOT, December 1994.
- O'Brien E.J., Keogh D.L., Upstand finite element analysis of slab bridges, *Computers and structures* 69, 1998.
- Okba, S.H., El-Dieb, A.S. and Reda, M.M., Evaluation of the Corrosion Resistance of Latex Modified Concrete (LMC), *Cement and Concrete Research*, Vol.27, 1997.
- Ray, I., Gupta, A.P. and Biswas, M., Effect of Latex and Superplasticiser on Portland Cement Mortar in the Hardened State, *Cement and Concrete Composites*, Vol.17, 1995.
- Regan, P.E., The Punching Resistance of Prestressed Concrete Slabs, *Proc. Instn Civ. Engrs.* Part 2, 1985.
- Schlaflli, M. and Bruhwiler, E., Fatigue of existing reinforced concrete bridge deck slabs, *Engineering Structures*, Vol. 20, No. 11, pp. 991-998, 1998.
- Schultz J.L., Commander B., Goble G.G., Frangpol D.M., Efficient field Testing and load Rating of Short – And Medium – Span Bridges, *Structural Engineering review*, Vol. 7, No 3 pp181-194, 1995.
- Shaker, F.A., El-Dieb, A.S. and Reda, M.M., Durability of Styrene-Butadiene Latex Modified Concrete, *Cement and Concrete Research*, Vol.27, 1997.

- Silfwerbrand, J. and Paulsson J., Better Bonding of Bridge Deck Overlays, *Concrete International*, Oct. 1998.
- Stewart, M.G. and Rosowsky, D.V., Time-dependent reliability of deteriorating reinforced concrete bridge decks, *Structural Safety* 20, pp.91-109,1998.
- Szerszen, M.M., Destrebecq, J-F. and Dyduch, K., Experimental Investigation of the Fatigue Strength of Plain Concrete under Compressive Loading, *Structures & Materials*, Vol.27 (173), 1994.
- Szerszen, M.M., Destrebecq, J-F. and Dyduch, K., Behavior and Durability of Concrete with Regards to Cycle and Time Dependant Effects, *IABSE Symposium: Extending the Lifespan of Structures*, San Francisco, 1995.
- Tarhini K.M., Frederic G.R., Wheel Load Distribution in I-Girder Highway Bridges’, *Journal of Strustural Engineering*, Vol. 118, No. 5, may, 1992.
- West R., Recommendations on the use of grillage analysis for slab and pseudo-slab bridge decks, *C.&C.A./C.I.R.I.A.*, London, 1973.
- Zhang Z., Aktan A.E., Different Levels of Modeling for the Purpose of Bridge Evaluation, *Applied Acoustics*, Vol. 50, No 3 pp.189-204, 1997.